

# Study of Spectroscopic Properties of Proton Rich Nuclei

A Thesis Submitted

to the

University of Allahabad

for the degree of

**Doctor of Philosophy  
in Science**

by

**Tarkeshwar Trivedi**



under the supervision of

**Prof. (Mrs.) Indira Mehrotra**

Department of Physics

University of Allahabad

Allahabad -211002

INDIA

Year 2010

# Acknowledgements

I would like to express my sincere gratitude towards my D. Phil guide Prof.(Mrs.) Indira Mehrotra for her elite guidance, ceaseless encouragement and support throughout my research work. I thank her for giving me time despite her extremely hectic schedule. I appreciate her for valuable physics discussions, motivating advice and invaluable guidance during my academic carrier.

I would like to express my sincere gratitude to Dr. Ranjan Bhowmik of IUAC, under whose guidance I have gained familiarity and knowledge on nuclear instrumentation and several experimental techniques.

My sincere gratitude to Dr. Amit Roy, Director IUAC for his keen interest and encouragement during the course of my research work and providing me all the necessary facilities and local hospitality during my IUAC visits.

I would like to thank Dr. R. Palit, TIFR for rendering his valuable support at the TIFR and subsequent helpful discussions during my research work.

I am extremely thankful to Prof. S. C. Pancholi for introducing me with the experimental nuclear physics. I am also thankful to Prof. Y. Sun, Prof. J. Sheikh for their help in the theoretical calculations and discussions.

It has been my great pleasure to work with Mr. S. Muralithar and would like to thank him for his valuable help during online as well as off-line data analysis. I am thankful to Mr. R.P. Singh and Mr. Rakesh Kumar for their invaluable help at different stages of my work. I am also thankful to Dr. S.S. Gughare for very informative discussion during the learning of OXBASH code.

I owe my gratitude to Prof. H.C. Jain and Prof. A.K. Jain for their constant encouragement and valuable suggestions from time to time during the course of my work.

My sincere gratitude to late Prof. C.V.K. Baba, Prof. S.K. Datta and Prof. S.B. Patel for their valuable suggestions during my course of work at IUAC. The help and encouragement received by Dr. J.J. Das, Mr. N. Madhavan, Mr. Subir Nath, Mr.Jagadeesh Gahlot, Mr.Sunil Ojha, Mr. Rajesh Kumar and Mr P. Barua is highly acknowledged. My special thanks to Mr. S. R. Abhilash and Dr. D. Kabiraj for their

help and cooperation during the preparation of targets and to Pelletron accelerator staff for smooth operation of the machine during the experimental run.

I am extremely thankful to my close friend Mr. Dinesh Negi, for his tremendous help and support at each and every stage of my thesis work, not only academically but also in every respect; without which my D. Phil work would have been much more difficult.

The encouragement of Dr. Vivek Kumar Tiwari is gratefully acknowledged. I would also like to thank the research scholars of our groups P.C. Srivastava, A. Devi, P. Gupta, K. Maurya and Uma Shankar for their help from time to time while pursuing my D. Phil work. I thank my friends Pavitra, Pramod, Dharmendra, Raghvendra, Vineet, Giradhar and R.B. for their excellent company and many memorable occasions at Allahabad.

I also like to thank Drs. Vivek Parker, Vinod kumar, Shuresh Kumar and A. Dhal for some useful discussions and help. It is a great pleasure to thank, my friends Yogendra, Rahul, Dinesh Agrawal, Sushil, Appana and Raja for their warm friendship which made my stay at IUAC memorable. I do not want to miss the chance to thank Dr. Bharat and Sushil for their company at TIFR which makes my life enjoyable during TIFR visits.

Above all, my deepest gratitude goes to my mother for her support and encouragement. I take a moment to express my deep sense of gratitude to the fond memories of my late Father, whose love and support, I will miss forever. I express my gratitude to my brother( Dr. Ram N Trivedi), Bhabhi(Vandana), my sisters (Sushila and Uma), jija (Rajan and S. Tewari), my cousin Ansu and to my wife Vineeta for their moral support and encouragement.

Finally, I gratefully acknowledge the IUAC New Delhi, for providing me fellowship to carry out this research work.

*Dedicated to*

*My*

*Late Father*

# Contents

<b>Acknowledgements</b>	<b>ii</b>
<b>1 Introduction</b>	<b>1</b>
1.1 Motivation of the Thesis . . . . .	2
1.1.1 Some features of $A \approx 70 - 80$ mass region . . . . .	2
1.1.2 Some features of $A \approx 100$ mass region . . . . .	4
1.2 Plan of the Thesis . . . . .	5
<b>2 Theoretical Models</b>	<b>8</b>
2.1 Introduction . . . . .	8
2.2 Nuclear Shell Model . . . . .	9
2.3 Deformation parameters . . . . .	11
2.4 Nilsson Model . . . . .	13
2.5 Total Energy-Shell correction . . . . .	16
2.6 Rotating nuclei . . . . .	18
2.6.1 Cranking Model . . . . .	18
2.7 Total Routhian Surfaces calculations . . . . .	21
2.8 Projected Shell-Model . . . . .	22
2.8.1 Projection operator . . . . .	23
2.8.2 Shell model in projected basis . . . . .	24
2.8.3 Choice of Hamiltonian . . . . .	27
2.8.4 Electromagnetic transition strengths . . . . .	28
2.9 Conclusion . . . . .	28

<b>3</b>	<b>Experimental Techniques</b>	<b>30</b>
3.1	Production of proton rich nuclei . . . . .	30
3.2	Accelerator Facility . . . . .	34
3.3	Detector systems . . . . .	35
3.3.1	Interaction of gamma rays with matter . . . . .	35
3.3.2	Germanium detectors . . . . .	37
3.3.3	Compton suppression . . . . .	38
3.3.4	Clover detectors . . . . .	39
3.3.5	Clover in addback Mode . . . . .	40
3.4	Array of Ge detectors . . . . .	41
3.4.1	Indian National Gamma Array at IUAC . . . . .	43
3.5	Electronics and data acquisition system for INGA . . . . .	45
3.5.1	Analog signal processing and data acquisition trigger generation . . . . .	45
<b>4</b>	<b>Target Preparation and Data Analysis</b>	<b>49</b>
4.1	Properties of chromium . . . . .	49
4.2	Details of the target preparation . . . . .	50
4.3	Experimental procedure . . . . .	51
4.3.1	Preparation of gold backing foils . . . . .	51
4.3.2	Deposition of natural chromium . . . . .	52
4.3.3	Deposition of isotopic chromium . . . . .	53
4.3.4	Thickness measurement by X-ray florescence method . . . . .	53
4.4	Data analysis for $\gamma$ -ray spectroscopy . . . . .	54
4.4.1	Correction for gain drift . . . . .	55
4.4.2	Energy calibration and gain matching . . . . .	56
4.4.3	Efficiency calibration . . . . .	58
4.5	Analysis of $\gamma$ - $\gamma$ coincidence data . . . . .	58
4.5.1	$\gamma - \gamma$ Matrices . . . . .	59
4.5.2	Background subtraction . . . . .	59
4.5.3	Total projections and gates . . . . .	60
4.6	Measurement of electromagnetic transition probabilities . . . . .	62

4.7	Methods of lifetime measurements . . . . .	64
4.8	Doppler-shift attenuation method . . . . .	65
4.8.1	Energy loss of heavy ions in materials . . . . .	66
4.8.2	Calculation of line shape . . . . .	68
4.8.3	Line shape analysis . . . . .	69
4.9	Conclusion . . . . .	70
<b>5</b>	<b>Shape Evolution at High Spin in <math>^{75}\text{Kr}</math></b>	<b>72</b>
5.1	Introduction . . . . .	72
5.2	Experimental details . . . . .	75
5.3	Analysis method . . . . .	76
5.4	Results and Discussion . . . . .	82
5.4.1	Projected shell model calculations . . . . .	84
5.4.2	Comparison with data . . . . .	86
5.4.3	Explanation by configuration mixing . . . . .	87
5.4.4	Shape calculations . . . . .	90
5.5	Conclusion . . . . .	93
<b>6</b>	<b>Shape Evolution at High Spins in <math>^{75}\text{Br}</math></b>	<b>95</b>
6.1	Introduction . . . . .	95
6.2	Experimental details . . . . .	96
6.3	Analysis method . . . . .	99
6.4	Results and Discussion . . . . .	105
6.4.1	Projected shell-model calculations . . . . .	109
6.4.2	Shape calculations . . . . .	111
6.5	Conclusion . . . . .	113
<b>7</b>	<b>Shell Model Description of Proton Rich Sn Isotopes</b>	<b>117</b>
7.1	Techniques of calculations and Shell-Model code . . . . .	118
7.1.1	Model space . . . . .	119
7.1.2	Effective interactions . . . . .	119
7.1.3	Shell model code: Nushell . . . . .	122

7.2	Diagonalization via LANCZOS method . . . . .	123
7.3	Details of calculations . . . . .	125
7.4	Results and Discussion . . . . .	126
7.4.1	Excitation energies of even Sn isotopes . . . . .	126
7.4.2	Excitation energies of odd Sn isotopes . . . . .	132
7.5	Electromagnetic transition strengths . . . . .	137
7.6	Conclusion . . . . .	138
<b>8</b>	<b>Summary and Future Perspective</b>	<b>139</b>
8.1	Summary . . . . .	139
8.2	Future Perspective . . . . .	142
	<b>Bibliography</b>	<b>144</b>
	<b>List of Publications</b>	<b>152</b>
	<b>List of Figures</b>	<b>158</b>
	<b>List of Tables</b>	<b>164</b>

# List of Tables

4.1	Physical properties of chromium isotopes. . . . .	50
4.2	Abundance of the stable chromium isotopes. . . . .	50
5.1	Experimental lifetimes of excited states in $^{75}\text{Kr}$ for positive-parity bands. Accepted lifetimes ( $\tau_{acc}$ ) represent the arithmetic average of the results measured at $148^\circ$ and $32^\circ$ . Excitation energies ( $E_x$ ), $\gamma$ -ray energies ( $E_\gamma$ ), branching ratio (Rb) and spins were taken from Ref. [5]. . . . .	80
5.2	Experimental lifetimes of excited states in $^{75}\text{Kr}$ for the negative-parity bands. Accepted lifetimes ( $\tau_{acc}$ ) represent the arithmetic average of the results measured at $148^\circ$ and $32^\circ$ . Excitation energies ( $E_x$ ), $\gamma$ -ray energies ( $E_\gamma$ ), branching ratio (Rb) and spins were taken from Ref. [5]. . . . .	80
5.3	Reduced transitional probability $B(E2)$ , transitional quadrupole moments $Q_t$ for the positive and negative-parity bands in $^{75}\text{Kr}$ obtained in the present experiment. . . . .	81
5.4	Configurations of 1- and 3-qp states with positive-parity as shown in Fig. 5.11. . . . .	88
5.5	Configurations of 1- and 3-qp states with negative-parity as shown in Fig. 5.12. . . . .	89

6.1	Experimental lifetimes of excited states in $^{75}\text{Br}$ for positive-parity bands. Accepted lifetimes ( $\tau_{acc}$ ) represent the weighted average of the results measured at $148^\circ$ and $32^\circ$ . Excitation energies ( $E_x$ ), $\gamma$ -ray energies ( $E\gamma$ ), and spins were taken from Ref. [94]. . . . .	102
6.2	Experimental lifetimes of excited states in $^{75}\text{Br}$ for the negative-parity bands. Accepted lifetimes ( $\tau_{acc}$ ) represent the weighted average of the results measured at $148^\circ$ and $32^\circ$ . Excitation energies ( $E_x$ ), $\gamma$ -ray energies ( $E\gamma$ ), and spins were taken from Ref. [94]. <sup>a</sup> and <sup>b</sup> represents data from Ref. [96] and [97], respectively. . . . .	103
6.3	Experimental lifetimes of excited states in $^{75}\text{Br}$ measured at $148^\circ$ for the positive-parity high lying K bands. Excitation energies ( $E_x$ ), $\gamma$ -ray energies ( $E\gamma$ ), and spins were taken from Ref. [94]. . . . .	103
6.4	Experimental lifetimes of excited states in $^{75}\text{Br}$ measured at $148^\circ$ for the negative-parity high lying K bands. Excitation energies ( $E_x$ ), $\gamma$ -ray energies ( $E\gamma$ ), and spins were taken from Ref. [94]. . . . .	104
6.5	Reduced transitional probability $B(E2)$ , transitional quadrupole moments $Q_t$ for the positive and negative-parity bands in $^{75}\text{Br}$ obtained from present experiment. . . . .	104
6.6	Reduced transitional probability $B(E2)$ , transitional quadrupole moments $Q_t$ of high K positive and negative-parity bands in $^{75}\text{Br}$ obtained from present experiment. . . . .	105
7.1	Single particle energies used in two different shell-model approaches. . .	126
7.2	Experimental [111] and theoretical low-lying states of $^{102}\text{Sn}$ . Energies are in MeV. . . . .	127
7.3	Experimental [112] and theoretical low-lying states (up to 4.5 MeV) of $^{104}\text{Sn}$ . Energies are in MeV. . . . .	128

7.4	Experimental [113] and theoretical low-lying states (up to 4.5 MeV) of $^{106}\text{Sn}$ . Energies are in MeV. . . . .	129
7.5	Experimental[115] and theoretical low-lying states (up to 4.5 MeV) of $^{108}\text{Sn}$ . Energies are in MeV. . . . .	131
7.6	Experimental [116] and theoretical low-lying states (up to 2.5 MeV) of $^{103}\text{Sn}$ . Energies are in MeV. . . . .	133
7.7	Experimental [117] and theoretical low-lying states (up to 2.5 MeV) of $^{105}\text{Sn}$ . Energies are in MeV. . . . .	135
7.8	Experimental [118, 26] and theoretical low-lying states (up to 2.5 MeV) of $^{107}\text{Sn}$ . Energies are in MeV. . . . .	136
7.9	Comparison of the yrast $B(E2; 0_{g.s.}^+ \rightarrow 2_1^+)$ values, obtained from the shell-model calculations with the measured values in $e^2b^2$ for even Sn isotopes. The experimental values have been taken from [30, 28] . . . . .	138

# List of Figures

2.1	Figure shows shell model orbitals. The simple harmonic oscillator levels (left) with the addition of an angular momentum dependent term ( $l^2$ ) attractive term to make the potential well more square (middle) and with the further addition of the spin orbit term (right). The shell model orbitals depends on the radial quantum number $n$ , the orbital quantum number $l$ and the total angular momentum $j$ . . . . .	10
2.2	Nilsson diagram for protons or neutron, $Z$ or $N \leq 50$ . Negative parity states are represented by dashed line, and positive with solid lines. . .	15
2.3	Orbitals around a prolate deformed nucleus, with their respective $\Omega$ projections. The different orbitals represent different $m$ states from the same $j$ -shell. . . . .	16
2.4	Deformation and nuclear rotation following the Lund convention. . . .	19
2.5	Total Routhian Surface calculation for the positive parity yrast band of $^{75}\text{Kr}$ at $\hbar\omega = 0.45$ MeV. . . . .	22
3.1	Figure shows the fusion evaporation reaction . . . . .	32
3.2	Figure showing the suppression of Compton continuum for $^{60}\text{Co}$ source and the improvement in the peak to total ratio. . . . .	39
3.3	Schematic diagram of the clover detector . . . . .	40
3.4	Figure showing the gain in efficiency due to addback . . . . .	41

3.5	The pictorial view of the Indian National Gamma Array setup at IUAC, New Delhi . . . . .	44
3.6	Block diagram of clover electronics . . . . .	46
3.7	Block diagram of the electronics for Compton Suppression . . . . .	47
3.8	Block diagram of the electronics for Master Gate . . . . .	47
4.1	Inside view of ultra high vacuum chamber used for deposition . . . . .	51
4.2	Graphite and Tantalum crucible used for keeping the target material inside . . . . .	52
4.3	A front view of enrich chromium target deposited on gold backing . . .	53
4.4	Typical spectra of the L x-rays of standard Cr target obtained from NIST and deposited Cr target . . . . .	54
4.5	Variation of gain shift for all 4 crystal of clover 16 during experiment .	56
4.6	The gain matching process . . . . .	57
4.7	Pictorial view of two-dimensional matrix . . . . .	60
4.8	Total 1-D projection spectrum . . . . .	61
4.9	Spectrum showing the gate on 191 keV transition of $^{75}\text{Kr}$ . . . . .	61
4.10	Figure shows the Doppler-shift-attenuation method . . . . .	66
4.11	Basic principle for DSAM technique . . . . .	67
5.1	Partial level scheme of $^{75}\text{Kr}$ relevant to the present work Ref. [5]. . . .	74
5.2	Gamma-ray spectrum created by gating on 187 keV transition of the yrast positive-parity band of $^{75}\text{Kr}$ . . . . .	76
5.3	Gamma-ray spectrum created by gating on 178 keV transition of the negative-parity band of $^{75}\text{Kr}$ . . . . .	76

- 5.4 Least-squares fits of line shape of some representative transitions in the positive parity bands: 824 keV, 896 keV and 1035 keV transitions. The left-hand frames show the data for the  $148^0$  backward detectors and right-hand frames show the data for  $32^0$  forward detectors in  $^{75}\text{Kr}$ . The contaminant peaks are shown by dotted lines. . . . . 78
- 5.5 Simultaneous line shape fits of some transitions in  $^{75}\text{Kr}$ : The left-hand frame show the simultaneous least square fits of 1195 and 1201 keV transitions at  $148^0$  and right-hand frame show simultaneous least square fits of 1180 and 1174 keV transitions at  $148^0$ . The contaminant peaks are shown by dotted lines. . . . . 79
- 5.6 Least-squares fits for line shapes of 916 and 1061 keV transitions of the negative-parity band. The left-hand frames show the data for the  $148^0$  backward detectors and right-hand frames show the data for  $32^0$  forward detectors in  $^{75}\text{Kr}$ . The contaminant peaks are shown by dotted lines. . . . . 79
- 5.7 Moment of inertia as a function of spin for the positive-parity band in  $^{75}\text{Kr}$ . . . . . 83
- 5.8 Moment of inertia as a function of spin for the negative parity band in  $^{75}\text{Kr}$ . . . . . 83
- 5.9 Comparison of the measured transitional quadrupole moments  $Q_t$  for excited states in the positive-parity bands in  $^{75}\text{Kr}$  with the prediction of the projected shell-model calculations. Circles represents the data from present measurements and the square for previous work reported in Ref. [5], respectively. Filled (open) symbols stand for positive (negative) signature band. . . . . 84

5.10	Comparison of the measured transitional quadrupole moments $Q_t$ for excited states in the negative-parity bands in $^{75}\text{Kr}$ with the prediction of the projected shell-model calculation. Circles represents the data from present measurements and the square for previous work reported in Ref. [5], respectively. Filled (open) symbols stand for positive (negative) signature band. . . . .	85
5.11	Band diagram for the positive parity band in $^{75}\text{Kr}$ . . . . .	88
5.12	Band diagram for the negative parity band in $^{75}\text{Kr}$ . . . . .	89
5.13	Total Routhian Surface (TRS) plots in the $\beta_2 - \gamma$ plane for positive-parity band of $^{75}\text{Kr}$ . Plots are for two rotational frequencies, $\hbar\omega = 0.30$ MeV (top frame) and $\hbar\omega = 0.65$ MeV (bottom frame) corresponding to before and after band crossing, respectively. . . . .	91
5.14	Total Routhian Surface (TRS) plots in the $\beta_2 - \gamma$ plane for negative-parity band of $^{75}\text{Kr}$ . Plots are for two rotational frequencies, $\hbar\omega = 0.30$ MeV (top frame) and $\hbar\omega = 0.65$ MeV (bottom frame) corresponding to before and after band crossing, respectively. . . . .	92
6.1	Partial level scheme of $^{75}\text{Br}$ relevant to the present work Ref. [94]. . .	97
6.2	Gamma-ray spectrum created by gating on 830 keV transition of the yrast positive-parity band of $^{75}\text{Br}$ . . . . .	98
6.3	Gamma-ray spectrum created by gating on 518 keV transition of the favored signature partner of negative-parity band in $^{75}\text{Br}$ . . . . .	98
6.4	Gamma-ray spectrum created by gating on 654 keV transition of the unfavored signature partner of negative-parity band in $^{75}\text{Br}$ . . . . .	99

- 6.5 Least squares fits for line shape of 830 keV and 1046 keV transitions of the positive parity band. The left-hand frames show the data for the  $148^0$  backward detectors and right-hand frame show the data for  $32^0$  forward detectors in  $^{75}\text{Br}$ . The contaminant peaks are shown by dotted line. . . . . 101
- 6.6 Least-squares fits for line shape of 1075 keV and 1192 keV transitions of negative parity band. The left-hand frames show the data for the  $148^0$  backward detectors and right-hand frames show the data for  $32^0$  forward detectors in  $^{75}\text{Br}$ .The contaminant peaks are shown by dotted line. . . . 101
- 6.7 Least-squares fits for line shape of some representative transitions of different bands: 1072 keV, 922 keV, 947 keV and 1117 keV transitions for the  $148^0$  backward detectors in  $^{75}\text{Br}$ .The contaminant peaks are shown by dotted line. . . . . 102
- 6.8 Moment of inertia as a function of spin for the positive parity bands in  $^{75}\text{Br}$ . . . . . 106
- 6.9 Moment of inertia as a function of spin for the negative parity bands in  $^{75}\text{Br}$ . . . . . 106
- 6.10 Comparison of the measured transitional quadrupole moments  $Q_t$  for excited states in the positive-parity bands in  $^{75}\text{Br}$  with the prediction of the projected shell-model calculation. Circles represents the data from present measurements and the square for previous work reported in Ref. [94], respectively. Filled (open) symbols stand for positive (negative) signature band. . . . . 107

6.11	Comparison of the measured transitional quadrupole moments $Q_t$ for excited states in the negative-parity bands in $^{75}\text{Br}$ with the prediction of the projected shell-model calculation. Circles represents the data from present measurements and the square for previous work reported in Ref. [94], respectively. Filled (open) symbols stand for positive (negative) signature band. . . . .	108
6.12	Experimental transitional quadrupole moments $Q_t$ as a function of spin for positive parity high K bands in $^{75}\text{Br}$ . . . . .	109
6.13	Comparison of the measured transitional quadrupole moments $Q_t$ for excited states in the negative-parity high K bands in $^{75}\text{Br}$ with the prediction of the projected shell-model calculation. . . . .	109
6.14	Total Routhian Surface (TRS) plots in the $\beta_2 - \gamma$ plane for positive parity band of $^{75}\text{Br}$ . Plots are for two rotational frequencies, $\hbar\omega = 0.30$ MeV (top frame) and $\hbar\omega = 0.70$ MeV (bottom frame) corresponding to before and after band crossing, respectively. . . . .	112
6.15	TRS plots in the $\beta_2 - \gamma$ plane for negative-parity $+1/2$ signature band of $^{75}\text{Br}$ . Plots are for three rotational frequencies, $\hbar\omega = 0.30$ MeV (top frame), $\hbar\omega = 0.50$ MeV (middle frame) and $\hbar\omega = 0.70$ MeV (bottom frame). . . . .	114
6.16	TRS plots in the $\beta_2 - \gamma$ plane for negative-parity $-1/2$ signature band of $^{75}\text{Br}$ . Plots are for three rotational frequencies, $\hbar\omega = 0.30$ MeV (top frame), $\hbar\omega = 0.50$ MeV (middle frame) and $\hbar\omega = 0.70$ MeV (bottom frame). . . . .	115
7.1	Experimental [111] and calculated energy levels of $^{102}\text{Sn}$ with sn100 and snet interactions. . . . .	128
7.2	Same as Fig. 7.1 for $^{104}\text{Sn}$ . . . . .	129
7.3	Same as Fig. 7.1 for $^{106}\text{Sn}$ . . . . .	130

7.4	Same as Fig. 7.1 for $^{108}\text{Sn}$ . . . . .	131
7.5	Comparison of energy of the first $2^+$ excited state from shell model calculations with experimental data for even Sn isotopes with A ranging from 102 to 108. . . . .	132
7.6	Comparison of energy of the first $4^+$ excited state from shell model calculations with experimental data for even Sn isotopes with A ranging from 102 to 108. . . . .	132
7.7	Experimental[116] and calculated energy levels of $^{103}\text{Sn}$ with sn100pn and snet interactions. . . . .	134
7.8	Same as Fig. 7.7 for $^{103}\text{Sn}$ . . . . .	134
7.9	Same as Fig. 7.7 for $^{107}\text{Sn}$ . . . . .	136
7.10	Comparison of energy of the first $7/2^-$ excited state from shell model calculations with experimental data for odd Sn isotopes with A ranging from 103 to 107. . . . .	137

# Chapter 1

## Introduction

The discovery of nucleus by Rutherford in 1911 laid the foundation of the new branch of physics called '*nuclear physics*'. In subsequent years, the discovery of neutron and the invention of accelerators, which enabled different probes to be used, helped this field to grow. Simultaneously, a basic understanding of nuclear structure and reactions in terms of quantum mechanics was achieved. The growth of nuclear physics has been further accelerated by the rapid development of versatile accelerators, wide ranging radiation detectors, fast electronics and high speed computational facilities. In recent past nuclear physics has developed as the key part, since it has a link with many branches of science and technology. Over the years, various discoveries in nuclear physics have not only improved our understanding on basic building blocks of matter, but also it has contributed in societal benefits such as nuclear energy, use of radioisotopes in medical treatments etc.

The atomic nucleus is a fascinating quantum-mechanical many body system consisting of nucleons (protons and neutrons) and the ultimate aim of nuclear physics continues to be the determination of the nature of nuclear force operating between the nucleons and to extend this knowledge to further understand the behavior of collection of nucleons, usually referred to as nuclear structure. In studying the nuclear structure one can observe the change in nuclear properties when different quantum states are occupied by nucleons. The behavior of the nucleus when stressed by rapid rotation i.e., at high spin allows us to observe the interplay between single particle and collective mo-

tions. The current status of nuclear physics research is such that one is now interested in exploring the nuclear structure under extreme conditions of energy, temperature, angular momentum, large or small  $N/Z$  ratio and extending the range of nuclei to ones far from the line of stability and finally understanding of nuclear structure is obtained through comparison of measured nuclear properties with the model predictions.

## 1.1 Motivation of the Thesis

One of the fundamental problems in the study of nuclear structure is to understand the interplay of single particle motion governed by the Pauli principle and coherence in nuclear wave functions. A nucleus with few nucleons outside the closed shell is spherical in structure and exhibits the single particle behavior. As more valence nucleons are added beyond closed shells, residual interaction leads to configuration mixing and hence the nearly rigid spherical structure softens as deformation and collectivity build up. An important aspect of nuclear structure is the investigation of stability of collective phenomenon at extremes of angular momentum and excitation energy which is possible due to the advancement of heavy ion accelerators and sophisticated Ge gamma detectors arrays having high energy resolution and increased photo peak efficiency for  $\gamma$ -ray detection. The spectroscopic studies of nuclei under extreme condition is a renaissance in the study of nuclear structure.

### 1.1.1 Some features of $A \approx 70 - 80$ mass region

The nuclei in the mass region  $A = 70 - 80$  form rich ground for the testing of various competing models like, single particle and collective models and display a large variety of structural effects. When both the proton and neutron number in this region lie close to the mid shell ( $Z = N = 39$ ), high deformation [1, 2] and rigid rotational behavior are common. As  $Z$  or  $N$  varies away from mid shell transitional effect such as shape coexistence and  $\gamma$  softness can occur. At the  $N = 50$ , spherical shell-model behavior is observed. The large number of valence particles in f-p-g shell strongly correlate with the high quadrupole deformation  $\beta_2 = 0.35 \sim 0.4$ , measured in this region.

Variation in the coupling between quasi particles and the core can lead to rapid shape changes [3] and varying degrees of signature splitting. Because of its high intrinsic spin the unique parity  $g_{9/2}$  orbital plays a large role in the structure of yrast and near yrast high spin states in this mass region. The light neutron deficient isotopes form a widespread well studied path across this mass region of deformation exhibiting shape coexistence of prolate, oblate shapes [4, 5], triaxial deformation, competing proton and neutron configurations [6], M1 bands [7], large shape changes caused by quasi-particle alignment [8, 3], smooth band termination [9] etc. The odd A isotopes provide an opportunity to clarify the role of quasi-particle alignment through the Pauli blocking and to investigate the deformation driving effect of different quasi-particle orbits. Magnetic transitions in the odd isotopes provide valuable information about the triaxial degree of freedom and the interaction between deformation and rotation aligned quasi particles.

The nuclei in the mass  $A = 70 - 80$  region are gaining importance due to development of new experimental techniques on one side and availability of various theoretical studies based on different models on the other side. The first example of shape coexistence in this mass region was found in  $^{72}\text{Se}$  by Hamilton et al. [10]. Total Routhian Surface (TRS) calculations predict more than one minima in the nuclear potential energy surfaces, corresponding to the prolate-oblate shape coexistence and triaxial shapes. Nazarewicz et al. [11] have calculated competing minimas at quadrupole deformations  $\beta_2 = +0.38$ (prolate) and  $\beta_2 = -0.30$ (oblate) for both Kr and Sr ( $N < 40$ ). Another interesting feature of  $N \simeq Z$  nuclei with increasing angular momentum is the loss of collectivity which finally leads to the band termination and is seen, for instance, in  $^{73}\text{Br}$  [9].

$^{75}\text{Br}$  and  $^{75}\text{Kr}$  lie in the region of transitional neutron deficient nuclei with  $Z = 35$  and  $36$ , where strong variations of collective properties have been observed as functions of both neutron and proton number. In fact, nuclei with  $Z = 37$  or  $38$  are amongst the best collective rotors known with quadrupole deformation  $\beta_2 = 0.38$ . On the other hand, nuclei with  $Z < 34$  are much less deformed. Neutron deficient Kr and Br isotopes lie in the center of this region.

The lifetimes of high spin states in this mass region can give us valuable information about the phenomenon like shape coexistence, alternating pattern of magnetic transition strength and shape changes as a function of spin. These states have lifetime in the range of  $<1$  ps, that is accessible only by Doppler-shift attenuation method (DSAM). In view of the above discussion we are motivated to do lifetime measurements of higher spin states using DSAM technique to understand various phenomenon occurring in this mass region.

### 1.1.2 Some features of $A \approx 100$ mass region

The nuclear structure studies near the  $^{100}\text{Sn}$  region have been burning topic of research from last two decades. The reason is that  $^{100}\text{Sn}$  is the heaviest doubly magic  $N = Z$  nucleus, which may show strong shell closure and is accessible to experimental investigations. A handful of nuclei are investigated near the  $^{100}\text{Sn}$  region in few experiments and excited states have been identified in neighboring nuclei e.g.  $^{98}\text{Ag}$  [12],  $^{99}\text{Ag}$  [13],  $^{102}\text{Cd}$  [14],  $^{102}\text{In}$  [15],  $^{103}\text{Sn}$  [16] and  $^{107}\text{In}$  [17]. Nuclei in this mass region are mostly characterized by small deformation at low spins and generation of angular momentum in them proceeds through the gradual alignment of the spin vectors of the nucleons in the valence orbitals along the symmetry axis. However, at higher spins typical collective band structures are observed, due to orbitals from  $\nu h_{11/2}$  which act as intruder states giving rise to larger prolate deformation.

With the increase in the number of particle and holes away from the shell closure, other excitation mechanisms have begin to have a significant contribution e.g. Band termination, Magnetic and Antimagnetic rotation etc. A novel mode of excitation arises in nearly spherical nuclei due to occupation of valence proton and neutron in  $g_{9/2}$  and  $h_{11/2}$  orbitals. Such high-j orbitals are now well known for the generation of rotation like sequence of  $M1$  transition called '*shares bands*' and have been observed in both lead and recently in tin region [18, 19] which are characterized by strong  $M1$  transitions with weak  $E2$  crossover transitions. In this case although the charge distribution is almost spherical, the magnetic dipole rotates leading to the appearance of magnetic dipole transition, with large  $B(M1)$  values indicating strong magnetic char-

acter.

Another mechanism of excitation which leads to the generation of rotational bands is that of particle-hole excitation across the  $Z = 50$  shell gap. This involves the occupation of intruder  $h_{11/2}$  orbital in addition to  $g_{9/2}$  subshell. With the advent of third generation arrays of  $\gamma$ -detectors like GAMMASPHERE [20], EUROGAM [21] and INGA [22] it has become possible to study a very rare reaction channels especially on the neutron deficient side of the nuclide chart. It has been observed that these rotational structures gradually loose their collectivity and the nuclear shape transforms from collective near prolate ( $\gamma = 0^\circ$ ) at low spin to non-collective near oblate ( $\gamma = 60^\circ$ ) at the 'band termination' [23, 24, 25]. This occurs when all of the valence nucleons become aligned, and at this point the rotational band must terminate, having exhausted all of the angular momentum available in the configuration.

A lot of  $\beta$ -decay [26, 27] and Coulomb excitation [28, 29, 30, 31] experiments at radioactive beam facilities have been carried out around the world which are focused on the low-spin states and provide the valuable information of low-lying states and on the electromagnetic transition strength  $B(E2)$  which is a very sensitive tool for nuclear structure studies.

## 1.2 Plan of the Thesis

The thesis is broadly divided into two parts :

- I. Experimental study of  $^{75}\text{Kr}$  and  $^{75}\text{Br}$  nuclei.
- II. Theoretical study of  $^{102-108}\text{Sn}$ .

In order to study the evolution of shapes at high spin states in 70 - 80 mass region, an experiment was planned to measure the lifetimes of these states using Indian National Gamma Array (INGA) at Inter University Accelerator Centre, New Delhi, India. The following heavy-ion fusion evaporation reaction were used to populate the high spin states in  $A = 75$ , Krypton and Bromine nuclei,

- $^{50}\text{Cr}(^{28}\text{Si}, 2\text{pn})^{75}\text{Kr}$  at 90 MeV of beam energy.

- $^{50}\text{Cr}(^{28}\text{Si}, 3\text{p})^{75}\text{Br}$  at 90 MeV of beam energy.

Excited states in  $A = 75$ , Krypton and Bromine nuclei were investigated through in-beam  $\gamma$ -ray spectroscopy techniques following population in the heavy-ion fusion-evaporations. In the present work, the aim was to study experimentally the shapes of the nuclei in this mass region at high spin and excitation energy. Emphasis was given to investigate the effects of quasi-particle (proton or neutron) alignment on the shapes of various nuclei in this mass region. These effects can be studied by populating the nuclei to higher spins and excitation energy where particle alignment takes place. The direct determination of nuclear shape is possible by measuring the lifetimes of the levels. From the lifetime measurement one can calculate the reduced transition probability and transitional quadrupole moments  $Q_t$ , which are direct measurement of nuclear shapes. To study such shape evolution at high spin, we have studied experimentally odd  $A = 75$ , Kr and Br nuclei by measurement of lifetimes beyond the band crossing. The results obtained are interpreted in terms of the projected shell-model and cranking model with Woods Saxon potential. Lifetimes of these excited states were determined using Doppler-shift attenuation method (DSAM). The emitted  $\gamma$ -rays were detected with the help of a powerful multi detector array consisting of Compton-suppressed clover detector called Indian National Gamma Array (INGA) at Inter University Accelerator Centre, New Delhi. The experiment was performed using heavy ion beam provided by 15 UD Pelletron accelerator. The recorded coincidence events from in beam  $\gamma$ -ray spectroscopy measurement were stored into two dimensional  $E_\gamma$ - $E_\gamma$ , 4K matrices using INGASORT program. The background subtracted coincidence spectra were generated and used for further line shape analysis.

Concept of nuclear shell closure came into picture in 1949 by Mayer [32], from that to till recently, new tool have been developed which makes further study of this topic possible. With the advent of radioactive ion beams and on-line mass separator, the experimental and theoretical studies are currently focussed on the nuclear structure

evolution far from the line of stability.

The theoretical study of Sn isotopes is interesting as it can provide a unique testing ground for nuclear structure calculations. In the present work, large scale shell model calculation have been performed for neutron deficient even  $^{102-108}\text{Sn}$  and odd  $^{103-107}\text{Sn}$  isotopes using more recent data of single particle spectrum and realistic interactions obtained by renormalization of Bonn and Paris potentials. The calculation have been performed by taking  $^{100}\text{Sn}$  core consisting of  $1g_{7/2}$ ,  $2d_{5/2}$ ,  $2d_{3/2}$ ,  $3s_{1/2}$  and  $1h_{11/2}$  single particle state.

This thesis consists of eight chapters. Following this introduction chapter, brief descriptions of the various theoretical models used have been given in **Chapter 2**. We present a brief account of the basic models such as spherical shell and deformed models. Thereafter, the cranking shell-model using Woods-Saxon potential and projected shell-model is described in detail. In **Chapter 3** various experimental techniques used in  $\gamma$ -ray spectroscopy and detection of  $\gamma$ -ray using clover detectors have been described. Need for large gamma ray detector arrays with special focus on Indian National Gamma Array at IUAC, New Delhi and their related data acquisition system are discussed at length. In **Chapter 4** fabrication of target using rolling and deposition technique followed by data analysis techniques used in in-beam  $\gamma$  spectroscopy have been presented. The methods of measurement of lifetimes of excited states and the extraction of  $Q_t$  from the measured lifetimes is also described. In subsequent chapters, the details of the nuclei studied, the results obtained and the interpretation of the results are discussed. In all these chapters, first an introduction is given summarizing the previous work carried out on the particular nucleus and next the aim of present work is described. This is followed by description of the experimental details and data analysis in the study of the particular nucleus and the results obtained. Finally, discussion and interpretation of the results has been presented. **Chapters 5 and 6** are devoted to lifetime measurements of high spin states and consequently the shape evolution in  $A = 75$ , Krypton and Bromine nuclei have been described. **Chapter 7** deals with theoretical large scale shell model calculation for proton rich Sn isotopes. Finally, the summary and conclusions along with a future outlook have been presented in **Chapter 8**.

# Chapter 2

## Theoretical Models

### 2.1 Introduction

The nucleus is a many-body system of strongly interacting fermions. The study of high spins or fast rotating nuclei forms one of the most important interests in nuclear structure physics. The fast rotating nuclei exhibit many interesting modes of excitations due to collective motion of nucleons or single particle effects or some exotic features due to the interplay between these two properties. To understand such excitations and to explain the underlying physical mechanism many nuclear models have been developed over the years. The aim of such studies is to understand the experimentally observed properties of nuclei by microscopic models using effective nucleon-nucleon interaction.

The *Liquid Drop Model(LDM)* proposed by Bohr and Wheeler is one of the primitive models. In this model the nucleus is considered as a liquid drop because it has very low compressibility and well defined surface. The nucleus was characterized by mass number  $A$  and its atomic number  $Z$ . This model could explain the most basic properties like binding energy and mass of the nucleus. It also explains the nuclear fission resulting from the large amplitude oscillation in nuclei. However, it was unsuccessful in explaining the discontinuities in certain nuclear properties like, the separation energy (the energy required to remove a nucleon from the nucleus), the quadrupole moment etc. at nucleon numbers 2, 8, 20, 28, 50, 82 and 126. These are called the *magic numbers*. These nuclei were found to have extra stability when the nucleon number is any of these. This extra binding gave birth to shell model of the nucleus.

## 2.2 Nuclear Shell Model

The nuclear shell model is a model of the atomic nucleus which uses the Pauli exclusion principle to describe the structure of the nucleus in terms of energy levels. The strong analogy of magic numbers found in atomic physics led to the development of the nuclear *shell model*. The *shell model* or the independent particle model proposed that nuclei have shell structure as it is a quantal system. The basic assumption of this model [32, 33] is that, each nucleon (proton or neutron) moves independently in a potential that represents the average interaction with the other nucleons in the nucleus.

Taking only two-body forces into account, the Schrodinger equation for  $A$  nucleons considering the sum over the kinetic-energy terms  $T(K)$  and the two-body nucleon-nucleon interaction  $V(K,l)$ ,

$$H\psi(1, 2, \dots, A) = \left[ \sum_{K=1}^A T(K) + \sum_{1=K<l}^A V(K, l) \right] \psi(1, 2, \dots, A) = E\psi(1, 2, \dots, A) \quad (2.1)$$

An exact solution of such a many-body problem can be rarely obtained except for the lightest masses. Therefore the first step towards an approximate solution is to introduce a single-particle potential  $U(K)$  by writing the Hamiltonian as:

$$H = \sum_{K=1}^A [T(K) + U(K)] + \left[ \sum_{1=K<l}^A V(K, l) - \sum_{1=K<l}^A U(K) \right] = H^{(0)} + H^{(1)} \quad (2.2)$$

Here  $H^{(0)}$  defines the independent-particle motion and  $H^{(1)}$  represents a residual interaction reflecting the fact that the particles do not move completely independently. In the interacting shell-model (SM) approach the spherical mean field produced by the closed core—the  $H^{(0)}$  part—is a standard phenomenological single-particle potential given by a harmonic oscillator. Configuration mixing between all valence nucleons outside the core—interacting through the  $H^{(1)}$  part—are taken into account for describing nuclei in a given model space. The shell model approach focuses on the properties of the residual interaction between valence nucleons. If full calculation can not be performed, a core is introduced which leads to the so called effective residual interaction.

The resulting shell model orbits are shown in Fig. 2.1 and characterized by the set of

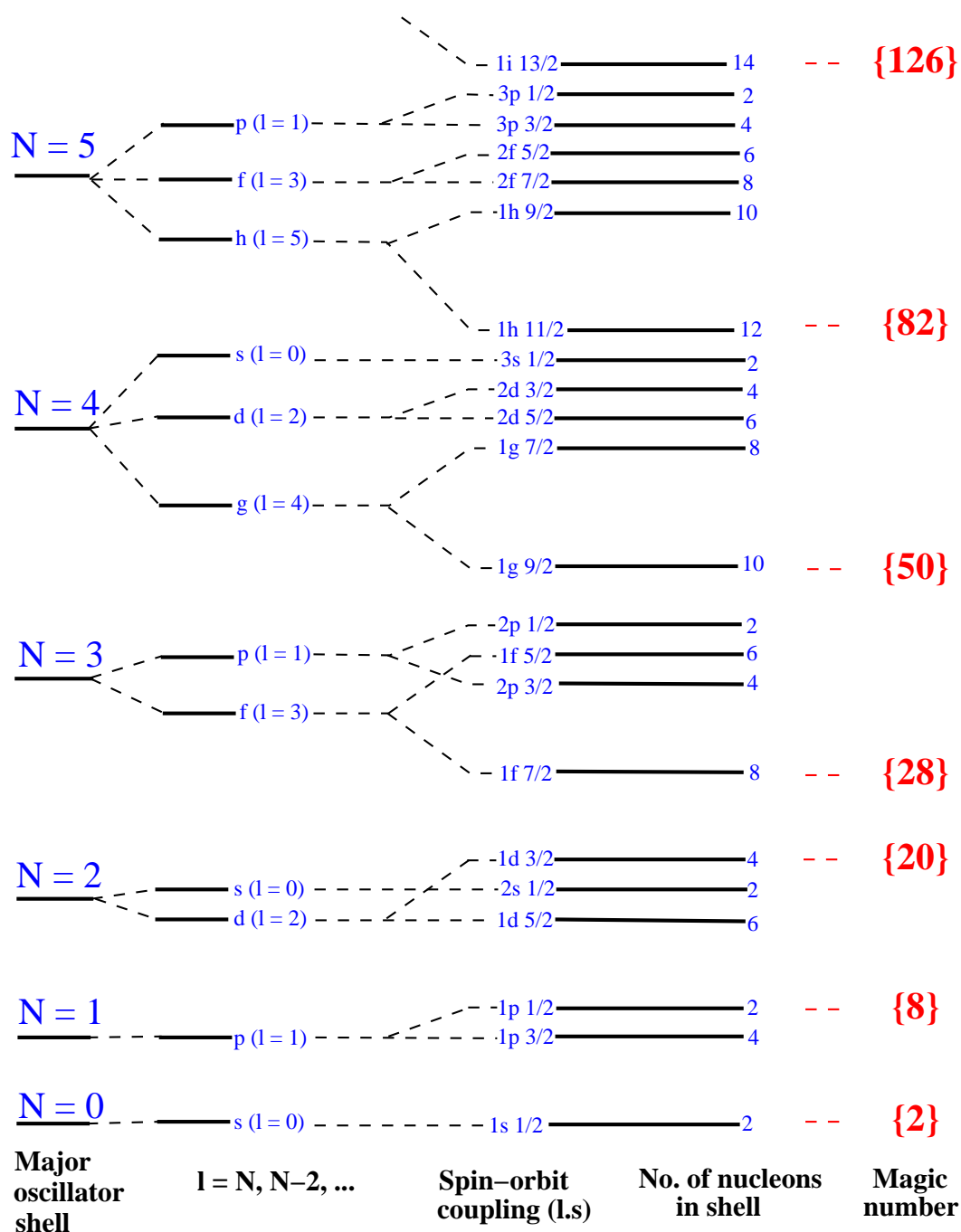


Figure 2.1: Figure shows shell model orbitals. The simple harmonic oscillator levels (left) with the addition of an angular momentum dependent term ( $l^2$ ) attractive term to make the potential well more square (middle) and with the further addition of the spin orbit term (right). The shell model orbitals depends on the radial quantum number  $n$ , the orbital quantum number  $l$  and the total angular momentum  $j$

quantum numbers  $(n, l, j, N)$  where  $n$  is the radial quantum number,  $l$  is the orbital quantum number and  $j$  is the total angular momentum and  $N$  is the major oscillator quantum number. The single particle orbitals obtained in shell model are  $(2j + 1)$  fold degenerate.

This model is known as “shell model” because of the grouping of energy levels into “shells” which are represented by large energy gaps. The Hamiltonian describing the residual interaction between valence nucleons outside a closed shell have two parts monopole and multipole.  $H_{monopole}$  is related to the evolution of the spherical mean field and determines the position of single particle energy levels. The monopoles can also be broken into central, spin-orbit and tensor forces, as for the bare  $NN$  forces. The higher-order multipoles determine correlations which are not present in the spherical mean field and are responsible for configuration mixing between levels and the relative energy splitting between different angular momentum states. With this potential, the shell model was able to reproduce the spherical magic numbers and also explain some other properties of almost all spherical nuclei, for example the ground state spins and parities and also the energy spectra of various nuclei. This model was limited to nuclei which do not deviate from the spherical shape in the ground state. But, as we go away from the shell closure it was found nuclei are deformed. To explain this deformed nuclei the Nilsson model (deformed shell model) came into picture. The deformation parameters to characterize a deformed nucleus and the Nilsson is model will be explained in the following section.

## 2.3 Deformation parameters

The nuclear surface can be expanded in terms of spherical harmonics [34]

$$R(\theta, \phi) = R_0 \left[ 1 + \sum_{\lambda=0}^{\infty} \sum_{\mu=-\lambda}^{\lambda} \alpha_{\lambda\mu} Y_{\lambda\mu}(\theta, \phi) \right] \quad (2.3)$$

Here,  $R_0$  represents the radius of the spherical nucleus. As  $R(\theta, \phi)$  has to be real, this demands,

$$\alpha_{\lambda\mu}^* = (-1)^\mu \alpha_{\lambda-\mu}$$

$\lambda$  describes the different modes of deformation. For example,  $\lambda = 0$  describes the change in nuclear volume. As the nucleus is highly incompressible, the  $\lambda = 0$  mode can be neglected. Similarly, it can be shown [34] that the  $\lambda = 1$  mode describes the translation of the nucleus as a whole for small deformation. Hence, for small deformation this mode can also be neglected. The lowest order term one considers for nuclear deformation is the  $\lambda = 2$  term, the quadrupole deformation. Now, the radius expansion in equation 2.3 becomes

$$R(\theta, \phi) = R_0 \left[ 1 + \sum_{\mu=-2}^{+2} \alpha_{2\mu} Y_{2\mu}(\theta, \phi) \right] \quad (2.4)$$

For axially symmetric shapes,  $\alpha_{2\mu}$  terms vanish except for  $\mu = 0$  and this  $\alpha_{20}$  defines the quadrupole deformation and is denoted by  $\beta_2$ .

For non-axially symmetric deformations, there are five parameters  $\alpha_{2\mu}$  which define the shape. In such cases, one can make a suitable rotation of the co-ordinate system through Euler angles  $\Omega (= \theta_1 \theta_2 \theta_3)$  such that the three axes of the new (body fixed) co-ordinate system coincide with the three principal axes of the ellipsoid. Then, the parameter  $\alpha_{\lambda\mu}$  transform as

$$\alpha_{\lambda\mu} = \sum_{\mu'} D_{\mu\mu'}^\lambda(\Omega) \alpha_{\lambda\mu'}$$

Where,  $D_{\mu\mu'}^\lambda(\Omega)$  are the Wigner  $D$ -functions. Under such a transformation, it can be shown [34] that that five co-efficients reduce to two real variables,  $\alpha_{20}$  and  $\alpha_{22} = \alpha_{2-2}$  with  $\alpha_{21} = \alpha_{2-1} = 0$ . These together with the Euler angles give complete description of the system.

For convenience, D. L. Hill and J. A. Wheeler [35] introduced the  $\beta_2$  and  $\gamma$  parameters through the relations,

$$\alpha_{20} = \beta_2 \cos \gamma$$

$$\alpha_{22} = \frac{1}{\sqrt{2}} \beta_2 \sin \gamma$$

With the above definitions, equation 2.4 can be written as,

$$\begin{aligned} R(\theta, \phi) &= R_0 [1 + \alpha_{20} Y_{20}(\theta, \phi) + \alpha_{22} Y_{22}(\theta, \phi) + \alpha_{2-2} Y_{2-2}(\theta, \phi)] \\ &= R_0 [1 + \beta_2 \cos \gamma \sqrt{\frac{5}{16\pi}} (3 \cos^2 \theta - 1) + \frac{1}{\sqrt{2}} \beta_2 \sin \gamma \sqrt{\frac{15}{32\pi}} \sin^2 \theta (e^{2i\phi} + e^{-2i\phi})] \\ &= R_0 [1 + \sqrt{\frac{5}{16\pi}} (3 \cos^2 \theta - 1) \beta_2 \cos \gamma + \sqrt{\frac{15}{64\pi}} 2 \sin^2 \theta \cos 2\phi \beta_2 \sin \gamma] \end{aligned}$$

Hence,

$$R(\theta, \phi) - R_0 = \sqrt{\frac{5}{16\pi}} \beta_2 R_0 [\cos \gamma (3 \cos^2 \theta - 1) + \sqrt{3} \sin \gamma \sin^2 \theta \cos 2\phi]$$

In the above equation,  $\beta_2$  measures the degree of deformation, while the  $\gamma$  measures the degree of non-axiality.

From the above definition,  $\beta_2 = 0$ , implies spherical nucleus,  $\gamma = 0^\circ$  defines an axially symmetric prolate shape and  $\gamma = 60^\circ$  corresponds to an axially symmetric oblate shape. For  $\gamma$  values between  $0^\circ$  and  $60^\circ$ , the nucleus has a triaxial shape.

## 2.4 Nilsson Model

In this deformed shell model [36, 37], an anisotropic harmonic oscillator is taken as the average potential. Then, the Hamiltonian can be written as,

$$H = -\frac{\hbar^2}{2m} \nabla^2 + \frac{m}{2} r^2 (\omega_x^2 + \omega_y^2 + \omega_z^2) + Cl.s + D(l^2 - \langle l^2 \rangle) \quad (2.5)$$

where,  $\omega_{i=x,y,z}$  are the oscillator frequencies corresponding to the three axes and given by,

$$\omega_x = \omega_0(\epsilon, \gamma) \left[ 1 - \frac{2}{3} \epsilon \cos\left(\gamma + \frac{2\pi}{3}\right) \right] \quad (2.6)$$

$$\omega_y = \omega_0(\epsilon, \gamma) \left[ 1 - \frac{2}{3} \epsilon \cos\left(\gamma - \frac{2\pi}{3}\right) \right] \quad (2.7)$$

$$\omega_z = \omega_0(\epsilon, \gamma) \left[ 1 - \frac{2}{3} \epsilon \cos(\gamma) \right] \quad (2.8)$$

where, the Nilsson parameter  $\epsilon$  is related to the Hill - Wheeler deformation  $\beta_2$  by the relation  $\epsilon \approx 0.95\beta_2$ . The frequencies are chosen to be proportional to the half axes  $a_x, a_y, a_z$  of the ellipsoid. In the case of axially symmetric shape,

$$\omega_x = \omega_y = \omega_0(\epsilon) \left( 1 + \frac{1}{3} \epsilon \right) = \omega_{\perp}$$

$$\omega_z = \omega_0(\epsilon) \left( 1 - \frac{2}{3} \epsilon \right)$$

with  $\omega_0 = \omega_0^0 \left( 1 + \frac{2}{3} \epsilon \right)$

The eigen states of the Hamiltonian can be labeled by the quantum numbers  $Nl_j m$  of the spherical single-particle states.

The only quantum numbers that remain conserved are parity  $\pi$  and the projection of the particle angular momentum  $j$  on the symmetry axis. The plot of the energy of different levels as a function of the deformation parameter  $\epsilon$  is known as the Nilsson diagram (see Figure 2.2). The positive value of  $\epsilon$  represents a prolate shape, while the negative value is for oblate shape. In the Nilsson diagram, the spherical magic numbers appear at 2, 8, 20, 28, 50, 82 and 126, appear at  $\epsilon = 0$ . In addition, there are other magic numbers which appear at different deformations or particle numbers other than spherical numbers. For example, in the  $A \sim 80$  region shell gaps occur for particle numbers 34, 38, for prolate deformation and at 36 for oblate deformation. In the

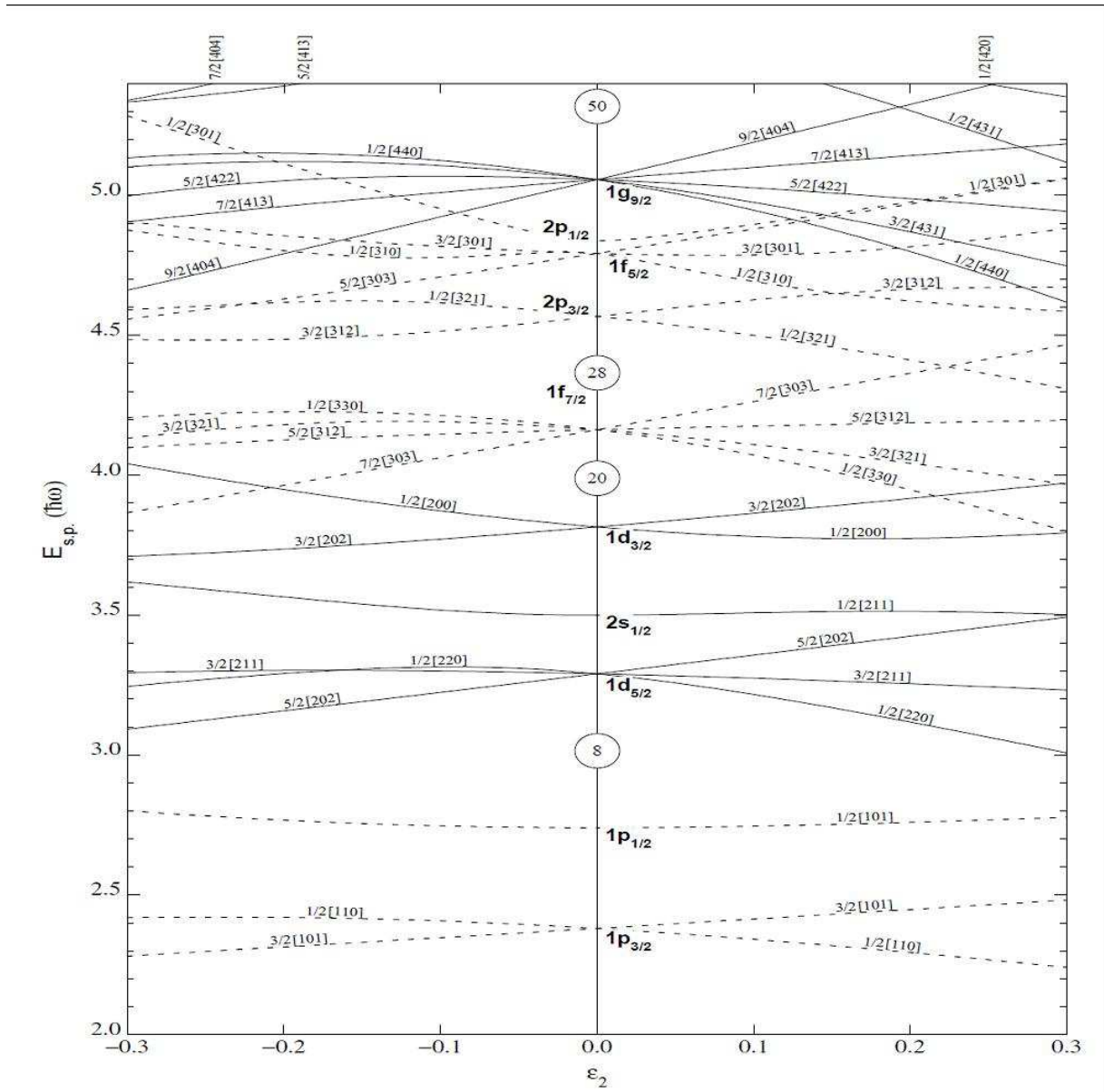


Figure 2.2: Nilsson diagram for protons or neutron,  $Z$  or  $N \leq 50$ . Negative parity states are represented by dashed lines, and positive parity states by solid lines.

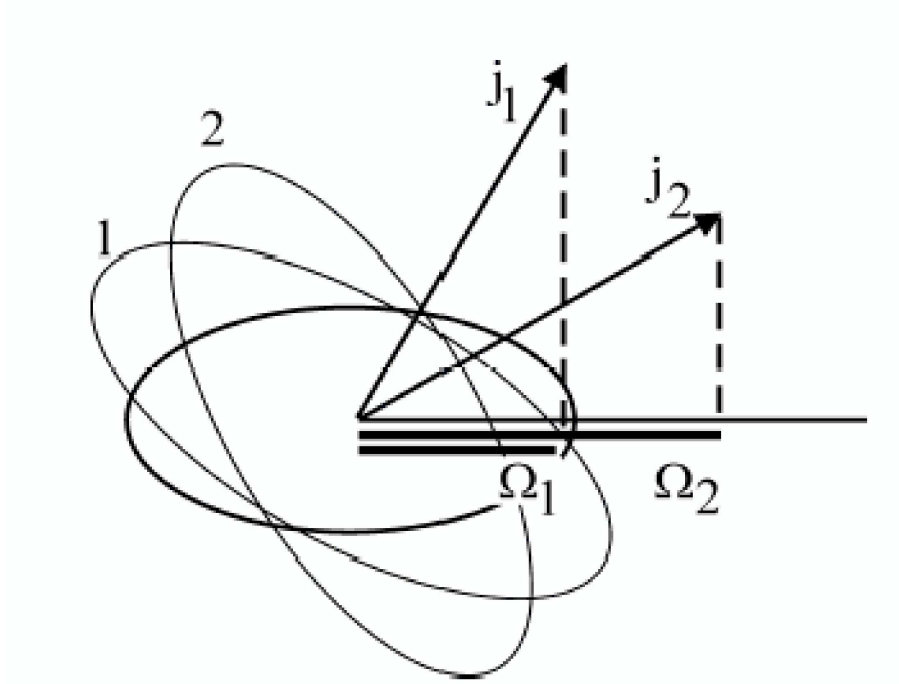


Figure 2.3: Orbitals around a prolate deformed nucleus, with their respective  $\Omega$  projections. The different orbitals represent different  $m$  states from the same  $j$ -shell.

higher mass region i.e. rare earth and above, the shell gaps occur at nucleon numbers 66, 70, 76 for prolate deformation and at 80 for oblate deformation. These numbers are called the deformed magic numbers. These play an important role in stabilizing the nuclear shape. From the Figure 2.2 one can observe in a particular  $j$ -multiplet, low  $\Omega$  values are energetically favored compared to the higher ones. This can be understood by the fact that nuclei have a very short range force and a particle in low  $K$  orbital has a larger overlap with the rest of the nuclear matter as shown in Fig. 2.3 and reverse is true for oblate shape.

## 2.5 Total Energy-Shell correction

In order to calculate the total energy of nucleus, Strutinsky [38, 39] has introduced a new powerful method called Strutinsky shell correction method which postulates that total energy of nucleus can be split into a sum of,

$$E_{Tot} = E_{LDM} + E_{sh} \quad (2.9)$$

The  $E_{LDM}$  term represents the macroscopic part of energy which is calculated by using a Liquid drop model to describe the the nuclear binding energy depending smoothly on  $A$  and  $Z$ , and a shell correction term  $E_{sh}$  which represents microscopic part of energy arising out of fluctuation in the level density and is defined as shell correction for the proton and neutron. To calculate this correction one needs to subtract the "smoothly varying" part of the sum of the single particle energies. The true distribution of the single particle energies is given by,

$$g(\epsilon) = \sum_{i=1}^{\infty} \delta(\epsilon - \epsilon_i) \quad (2.10)$$

and the total energy of the occupied levels is given by,

$$U = \int_{-\infty}^{\epsilon_F} \epsilon g(\epsilon) d\epsilon \quad (2.11)$$

Similarly, the total number of particles (proton or neutron) is given by,

$$N = \int_{-\infty}^{\epsilon_F} g(\epsilon) d\epsilon \quad (2.12)$$

A smoothed sum of the single particle energies is now obtained by replacing the  $\delta$  function by a smooth distribution:

$$\tilde{g}(\epsilon) = \sum_{i=1}^{\infty} f\left(\frac{\epsilon - \epsilon_i}{\gamma}\right) \quad (2.13)$$

The function is like a Gaussian and the parameter  $\gamma$  should be chosen suitably such that the smoothed level distribution shows fluctuations only near major shell structures.

With this smooth distribution of levels, the Fermi energy is fixed using

$$N = \int_{-\infty}^{\tilde{\epsilon}_F} \tilde{g}(\epsilon) d\epsilon \quad (2.14)$$

and the smoothed total energy can be determined from,

$$\tilde{U} = \int_{-\infty}^{\tilde{\epsilon}_F} \epsilon \tilde{g}(\epsilon) d\epsilon \quad (2.15)$$

Hence, the shell correction becomes,

$$E_{sh} = U - \tilde{U} \quad (2.16)$$

With this shell correction, one can easily calculate the total energy of the nuclear system as function of deformation parameter  $\beta$  or triaxiality parameter  $\gamma$ . Often, the higher order deformations, for example  $\beta_4$  are also considered and the total energy is minimized with respect to  $\beta_4$  for every pair of  $\beta_2$  and  $\gamma$ . The total energy as a function of  $\beta_2$  and  $\gamma$  can be plotted in contour plots (potential energy surface). The minimum in this contour defines the ground state deformation of the nucleus.

## 2.6 Rotating nuclei

In the previous section the models described were considering the nucleus at rest. A deformed nucleus can rotate and consequently, the rotational states with  $I(I+1)$  character are developed. Such rotational bands have been observed experimentally in deformed nuclei. The rotational states originate from the rotation of the nucleus about an axis perpendicular to its symmetry axis. A quantum mechanical system can not rotate around the symmetry axis. In a nucleus, however, an interaction occurs between single particle excitations and collective rotations which leads to a rotation around the symmetry axis (large K quantum number). Among the theoretical models proposed to describe the high spin states of a nucleus, the cranking model is one of the most successful ones.

### 2.6.1 Cranking Model

The basic principle of cranking model was suggested by D. R. Inglis [40, 41] in 1954. Which was used extensively during the last couple of decades [42, 43]. It combines the formalism of the two extreme limits, i.e., the description of high spin single particle

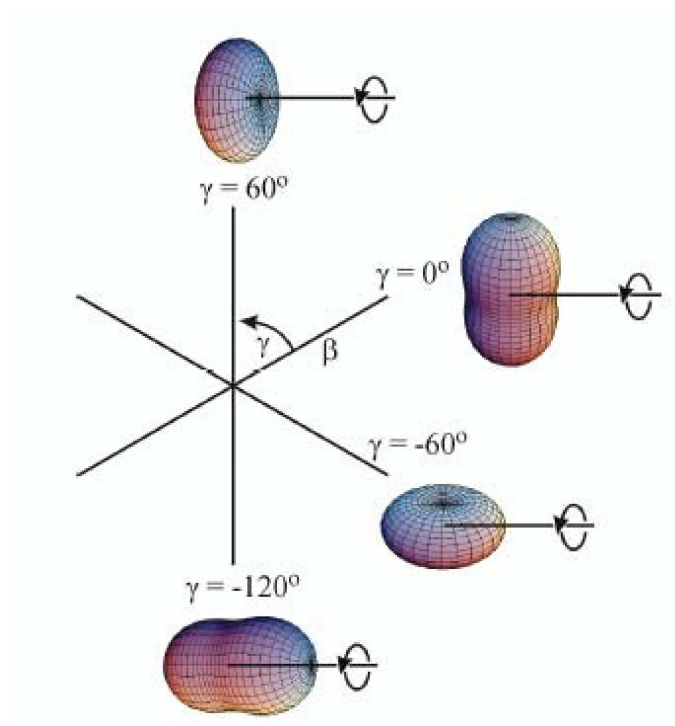


Figure 2.4: Deformation and nuclear rotation following the Lund convention.

configuration and the collective rotation.

In Cranking model, the rotation is treated in a classical sense with the rotation vector coinciding with one of the main axis of the nucleus. It then turns out that, in the system, the nucleus can be described as independent particles moving in a rotating potential (Woods-Saxon or modified oscillator) i.e. rotation degree of freedom enters in the very much the same way as deformation degree of freedom. For simplicity, the treatment in this model are done in the body fixed co-ordinate system. It was mentioned in the section 2.3, that the range of  $\gamma$  between  $0^\circ$  and  $60^\circ$  is sufficient to describe the intrinsic shape. However, in order to describe a cranked system, one needs three times larger range of  $\gamma$  variables, namely,  $-120^\circ \leq \gamma^\circ \leq 60^\circ$ , corresponding to the three axis about which the system with a given intrinsic shape is cranked. This is shown in Fig. 2.4, where the shapes of the nucleus is shown for different values of the parameter  $\gamma$  following the Lund convention.

Considering the symmetry axis as the  $z$ -axis and cranking the nuclei along  $x$ -axis, one gets Schrodinger equation in rotating system

$$(H_0 - \omega J_x)\phi^\omega = e^\omega \phi^\omega \quad (2.17)$$

Thus, one can get the Cranking Hamiltonian as

$$H_\omega = H_0 - \omega J_x \quad (2.18)$$

Where,  $H_0$ , is like Wood-Saxon or Nilsson potential and  $\omega J_x$  term expresses the coriolis and centrifugal force in the rotating co-ordinate system. In the non-rotating case, as discussed in the previous section,  $\Omega$  is a good quantum number, which indicates that the time reversal symmetry is a conserved in the non-rotating nuclei. The  $\omega J_x$  term in the cranking Hamiltonian destroys this time reversal symmetry and hence  $\Omega$  is no longer a conserved quantity. However, another important symmetry in the rotating nuclei still survive called *signature*,  $\alpha$ , which is related to the properties of a nucleonic state under a rotation of  $\pi$  around the cranking axis. It is defined as,

$$R_X(\pi)\psi_\alpha = e^{-i\pi J_x}\psi_\alpha = e^{-i\pi\alpha}\psi_\alpha \quad (2.19)$$

Where,  $\psi_\alpha$  denotes the wave function with signature  $\alpha$ . The signature of the single particle state, can be  $\alpha = +1/2$  or  $\alpha = -1/2$ . In a non-rotating potential the time conjugate states with spin-projection  $+\Omega$  and  $-\Omega$  the symmetry axis are energetically degenerate. Although they do not have a good signature with respect to rotation around x-axis, their linear combinations can give eigenstates of signature. Then, the solutions of the Hamiltonian Eq. 2.18 can be four sets of eigenstates. They are with  $(\pi, \alpha)$  given by,  $(+,+1/2)$ ,  $(+,-1/2)$ ,  $(-,+1/2)$  and  $(-,-1/2)$ .

The parity  $\pi$  is also a good quantum number of the cranking Hamiltonian, since this does not mixes the states with different parity. So in the cranking model the conserved quantities are the signature  $\alpha$  and the parity  $\pi$ .

The eigenvalues of the cranking Hamiltonian can be written as a function of rotational frequency  $\omega$  by,

$$e'_\mu = \langle \mu | H_\omega | \mu \rangle = \langle \mu | H_0 | \mu \rangle - \omega \langle \mu | J_x | \mu \rangle \quad (2.20)$$

Which implies that,

$$\frac{de'_\mu}{d\omega} = -\langle\mu|J_x|\mu\rangle \quad (2.21)$$

$e'_\mu$  are called the single particle Routhian and the slope of this single particle Routhian is equal to the expectation value of the angular momentum operator  $j_x$  with reversed sign. The total angular momentum along the axis of rotation can be calculated for N particle system as,

$$I_1 = \sum_{\mu=1}^N \langle\mu|J_x|\mu\rangle \quad (2.22)$$

where  $\mu$  runs over all the occupied levels. The total Routhian is given by,

$$E' = \sum_{\mu=1}^N \langle\mu|H_\omega|\mu\rangle = \sum_{\mu=1}^N e'_\mu \quad (2.23)$$

## 2.7 Total Routhian Surfaces calculations

The total Routhian surface calculations are used to obtain the shape parameter of nucleus corresponding to minimum energy of the nucleus. In the calculations, the total energy of nucleus in terms of  $N$ ,  $Z$ ,  $\beta_2$ ,  $\gamma$ ,  $\omega$  is given by,

$$E^\omega(Z, N, \beta_2, \gamma) = E^{\omega=0}(Z, N, \beta_2, \gamma) + (\langle\chi^\omega|H^\omega(Z, N, \beta_2, \gamma)|\chi^\omega\rangle - \langle\chi^\omega|H^{\omega=0}(Z, N, \beta_2, \gamma)|\chi^\omega\rangle) \quad (2.24)$$

The first term gives the energy of the nucleus in ground state and the second term gives the rotational contribution to the energy.

The static energy is given by,

$$E^{\omega=0}(Z, N, \beta_2, \gamma) = E_{LDM}(Z, N, \beta_2, \gamma) + \delta E_{shell}(Z, N, \beta_2, \gamma) \quad (2.25)$$

where, the first term is the Liquid Drop energy and the second term is due to shell correction as mentioned before. Now, the rotational part of the energy can be calculated from Eq. 2.24. The nuclear average potential taken in the Cranking Hamiltonian is Wood-Saxon type. The calculations have been performed in the following scheme. At each pair of deformation parameters  $(\beta_2, \gamma)$ , the total energy is found out. It is

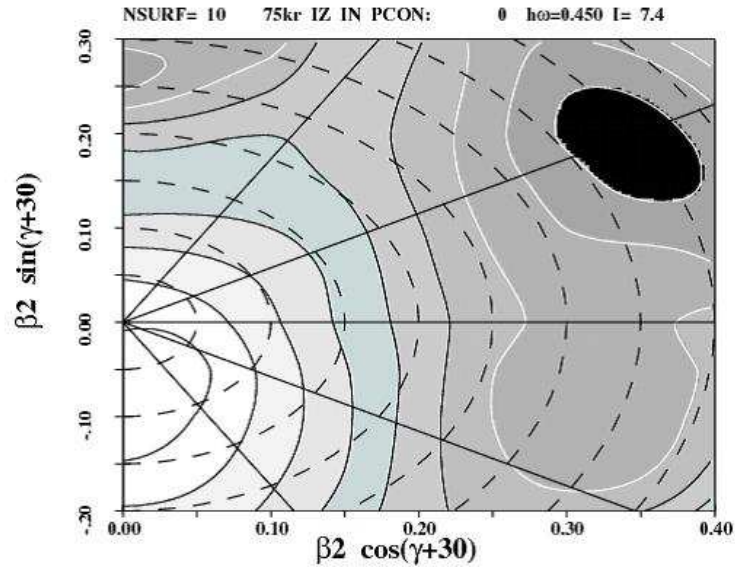


Figure 2.5: Total Routhian Surface calculation for the positive parity yrast band of  $^{75}\text{Kr}$  at  $\hbar\omega = 0.45$  MeV.

minimized with respect to higher order shape parameters like  $\beta_4$ . To make the energy contour plot, the following transformation has been made,

$$\begin{aligned} X &= \beta_2 \cos(\gamma + 30) \\ Y &= \beta_2 \sin(\gamma + 30) \end{aligned} \quad (2.26)$$

Figure 2.5 shows the TRS plot for positive-parity of  $^{75}\text{Kr}$ . A stable minimum at rotational frequency  $\hbar\omega = 0.45$  MeV is seen in energy surface at  $\beta_2 \approx 0.39$ ,  $\gamma \approx -5^\circ$ . This indicates the nearly prolate nuclear shape at this rotational frequency. This model is quite successful in explaining the alignments and can also be used to compare with the measured electromagnetic transition strengths and moments.

## 2.8 Projected Shell-Model

Elliott was the first to point out the advantage of a deformed (intrinsic) many-body basis and developed the SU(3) shell model for sd-shell nuclei [44]. In this model the classification of the basis states and their projection onto the good angular momentum states is done on the basis of group theoretical techniques. It works nicely for light systems where the LS-coupling is very weak. In heavier nuclei, where the presence of strong LS-coupling is essential for reproducing the correct shell closure, SU(3) scheme

is no longer valid. The natural extension of the SU(3) shell model for heavier deformed systems is the Projected Shell model, where Nilsson model along with BCS scheme (to take care of strong pairing interaction) is used for basis selection and the projection of these deformed basis onto good angular momentum states is done numerically. The deformed basis provides us an efficient way to truncate the shell model basis. The most important aspect of the model is that it allows us to interpret the results in simple way.

### 2.8.1 Projection operator

The explicit form of the group element is given by

$$\hat{R}(\Omega) = \exp(-i\alpha\hat{J}_x) \exp(-i\beta\hat{J}_y) \exp(-i\gamma\hat{J}_z) \quad (2.27)$$

where, the  $\Omega$  represents a set of Euler angles ( $\alpha, \gamma = [0, 2\pi], \beta = [0, \pi]$ ) and the  $\hat{J}'_s$  are the angular momentum operators. The unitary representation of the rotation operator is given by

$$\langle \mu IM | \hat{R}(\Omega) | \nu JK \rangle = \delta_{\mu\nu} \delta_{IJ} D_{MK}^{I*}(\Omega) \quad (2.28)$$

where, the superscript  $*$  is for the complex conjugate and  $D_{MK}^I(\Omega)$  is the  $D$ -function [45]. For a state  $|\mu IM\rangle$  belonging to the angular momentum  $IM$ ,  $\mu$  designates a set of quantum numbers that specify the quantum state uniquely. It obeys the following closure relation:

$$\sum_{\mu IM} |\mu IM\rangle \langle \mu IM| = 1 \quad (2.29)$$

From the above two equations, it follows that

$$\hat{R}(\Omega) | \nu JK \rangle = \sum_M | \nu IM \rangle D_{MK}^{I*}(\Omega) \quad (2.30)$$

Using this equation and the orthogonality of  $D$ -functions

$$\int d\Omega D_{MK}^{I*}(\Omega) D_{M'K'}^I(\Omega) = \frac{8\pi^2}{2I+1} \delta_{II'} \delta_{MM'} \delta_{KK'} \quad (2.31)$$

We obtain the relation

$$\hat{P}_{MK}^I |\nu I' K'\rangle = \delta_{II'} \delta_{KK'} |\nu IM\rangle \quad (2.32)$$

where the operator  $\hat{P}_{MK}^I$  is defined by

$$\hat{P}_{MK}^I = \frac{2I+1}{8\pi^2} \int d\Omega D_{MK}^I(\Omega) \hat{R}(\Omega) \quad (2.33)$$

and is called the angular momentum projection operator.

Below are given some of the important properties of the Projection operator

$$\hat{P}_{MK}^I = \sum_{\nu} |\nu IM\rangle \langle \nu IK\rangle$$

$$\sum_{IM} \hat{P}_{MM}^I = 1$$

$$\hat{P}_{MK}^{I\dagger} = \hat{P}_{KM}^I$$

$$\hat{P}_{MK}^I \hat{P}_{M'K'}^I = \delta_{II'} \delta_{MM'} \hat{P}_{KK'}^I$$

Using these ideas about the Projection operator, let us consider the shell model with the projected basis, as will be discussed in the following section.

## 2.8.2 Shell model in projected basis

Suppose that  $|\phi\rangle$  is a deformed state and therefore, not an eigenstate of the angular momentum. Because of the rotational invariance of the Hamiltonian, i.e.,

$$\hat{R}^\dagger(\Omega) \hat{H} \hat{R}(\Omega) = \hat{H} \quad (2.34)$$

the energy expectation value remains the same even if we rotate the state  $|\phi\rangle$ . Considering a wider class of states by forming a superposition

$$|\psi\rangle = \int d\Omega F(\Omega) \hat{R}(\Omega) |\phi\rangle, \quad (2.35)$$

where  $F(\Omega)$  is a function to be determined by minimizing the energy expectation value

$$E = \frac{\langle \psi | \hat{H} | \psi \rangle}{\langle \psi | \psi \rangle} \quad (2.36)$$

Because of larger space spanned by projected state  $\hat{R}(\Omega)|\phi\rangle$  it gives lower energy compared to that of the single deformed state  $|\phi\rangle$  corresponding to  $\Omega = 0$ .

Using the completeness of the D-functions, one can write the trial function  $F(\Omega)$  as

$$F(\Omega) = \sum_{IMK} \frac{2I+1}{8\pi^2} F_{MK}^I D_{MK}^I(\Omega) \quad (2.37)$$

and now using this into Eq. 2.35 one gets

$$|\psi\rangle = \sum_{IMK} F_{MK}^I \hat{P}_{MK}^I |\phi\rangle \quad (2.38)$$

The coefficients  $F_{MK}^I$  play the role of the variational parameters. Carrying out the variation with  $|\psi\rangle$  given in the above Eq. 2.38, the summation over  $I$  and  $M$  drops away because of the orthogonality relations of projection operator and the rotational invariance of the Hamiltonian. Thus it is sufficient to carry out the variation calculations with

$$|\psi\rangle = \sum_K F_K^I \hat{P}_{MK}^I |\phi\rangle \quad (2.39)$$

The resulting variational equation takes the form of an eigenvalue equation independent of  $M$ :

$$\sum_{K'} \{H_{K'K}^I - EN_{KK'}^I\} F_{K'}^I = 0 \quad (2.40)$$

$$N_{KK'}^I = \langle \phi | \hat{P}_{KK'}^I | \phi \rangle$$

where, the Hamiltonian and norm are defined as,

$$H_{K'K}^I = \langle \phi | \hat{H} \hat{P}_{KK'}^I | \phi \rangle \quad (2.41)$$

$$N_{KK'}^I = \langle \phi | \hat{P}_{KK'}^I | \phi \rangle$$

For an axially symmetric nuclei, where  $\hat{J}_z |\phi\rangle = K_0 |\phi\rangle$  holds,  $K_0$  being the conserved  $K$ -quantum number, the problem is simple. The solution of the above equation becomes,

$$E = \frac{H_{K_0 K_0}^I}{N_{K_0 K_0}^I} \quad (2.42)$$

$$F_{K_0}^I = \sqrt{\frac{1}{N_{K_0 K_0}^I}}$$

The state  $|\phi\rangle$  used in the above discussion can be generated in various ways. One can construct the symmetry violating state using the Nilsson (or Hartree-Fock) single-particle basis or, if the pairing is strong, the Nilsson + BCS (or Hartree-Fock-Bogolyubov) quasi-particle basis. The state  $|\phi\rangle$  may violate various symmetries of the Hamiltonian because it represents the intrinsic state. Violated symmetry is recovered in the state  $|\psi\rangle$ . This state  $|\psi\rangle$  can be accepted as a approximate solution of the Hamiltonian. One can refer to  $|\psi\rangle(|\phi\rangle)$  as a state in the space-fixed (body-fixed) system. This terminology can be traced back to the mathematical nature of the  $D$ -function used in the projection operator. As there exist two sets of angular momentum operators, one for body-fixed frame and the other for space-fixed frame. The quantum numbers  $M$  and  $K$  of  $D_{MK}^I(\Omega)$  originates from space-fixed and body-fixed co-ordinates, respectively. Thus the quantum number  $M$  belongs to  $|\psi\rangle$  and  $K$  to  $|\phi\rangle$ . Hence, the projection operator transforms a body-fixed state  $|\phi\rangle$  to space-fixed frame  $|\psi\rangle$ .

Upto now, only one projected basis is used for eigen value problem, to get the flavor of the Projection technique. In reality, lot of configurations  $|\phi\rangle$  coexist within excitation of few MeV, and they can interact. Thus the observed spectrum of the nuclei should be compared with the calculations of PSM only after the mixing of different projected states at each spin. Let us select a set of multi-quasiparticle states  $|\phi\rangle$  which we want to take into account in the shell model configuration space by projecting them onto good angular momentum  $I$ .

Once the quasi particle basis is prepared, we diagonalize the Hamiltonian in the shell model space spanned by  $\hat{P}_{KK'}^I|\phi\rangle$ . This leads to he eigenvalue equation

$$\sum_{\kappa'K'} \{H_{\kappa K \kappa' K'}^I - EN_{\kappa K \kappa' K'}^I\} F_{\kappa' K'}^I = 0 \quad (2.43)$$

with the normalization condition

$$\sum_{\kappa K \kappa' K'} F_{\kappa K}^I N_{\kappa K \kappa' K'}^I F_{\kappa' K'}^I = 1 \quad (2.44)$$

### 2.8.3 Choice of Hamiltonian

In the PSM calculation, we employ a quadrupole plus pairing Hamiltonian, with inclusion of quadrupole-pairing term [46]

$$\hat{H} = \hat{H}_0 - \frac{1}{2}\chi \sum_{\mu} \hat{Q}_{\mu}^{\dagger} \hat{Q}_{\mu} - G_M \hat{P}^{\dagger} \hat{P} - G_Q \sum_{\mu} \hat{P}_{\mu}^{\dagger} \hat{P}_{\mu}. \quad (2.45)$$

In the above equation,  $\hat{H}_0$  is the spherical single-particle Hamiltonian which contains a proper spin-orbit force

$$\hat{H}_0 = \sum_{\alpha} c_{\alpha}^{\dagger} \varepsilon_{\alpha} c_{\alpha} \quad (2.46)$$

where,  $\varepsilon_{\alpha} (\equiv \hbar\omega\{N - \kappa[2\mathbf{j}\cdot\mathbf{s} + \mu(\mathbf{I}^2 - \langle \mathbf{I}^2 \rangle)_{N\mathbf{j}}]\})$  is the energy of the single particle levels of the spherical harmonic oscillator with quantum numbers  $\alpha = N, j, m$ . For f-p-g nuclei, we have taken three major shells for active nucleons i.e.,  $N = 2, 3$  and 4 for both neutron and proton.

The one-body operators in the Hamiltonian are defined by

$$\begin{aligned} \hat{Q}_{\mu} &= \sum_{\alpha\beta} c_{\alpha}^{\dagger} Q_{\mu\alpha\beta} c_{\beta} \\ \hat{P}^{\dagger} &= \frac{1}{2} \sum_{\alpha} c_{\alpha}^{\dagger} c_{\bar{\alpha}}^{\dagger} \\ \hat{P}_{\mu}^{\dagger} &= \frac{1}{2} \sum_{\alpha\beta} c_{\alpha}^{\dagger} Q_{\mu\alpha\beta} c_{\bar{\beta}}^{\dagger} \end{aligned} \quad (2.47)$$

where  $\bar{\alpha}$  represents the time reversed state of  $\alpha$  and

$$Q_{\mu\alpha\alpha'} = \delta_{NN'} (Njm | Q_{\mu} | N'j'm') \quad (2.48)$$

is the matrix element of quadrupole operator. The strength of the quadrupole force  $\chi$  is adjusted such that the known quadrupole deformation parameter  $\epsilon_2$  is obtained. This condition results from the mean-field approximation of the quadrupole-quadrupole interaction of the Hamiltonian in Eq. 2.28. Paring force are assumed to act only between like nucleons. The coupling constant for the monopole pairing force is taken as

$$\begin{aligned} G_M^{\nu} &= [20.25 - 16.20 \frac{N-Z}{A}] A^{-1} \\ G_m^{\pi} &= 20.25 A^{-1} \end{aligned} \quad (2.49)$$

The strength parameter  $G_Q$  for quadrupole pairing is assumed to be proportional to  $G_M$ . It has been shown that the band crossing spins vary with the magnitude of

the quadrupole pairing force [47]. The ratio  $\frac{G_Q}{G_M}$  has therefore been slightly adjusted around 0.20 to reproduce the observed band crossings.

### 2.8.4 Electromagnetic transition strengths

Electromagnetic transitions can give important information on the nuclear structure and provide a stringent test of a particular model. In the present work, we have calculated the electromagnetic properties using the PSM approach to compare the experimental data. The reduced transition probabilities  $B(EL)$  from the initial state  $(\sigma_i, I_i)$  to the final state  $(\sigma_f, I_f)$  are given by [46]

$$B(EL, I_i \rightarrow I_f) = \frac{e^2}{(2I_i + 1)} |\langle \sigma_f, I_f || \hat{Q}_L || \sigma_i, I_i \rangle|^2, \quad (2.50)$$

However, the transition quadrupole moment  $Q_t(I)$  is related to the  $B(E2)$  transition probability through

$$Q_t(I) = \left( \frac{16\pi}{5} \frac{B(E2, I \rightarrow I - 2)}{\langle IK20 | I - 2K \rangle} \right)^{1/2} \quad (2.51)$$

In our calculations, we have used the effective charges of 1.5e for protons and 0.5e for neutrons, which are the same as in the previous PSM calculations [48, 46]. Variation of  $Q_t$  with spin  $I$  provide information on shape evolution in nuclei. In the case of a rigid rotor, the  $Q_t$  curve as a function of  $I$  is a straight line. Experimentally, one finds a deviation from the rigid body behavior for most of the nuclei in  $A = 70$  mass region. One expects more or less a constant value in  $Q_t$  up to the first band crossing. At the band crossing, one often sees a dip in  $Q_t$  value due to a small overlap between the wave functions of the initial and the final states involved. There can be a change in  $Q_t$  values after the first band crossing, which indicates a shape change induced by quasi-particle alignment

## 2.9 Conclusion

In this chapter, the striking features of various nuclear models have been outlined which are relevant to the present work. Basic postulates of shell model and cranking models

are described, prediction of which have been used for direct or indirect comparison of observed data. The shape of the nucleus as a function of rotational frequency calculated through TRS is considered. The calculated quantities like level energy as a function of angular momentum or rotational frequency in a model can be compared with the experimental observed values. The importance of the PSM has been emphasized because it gives the wave function in the laboratory frame and can be directly compared with the experimental transition strengths by measuring lifetimes of nuclear states

# Chapter 3

## Experimental Techniques

The production of nuclei away from the  $\beta$ -stability line with high yield is an experimental as well as technological challenge for the modern science. The study of nuclear structure at high spin states has undergone spectacular progress in the last decade due to the possibilities of accelerating heavy ions and the development of state of art sophisticated detector arrays. Recently, using high resolution and highly efficient detectors a lot of experimental studies have gained by the observations of excited states with very high angular momentum ( $I \geq 40\hbar$ ) as discrete lines in the  $\gamma$  ray spectra. The large amounts of energy and angular momentum transferred in these reactions are not only converted to external excitations (i.e. rotation of the nucleus as a whole) but also to internal degrees of freedom. The excitation of collective and single particle degrees of freedom offers us the possibility of studying the interplay between the classical and quantal phenomena. In this chapter, we shall discuss briefly, the description of the method of producing high spin states of proton rich nuclei away from the  $\beta$  stability line. Following that, the techniques and detector systems used to detect the discrete  $\gamma$  rays from the reaction is discussed. Finally, the Indian National Gamma Array is discussed in details in last section.

### 3.1 Production of proton rich nuclei

In the study of high spin states one searches for reaction which can transfer highest possible angular momentum  $l$  with the largest possible cross-section  $\sigma$ . The heavy

ion fusion evaporation reactions form the most efficient way to achieve this. In a complete fusion reaction the incident particle is captured by the target nucleus to form a compound nucleus (see Fig. 3.1). The kinetic energy in the centre of mass (cm) system is converted into excitation energy of the compound nucleus, being shared among the constituent nucleons. The lifetime of the composite system (compound nucleus) is long enough ( $10^{-20}$  s) for thermodynamic equilibrium to be reached before it decays. During this time all memory of its formation process is lost, with the exception of conservation of energy, angular momentum. The transferred angular momentum in the reaction is determined by the momentum of the particle  $m_p v_p$  relative to the target nucleus and by the impact parameter  $b$ , according to the relation  $l = m_p v_p b$ . This simple relation shows that high-energetic heavy ions are the most suitable to excite high-spin states.

If  $l_{max}$  is the maximum angular momentum corresponding to a peripheral collision, and if we use a sharp cut-off approximation and assume that no reaction will occur at  $l > l_{max}$ ; i.e. the transmission coefficient  $T_l = 0$  for partial waves with  $l > l_{max}$  and  $T_l = 1$  for  $l \leq l_{max}$ . The total reaction cross-section  $\sigma_R$  can be written as a sum of the contribution from all partial waves up to  $l_{max}$  as:

$$\sigma_R = \pi\lambda^2(2l + 1)T_l \approx \pi\lambda^2(l_{max} + 1)^2 \quad (3.1)$$

where the reduced wavelength for the entrance channel is

$$\lambda = \hbar/\sqrt{(2E_{cm}\mu)} \quad (3.2)$$

Here  $E_{cm}$  denotes the centre-of-mass energy and  $\mu = A_1 A_2 / (A_1 + A_2)$ , the reduced mass of the colliding nuclei with mass numbers  $A_1$  and  $A_2$ . From the requirement of energy conservation from infinity to the distance of closest approach between the colliding nuclei we obtain the relationship:

$$l_{max}^2 = (2\mu R^2/\hbar^2)(E_{cm} - V_c) \quad (3.3)$$

where  $R = 1.4 (A_1^{1/3} + A_2^{1/3})$  is the maximum distance at which the collision leads to any reaction. The Coulomb energy in Eq. 3.3 is given by

$$V_c = 1.441Z_1Z_2/R \quad (3.4)$$

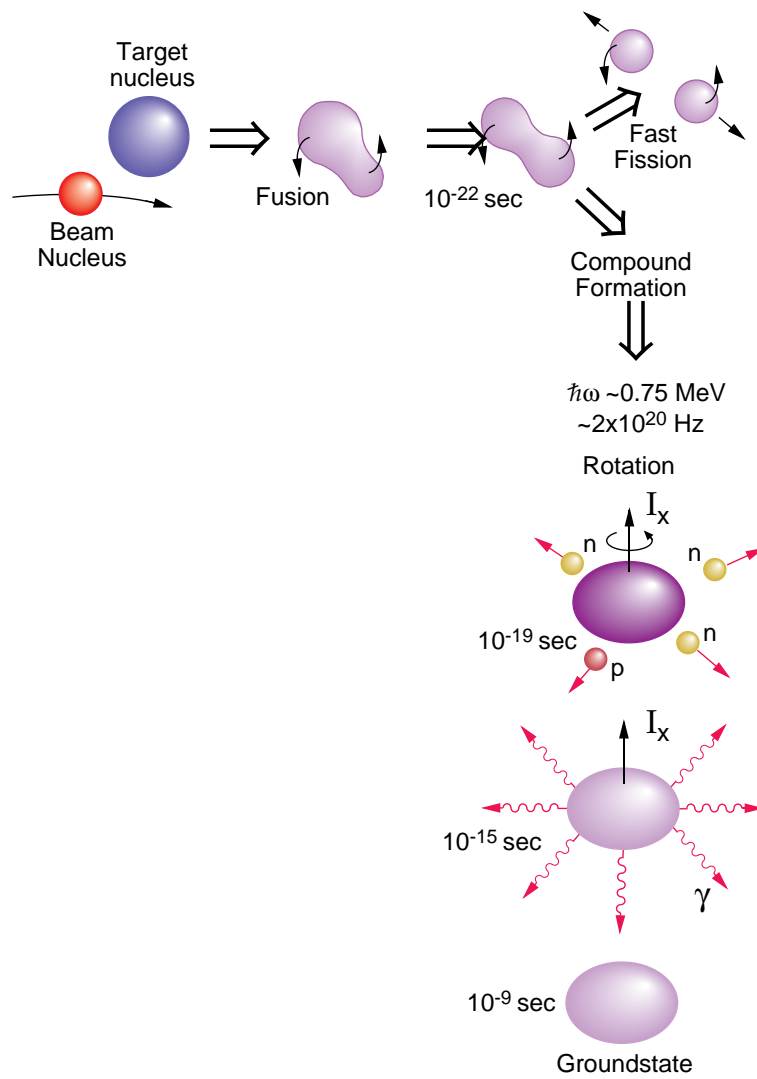


Figure 3.1: Figure shows the fusion evaporation reaction

in units of  $MeV$  when  $R$  is in  $fm$  and  $Z_1$  and  $Z_2$  are the atomic numbers. The excitation energy of the compound nucleus is given by

$$E_{ex} = E_{cm} + Q_{fus} \quad (3.5)$$

The time needed for the projectile to pass through the target nucleus is  $\approx 10^{-22}$  s and a fast rotating dinuclear can be formed that may lead to the formation of a compound nucleus if it does not undergo for fast fission. The rapid rotation with an angular velocity  $\omega \approx 0.75MeV/\hbar$  corresponds to  $2 \times 10^{20}$  revolution/s of the compound nucleus. The decay mainly proceeds via neutron emission as due to their lack of charge they do not feel the effect of the Coulomb barrier, although high energy  $\gamma$ -ray emission is not excluded, due to enhancement of giant dipole resonance, GDR, built on excited states. An emitted neutron lowers considerably the excitation energy, at least by its separation energy of  $8-10MeV$  and angular momentum of about  $1\hbar$ . In general not only neutrons but also charged particles can be emitted from the highly excited nucleus. The number of emitted nucleons is very sensitive to the excitation energy of the compound nucleus, for a particular excitation energy several evaporation channels are possible leading to the formation of a number of nuclei with similar  $Z$  and  $A$ . After  $10^{-15}$ s the excitation energy is lowered by neutron emission to a region of one neutron separation energy or less above the *yrast line*. The *yrast line* is a sequence of all states that have the highest angular momentum for a given energy. The decay of these states now proceeds via  $\gamma$ -ray emission, reaching the ground state after  $\approx 10^{-9}$ s

The  $\gamma$ -ray spectroscopy probes the region on and just above the *yrast line* in the  $E_x$  versus  $l$  plane which are populated in the last  $10^{-9}$ s of the de-excitation process of the compound nucleus. For heavy nuclei ( $A > 130$ ), the large Coulomb barriers inhibit charged particle emission and the dominant reaction channels are the neutron channels, i.e.  $(HI, xn)$  type with  $x \sim 4-6$ . For medium mass nuclei ( $A < 100$ ), the reduced barrier allows protons and alphas to be emitted in addition to neutrons. The increased neutron separation energies for neutron deficient nuclei further enhance the charged particle emission. In this work the most dominant reaction channels are  $2pn$  and  $3p$ .

The ion-beams required for populating the nuclei of interest, by fusion evaporation reaction were obtained from 15 UD Pelletron accelerator facility at IUAC, New Delhi. This facility is briefly discussed in the following:

## 3.2 Accelerator Facility

The ion beams were obtained from the 15UD tandem accelerator facility at IUAC [49], New Delhi. The source for the charged particles is located at the top of the accelerator tower. A Caesium sputter ion source generates negative ions, which are initially accelerated to low energies (150-250 keV) in a short horizontal section. These low energy negative ions are then bent through 90° using an injector magnet into the vertical accelerating column. In the first stage, the acceleration results from the electrostatic attraction of the negative ions by the positively charged high voltage terminal situated at the centre of the column. The high electric potential at the terminal is achieved by a continuous transfer of charge to the terminal by means of the chain of steel pellets and hence the name pelletron accelerator. Inside the terminal the ions pass through a thin carbon foil or a small volume of gas, where they lose electrons and acquire a high positive charge. The average charge of the ion depends on the type of the ion and the terminal voltage. The resulting positive ions enter the second or high energy stage of acceleration where the positive voltage of the terminal acts repulsively on the positive ions. In this way, the final energy of the ion that has acquired a positive charge of "q" units will be (q+1)V, where V is the terminal voltage (maximum of 14MV). As the negative ion pass through the carbon foil, we actually get a distribution of charge state at the end of the terminal. Hence, at the end of the accelerating column, we get positive ions of different energy. To select the correct energy for a given beam the magnetic field of the analyzing magnet is set to

$$B = \frac{\kappa\sqrt{AE}}{q} \left(1 + \frac{E}{3725.9A}\right) \quad (3.6)$$

where B is in Gauss,  $\kappa$  is the calibration constant determined experimentally. In this case,  $\kappa = 720.76 \pm 0.06$  Gauss  $(a.m.u.MeV)^{-1/2}$ . A is in *a.m.u.*, E is in *MeV* and

$q$  is the charge state of the ion.

### 3.3 Detector systems

In order to detect and identify the gamma decay following the fusion evaporation reaction we need to use gamma detectors. In this section, the method and techniques to detect gamma rays are being discussed. The array of detectors and its associated electronics used in the present work will also be described in detail in this section.

#### 3.3.1 Interaction of gamma rays with matter

The total attenuation coefficient for a  $\gamma$  or X-ray traveling through a medium has contributions from scattering, photoelectric absorption and pair production processes. The three main processes are discussed below.

##### Compton scattering

In this case, an incident  $\gamma$  ray scatters from an outer shell electron in the absorber material at an angle  $\theta$ , and some of the  $\gamma$ -ray energy is imparted to the electron. Conservation of energy and momentum lead to the following expression for the energy of the scattered photon:

$$E'_\gamma = \frac{E_\gamma}{1 + (E_\gamma/m_0c^2)(1 - \cos \theta)} \quad (3.7)$$

where  $E_\gamma$  is the incident photon energy,  $E'_\gamma$  is the energy of the scattered photon,  $\theta$  is the scattering angle and  $m_0c^2$  is the electron rest mass energy. The kinetic energy of the electron after the collision is given by

$$T_e = E_\gamma - E'_\gamma = \frac{E_\gamma^2}{m_0c^2 + E_\gamma(1 - \cos \theta)}. \quad (3.8)$$

It can be seen that, since all scattering angles are possible, the electron energy ranges from zero for  $\theta = 0^\circ$  to  $2E_\gamma^2/(m_0c^2 + 2E_\gamma)$  for  $\theta = 180^\circ$ , and that the photon

never loses the whole of its energy in any one collision. The scattered photon can then continue through the absorber and interact again or scatter out of the absorber material completely. This process, where the scattered photon escapes, is very important for the  $\gamma$ -ray spectroscopist. If the full energy of the incident photon is not absorbed in the detector, then there is a continuous background in the energy spectrum, known as the Compton continuum. This continuum extends up to an energy corresponding to the maximum energy transfer, where there is a sharp cut-off point, known as the Compton edge. Compton scattering is the most probable process for photons in the intermediate energy range and the probability decreases rapidly with increasing energy. The probability is also dependent on the number of electrons available for the photon to scatter from, and hence increases with increasing  $Z$ .

### Photoelectric absorption

An incident photon is completely absorbed by an atom in the absorber material, and one of the atomic electrons is ejected. This ejected electron is known as a photoelectron. The electron must be bound to the atom, to conserve energy and momentum. The kinetic energy of the photoelectron is given by

$$T_e = E_\gamma - B_e \quad (3.9)$$

where  $B_e$  is the binding energy of the atomic electron. The vacancy left in the atomic structure by the ejected electron is filled by one of the electrons from a higher shell. This transition is accompanied by an emission of an X-ray. These X-rays are also absorbed by the detector. Photoelectric absorption is the most favorable process for the  $\gamma$ -ray spectroscopist, since the incident photon deposits all of its energy into the detector, but it is only dominant for low energy photons ( $< 200$  keV). The interaction is again dependent upon  $Z$ , and an approximate expression for the absorption probability  $\tau$  is

$$\tau \propto \frac{Z^n}{E_\gamma^{3.5}}. \quad (3.10)$$

Here  $n$  is normally between 4 and 5 depending on the absorber material. This dependence on  $Z$  explains the choice of high- $Z$  materials such as lead for shielding purposes.

### Pair production

The third important  $\gamma$ -ray interaction is the process of pair production. If the incident photon energy is greater than 1.022 MeV (twice the electron rest mass) in the presence of an atomic nucleus an electron/positron pair can be produced. Any residual energy is distributed evenly between the electron and positron as kinetic energy. As the positron slows to thermal energies through interaction with the detector material, it can annihilate with one of the atomic electrons producing two  $\gamma$  rays of energy 511 keV. These  $\gamma$  rays can then either be absorbed or escape the detector. This is evidenced by the so-called escape peaks observed in  $\gamma$ -ray spectra. If one of the 511 keV photons escapes the detector, then a peak is observed at  $E_\gamma - m_0c^2$  (single escape peak). If both escape, then a peak is observed at  $E_\gamma - 2m_0c^2$  (double escape peak). The process of pair production only becomes important for high energy  $\gamma$  rays (5 - 10 MeV) which are outside the energy range of interest in the present work.

### 3.3.2 Germanium detectors

Discrete  $\gamma$ -ray spectroscopy requires a detection system that offers excellent energy resolution. Today, practically all  $\gamma$ -ray spectroscopy experiments employ high-resolution germanium detectors. The germanium detector, similar to other semiconductor detectors, is a large reverse-biased p-n junction diode. At the junction between the p-type and n-type material, the migration of electrons from the n-type material and holes from the p-type material gives rise to a region of net zero charge. This region is known as the depletion region. The net positive charge on one side of the junction, and the net negative charge on the other side, sets up an electric field gradient across the depletion region. Any  $\gamma$  rays interacting with the germanium, through the processes described in the previous section, will produce electron-hole pairs in the depletion region, which

will then be swept to the edges of the detector because of the electric field gradient, constituting an electric current. Since the depletion region is the active part of the Ge detector, the active volume is required to be as large as possible. If a reverse-bias is applied, the width of the depletion region can be increased. The width is proportional to  $(\frac{V}{N})^{\frac{1}{2}}$ . Here,  $V$  is the bias voltage applied and  $N$  is the impurity concentration of the germanium. Natural purity germanium can only maintain a depletion region of a few millimeters before electrical breakdown occurs. Therefore at a given bias voltage the only way to increase the width of the depletion region is to reduce the impurity concentration,  $N$ . Advances in manufacturing techniques have allowed extremely pure Ge crystals to be grown. This high-purity germanium, or HPGe, has impurity concentrations of around one part in  $10^{12}$ , allowing depletion depths of several centimeters to be achieved. The energy required to create an electron-hole pair in Ge is approximately 3 eV, thus an incident  $\gamma$  ray, with an energy of several hundred keV, produces a large number of such pairs, leading to good resolution and low statistical fluctuations. These are desirable properties as discussed earlier. HPGe detectors are operated at temperatures of around 77 K, in order to reduce noise from electrons which may be thermally excited across the small band gap in Ge (0.67 eV) at room temperature. This is achieved through thermal contact of the Ge crystal with a dewar of liquid nitrogen, using a copper rod, known as a cold finger.

### 3.3.3 Compton suppression

As discussed in section 3.3.1, Compton scattering means that  $\gamma$ -rays which enter the Ge detector will not deposit their full energy, leading to a large Compton continuum. In order to reduce the contribution of scattered  $\gamma$  rays the Ge detector can be surrounded by an inorganic scintillator detector. The two detectors are operated in anti-coincidence, which means that if an event occurs at the same time in both detectors, then the event is rejected. The majority of escape suppression shields, as they are known, use bismuth germinate ( $\text{Bi}_4\text{Ge}_3\text{O}_{12}$  =BGO). The reason for this choice is that BGO has excellent timing properties, which is desirable for coincidence work, and high density ( $7.3 \text{ g/cm}^3$ ), so that a relatively small amount of material is needed in order to stop

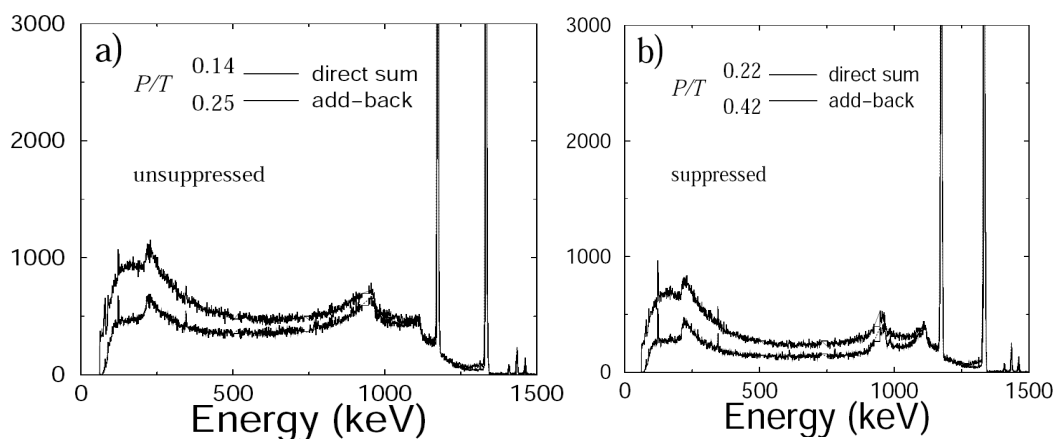


Figure 3.2: Figure showing the suppression of Compton continuum for  $^{60}\text{Co}$  source and the improvement in the peak to total ratio.

fully the scattered photons. This fact becomes important when we wish to closely pack many detectors around a target to form an array (see next section). An example of the effect of Compton suppression is shown in figure 3.2.

### 3.3.4 Clover detectors

The photopeak efficiency of detector can be increased by increasing the size of the Ge crystal but crystal size larger than 6 cm in diameter is difficult to fabricate. In addition, they have poor charge collection time and greater sensitivity to neutron damage. For in-beam spectroscopy, one would suffer from Doppler broadening of  $\gamma$ - rays emitted in flight. Therefore the detector volume is increased by accommodating more than one Ge crystal in the same cryostat which yield a segmentation of the solid angle. This result in design of the total array surrounded by anti-Compton shield. The schematic diagram of a clover detector is shown in Fig. 3.3. Each clover detector consists of four separate n type high purity Ge crystals placed in the form of a four-leaf clover in a single vacuum housing [50, 51].

The geometry of the HpGe crystals inside the vacuum chamber is shown in Fig. 3.3. Each of these crystals, 50 mm diameter and 70 mm long, has a tapering at the front face, leaving 89 % of the initial volume. A common high voltage supply provides to the inner side of the crystal with p-type contact in all the four crystals. Each crystal

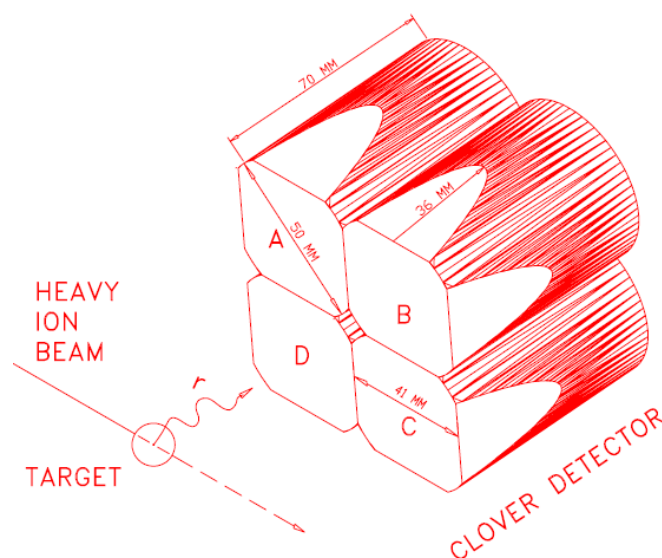


Figure 3.3: Schematic diagram of the clover detector

is coupled to a pre-amplifier. The timing and energy signals of each pre-amplifier is processed further.

### 3.3.5 Clover in addback Mode

To get the maximum efficiency from the clover detector, it should be used in add-back mode. A photon hitting a crystal can be absorbed or Compton scattered out of the detector or to one of the neighboring crystals. In the latter process, the scattered photon may be absorbed in the second crystal or it also can get scattered out of the detector or to the other crystal. Thus, a full energy signal can be generated by adding the energy signals from all the crystals obtained at the same time. This increases the photopeak efficiency compared to the direct summing of all four crystals where individual spectra from each crystal is added to obtain the total photopeak efficiency. This effect can be seen in Fig. 3.4 where the relative add-back efficiency is plotted as a function of energy. One has to take extreme care while using Clover detectors in add-back mode in gain matching of individual crystals.

- The gain matching of the individual crystals should be properly with extreme

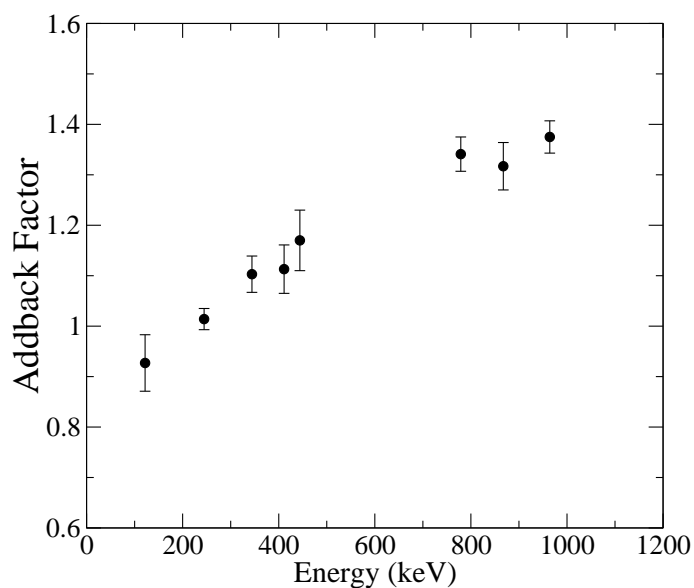


Figure 3.4: Figure showing the gain in efficiency due to addback

care for doing add-back in software.

- As the total surface area of the detector is large, there is a probability of two genuine gamma-rays originating from a cascade and hitting two crystals at the same time. This will then lead to a pseudo-peak called the sum peak. In this data the sum peak intensity was estimated to be less than 1% intense compared to the individual gamma ray hitting one of the crystal.

### 3.4 Array of Ge detectors

Several such Compton-suppressed detectors, described in the previous section, can be put together to form an array. Most of today's multi-detector Ge arrays are designed to measure the energies and coincidence relations of many  $\gamma$ -rays emitted in a cascade from high-spin states. The power of an array to collect  $\gamma$  rays is defined by the total photo-peak efficiency. This has led to the development of so-called "third-generation" arrays, such as GAMMASPHERE (USA). This array consists of  $\sim 110$  Ge detectors, covering as much of the  $4\pi$  solid angle around the target as possible. The total photo-peak efficiency of the GAMMASPHERE is  $\sim 8\%$ .

An important quantity in the discussion of large arrays of Ge detectors is the resolving power,  $R$ , which provides a measure of the spectrum quality obtainable with a particular array. The resolving power is defined as

$$R = \left( \frac{S_{E_\gamma}}{\Delta E_\gamma} \right) P/T \quad (3.11)$$

where  $\Delta E_\gamma$  is the full-width at half-maximum resolution of the measured  $\gamma$  rays,  $S_{E_\gamma}$  is the average energy separation between consecutive  $\gamma$  rays in the cascade, and  $P/T$  is the peak-to-total ratio. The equation 3.11 shows that the only way to improve the resolving power is to either increase the peak-to-total ratio,  $P/T$ , or to reduce the energy resolution,  $\Delta E_\gamma$ . In practice, it is difficult to increase the peak-to-total ratio apart from suppressing the Compton events.  $\Delta E_\gamma$  has four major contributing factors. These are:

- the intrinsic resolution of the detector,  $\Delta E_{in}$ , which is a property of the individual detector
- Doppler broadening due to the opening angle of the detectors,  $\Delta E_D$ , which can be improved by using “segmentation”, or clusters of smaller detectors
- Doppler broadening due to the angular spread of the recoils,  $\Delta E_R$ , which can be improved using a “kinematic correction”
- Doppler broadening due to the velocity distribution of the recoils,  $\Delta E_V$ .

These factors contribute as follows:

$$\Delta E_\gamma^2 = \Delta E_{in}^2 + \Delta E_D^2 + \Delta E_R^2 + \Delta E_V^2. \quad (3.12)$$

The limit of observation of a array depends on the resolving power and total photo-peak efficiency. For a given resolving power it decreases rapidly with increasing fold, while for a given photo-peak efficiency the limit of observation increases with fold. Thus, an optimum fold must be used to obtain the lowest possible limit of observation. With the latest generation of germanium arrays, the smallest limit of observation that

can be achieved is around  $1 \times 10^{-4}$ , with an optimum fold of 4 [52, 53]. This means that, if the total reaction cross section is 1 barn, nuclei produced with cross sections of around  $100 \mu\text{b}$  can be studied. Hence, large arrays are necessary for the observation of weaker channels. To achieve this, the nuclear physics community of India decided to come together with their resources to form a large array of clover detectors. This array is described in the following section.

### 3.4.1 Indian National Gamma Array at IUAC

The Indian National Gamma Array [22] is a national facility for nuclear structure studies and setup as a joint collaboration between various institute in India like IUAC, New Delhi, TIFR, Mumbai, SINP,VECC, and IUC-DAEF, Kolkata. At present this array consisted of 17 Compton suppressed clover detectors as shown in Fig. 3.5 although it had 24 detector positions, each capable of housing one clover detector and the corresponding anti Compton shield (ACS) in two hemispheres to cover most of the available solid angle. The photo-peak efficiency of the array is  $\sim 5\%$  and the detector to target distance is  $\sim 24.0$  cm. The total coverage by Ge crystals is about 25% of  $4\pi$ , Gamma-rays were detected by the clover detectors, placed at  $32^\circ$ ,  $57^\circ$ ,  $90^\circ$ ,  $148^\circ$ ,  $123^\circ$ , with respect to the beam direction. The experiments for this thesis work was performed using the Indian National Gamma Array (INGA) setup at IUAC, New Delhi during end of September 2008. A NIM based high voltage supplies has been developed at IUAC for biasing Germanium and BGO/ACS detectors. A high voltage power supply has been developed using switch mode technique and high voltage is generated by Cockroft Walton multiplier. The power supply have an automatic output ramping facility where output always starts at zero volt and then ramp up to the value set by the front panel potentiometer at the chosen ramping rate. For BGO/ACS Detector, AC powered supplies housed in double width NIM module. Power supply have two regulation loops to control power dissipation and to regulate output voltage. High grade insulating materials are used to avoid local discharge and EMI for achieving low ripple and noise. Power supplies are protected for over load and short circuit.

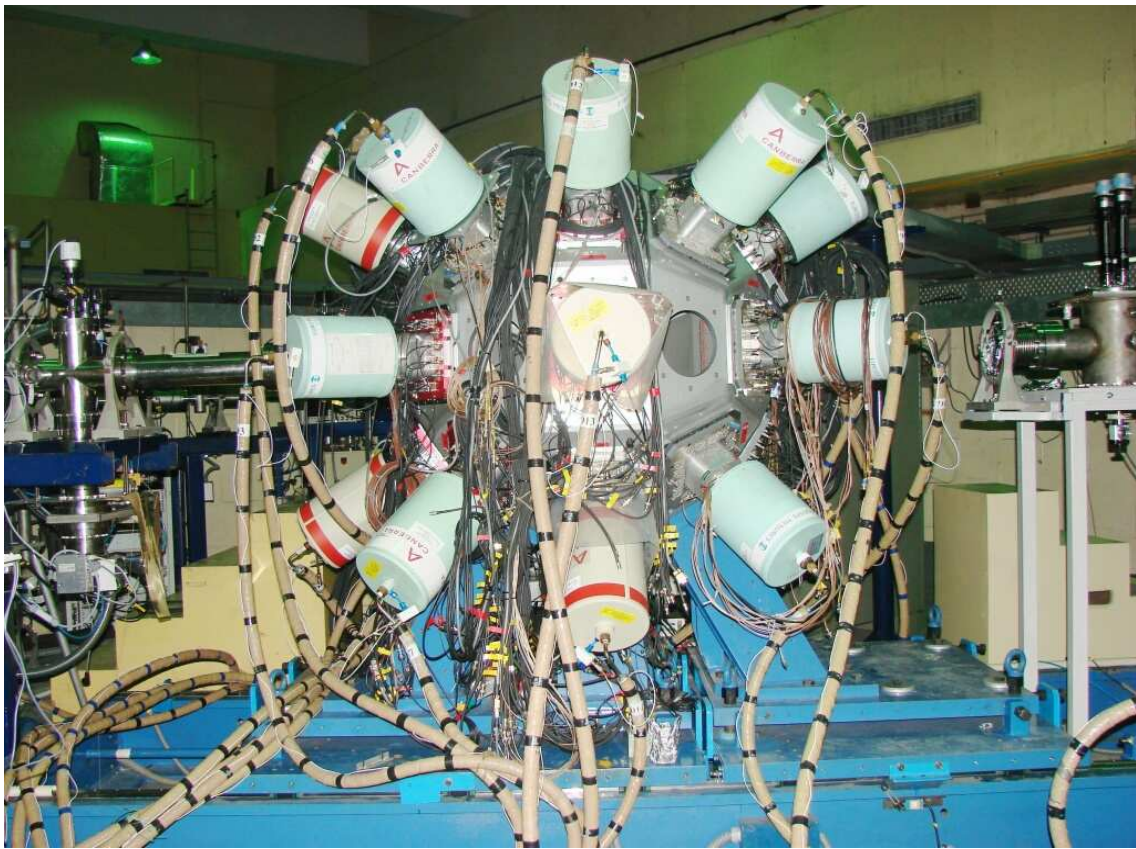


Figure 3.5: The pictorial view of the Indian National Gamma Array setup at IUAC, New Delhi

## 3.5 Electronics and data acquisition system for INGA

The Indian National Gamma Array (INGA) is the multi detector arrays at IUAC, New Delhi. The electronics requirement of any such standard  $\gamma$  detector array are as follows:

- Rejection of unwanted Compton scattered  $\gamma$ -rays. This is achieved by vetoing out the signal from clover detector with the signal from the BGO shield.
- To extract the energy and timing information from the detector signal.
- Coincidence between two or more  $\gamma$ -rays. This is achieved by having a trigger only when two or more clover detectors fire.

The need to provide the large number of data channels in a typical experiment puts severe constraints on the design of front end electronics. The front end electronics of INGA array has following dedicated setup:

- Energy and timing signals from the 17 clover.
- Anti-Compton logic for each clover.
- Coincidence logic for Compton suppressed  $\gamma$ - $\gamma$  measured as fold.
- Multiplicity logic for suppressed gamma fold
- Gating and pile up rejection for individual channels

### 3.5.1 Analog signal processing and data acquisition trigger generation

The timing and energy signals from different detectors are processed through a complex circuit and finally appears as digitized outputs which were interfaced to the data acquisition system. The clover detector has four energy and four timing signals corresponding to the individual four crystals. The pre-amplification of all these 8 signals are achieved inside the detector housing. Then these energy and time signals are sent

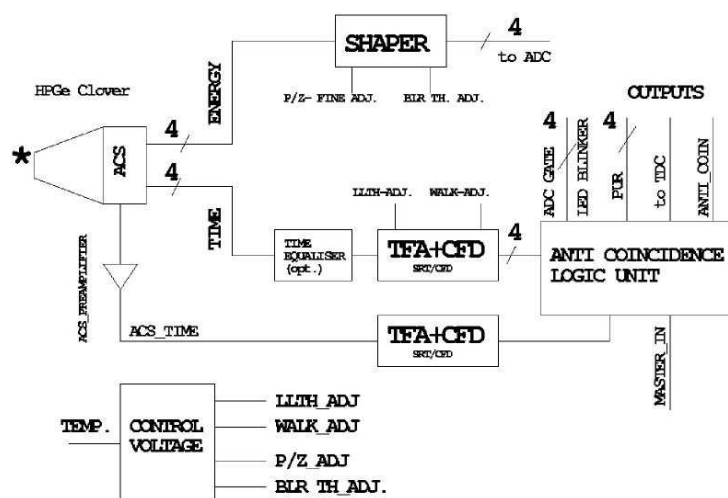


Figure 3.6: Block diagram of clover electronics

to clover module [54] (developed at IUAC electronics laboratory). One clover module support one clover detector and its corresponding ACS. Clover module is double width NIM module consisting of four number of high quality shaper amplifier and corresponding four numbers of Timing Filter Amplifier and Constant Fraction Discriminator (TFA+CFD) cards as shown in Fig. 3.6. Additional TFA card is provided to handle signal from ACS detector to generate Anti-Coincidence (ACOIN) signal. All the timing signals generated are processed in Anti Coincidence Logic (ACL) card in order to generate ADC Gate, Pile Up Rejection (PUR),  $\overline{\text{Ge(ACS)}}$ , ACOIN, TDC STOP logic signals. The amplified signal from the spectroscopic amplifier is fed into the analog to digital converter (ADC) for recording the energy information proportional to the pulse height. The OR of all 4 suppressed Ge output (A Coin) is used for generating the MASTER trigger. The block diagram of the electronics for the Compton suppression is shown in Fig. 3.7. The timing signal from the Ge is given to the TFA and the output of this TFA is fed to the constant fraction discriminator (CFD) for getting the OR of the 4 timing signals. The threshold of the clover CFD's are set just above noise by seeing the output of the TFA triggered with the CFD output. The CFD pulse width is for clover detector is kept at 50 ns. The timing signals from the BGO shield is given to a CFD through a TFA. To ensure that the Ge signal is at the centre of the ACS signal and to take care of the time walk in Ge signal, the Ge CFD output is delayed before



of detectors) discriminator are taken as inputs to the linear sum module (Philips 744). The output of linear sum module is then fed to hex discriminator (Philips 711) where threshold level have to set on the three different channels of this module according to the desired multiplicity selection ie, single fold, two fold and three fold. The output from the discriminator is a basic master trigger. The output corresponding to the higher fold ( $f \geq$ ) was delayed by 300 ns with respect to single output used as veto for the master trigger generation. In this way a coincidence between two or more  $\gamma$ -rays is ensured for each event. The other veto to the master trigger was the busy signal generated by the trigger generator module on the receipt of master trigger by the trigger generator. The timing information from the clover detectors are recorded by using a 16 channel CAMAC Time to Digital Converter (TDC). The Master gate provides the common start signal for this and the individual clover CFD outputs which are delayed by  $\sim 200 - 400$  ns serve as the stop signal. The total number of modules used in INGA array electronics are too large to fit in within a single CAMAC crate. A multi crate system has been developed for distributed readout and analysis data. New software CANDLE [55] is used to for three CAMAC crates with parallel read out of all the crates. It can handle up to  $10^4$  triggers/sec. Fast ADCS (conversion time  $\sim 10 \mu\text{s}$ ) have been used which are also developed at IUAC. List mode data contains event by event energy and timing information from all detectors are recorded and the compressed list mode data is stored in hard disc.

# Chapter 4

## Target Preparation and Data Analysis

This chapter starts with the description of procedure and method followed in the preparation of isotopic  $^{50}\text{Cr}$  target which is one of the important aspect in nuclear physics experiments. This target is required for an experiment to study the exotic nuclear shapes in 70-80 mass region using Indian National Gamma Array (INGA) facility. For this lifetime study the desired target should be of approximately  $0.50 \text{ mg/cm}^2$  to  $1 \text{ mg/cm}^2$  thick and backed with some high  $Z$  material. According to our need we have chosen  $^{50}\text{Cr}$  target backed by high  $Z$  material (gold) to stop the recoils as quickly as possible. As chromium has very poor adhesive properties we have taken some precautions during deposition. The first section will describe different type of modifications adopted and steps followed to fabricate a good quality isotopically enriched  $^{50}\text{Cr}$  target on gold backing. After that a brief description of off-line data analysis is presented. Finally, methods of measuring the lifetimes of high spin states and extraction of transitional quadrupole moments from the measured lifetimes will be discussed in detail.

### 4.1 Properties of chromium

Isotopically enriched chromium was available to us in the form of steel gray, hard, metallic form. It has very high melting point. The properties of chromium are shown

in the Table below:

Table 4.1: Physical properties of chromium isotopes.

Atomic Number	24
Atomic Weight	50
Melting Point	1907°C
Boiling Point	2671°C
Density	7.18 g/cm <sup>3</sup>

Chromium is having five stable isotopes and twenty one unstable isotopes. The abundance of the stable isotope is shown in Table below

Table 4.2: Abundance of the stable chromium isotopes.

Isotopes	Abundance(%)
50	4.34
51	syn
52	83.78
53	9.50
54	2.36

## 4.2 Details of the target preparation

We have used the rolling mil for making the gold foils and Ultra High Vacuum Evaporator for the deposition of chromium on gold backing. It is equipped with scroll pump, turbo pump and cryo pump. This chamber provides a vacuum of the order  $2 \times 10^{-8}$  Torr. This evaporator is having 6 kW electron gun and has four copper crucible of different sizes as shown in Figure 4.1. There are two methods in this ultra high vacuum chamber to evaporate the target material viz. resistive heating method and electron gun. Details are given in Ref. [56]. The resistive heating is used for material having low melting point. The 6 kW electron gun method is mainly used for targets having high melting point. We have taken Graphite boat and the target material is kept inside the boat. The accelerated electron beam is focussed on the boat. After hitting the

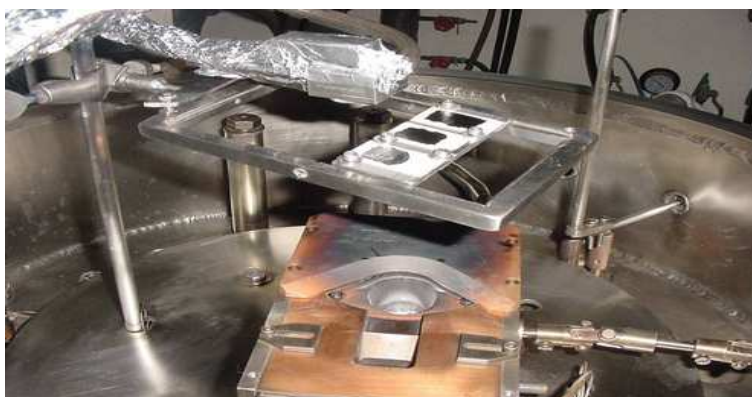


Figure 4.1: Inside view of ultra high vacuum chamber used for deposition

surface of the target material the kinetic energy of electron beam is converted into heat energy and due to this the material gets evaporated. This evaporator is equipped with a quartz crystal to monitor the thickness of deposition. A manually operated shutter is placed in the system to control the impurity deposition .

### 4.3 Experimental procedure

The preparation of isotopic chromium is divided into the following steps:

- Preparation of gold foils .
- Deposition of natural chromium on gold.
- Deposition of isotopic chromium on gold by evaporation method.
- Thickness measurement using X-ray florescence method.

#### 4.3.1 Preparation of gold backing foils

One starts the prepration of Au backing from thicker foil and puts it in between two hard fine polished plates and start pressing the plates (called rolling later). Depending on the physical property of material different type of plates are used. For example for gold, nickel, iron and aluminum, steel plates are used where as for soft material like lead and tin, teflon plates are used. It is quite important to prepare a good quality



Figure 4.2: Graphite and Tantalum crucible used for keeping the target material inside plate to get a good quality target. By a good plate it means the inside surface of plate should be clean so that while pressing the plates any unwanted dust particle should not get inside the target. We have prepared  $\sim 12 \text{ mg/cm}^2$  gold foil for deposition of enrich target and  $\sim 4 \text{ mg/cm}^2$  for thickness measurement by alpha scattering method.

### 4.3.2 Deposition of natural chromium

The deposition of chromium was done in ultra high vacuum evaporator by electron gun evaporation method. Before we attempt to make enriched isotopic target we tried to do trial runs with natural chromium because the isotopic material is very costly and the material available with us was only 100 mg. The natural chromium was in the form of fine metallic lamps. We took around 100 mg material for all trials. Since chromium has high melting point we have tried with different materials boat. First we used cylindrical crucible of tantalum of length around 1 cm and made drill of 3 mm diameter in side the rod shown in Fig. 4.2. The vacuum in the chamber was  $2 \times 10^{-8}$  Torr. Initially, we gave a small current around 40 - 50 mA and waited for 15 minutes so that steady heat is generated inside the chamber. Later, we increased the current to 100 mA. The tantalum crucible gets melted at this current. The distance between the tungsten boat and the gold frame holder was 7 cm during evaporation. Again we made graphite crucible ( because of higher melting point ) and put a shutter in between the target holder containing gold foils and target material. Apply small amount of current for 30 minutes so that impurity can be removed and after that shutter should be take out. Now increase the current slowly in step of 2 - 3 mA till the whole material gets deposited. Since the enriched material is very costly and having in very small amount we have repeated this procedure 4 - 5 times.



Figure 4.3: A front view of enrich chromium target deposited on gold backing

### 4.3.3 Deposition of isotopic chromium

After successful deposition of natural chromium, we next tried with the isotopic  $^{50}\text{Cr}$  material. The material available with us was around 80 mg. We took 80 mg of isotopic chromium in the graphite crucible for deposition. The vacuum in the chamber was around  $2 \times 10^{-8}$  Torr. The electron beam was focused on the target material. Since material was in the form of small pieces we gave a small current of around 40 - 50 mA for 30 minutes. After 30 minutes we saw that material gets melted and they were combined to form a single ball. Then we followed the same procedure which was followed during natural chromium deposition. The evaporation continued for 3 hours and finally succeeded in depositing the isotopic chromium on the gold backing and is shown in Fig. 4.3. Thickness was around  $550 \mu\text{g}/\text{cm}^2$  which is measured by X-ray fluorescence method discussed in section 4.3.4.

### 4.3.4 Thickness measurement by X-ray fluorescence method

Since enriched chromium target is used for the measurement of lifetimes of high spin states using Doppler-shift attenuation method, much accurate thickness is needed for the better understanding of slowing down history. The target thickness has been measured by X-ray fluorescence method (XRF) also. The brief procedure is described below and details of the source, target, and detector geometrical arrangement used for the present Li-subshell XRF measurements can be found in Ref. [57]. The Mn  $K\alpha$  ( $E_{K\alpha 2} = 5.888$  keV,  $E_{K\alpha 1} = 5.899$  keV) x rays were obtained from an  $^{55}\text{Fe}$  radioisotope annular source used in conjunction with a Cr absorber. The  $^{55}\text{Fe}$  annular source is in the form of a circular flat ribbon of 34-mm diameter and 4-mm width. The  $^{55}\text{Fe}$  radioisotope

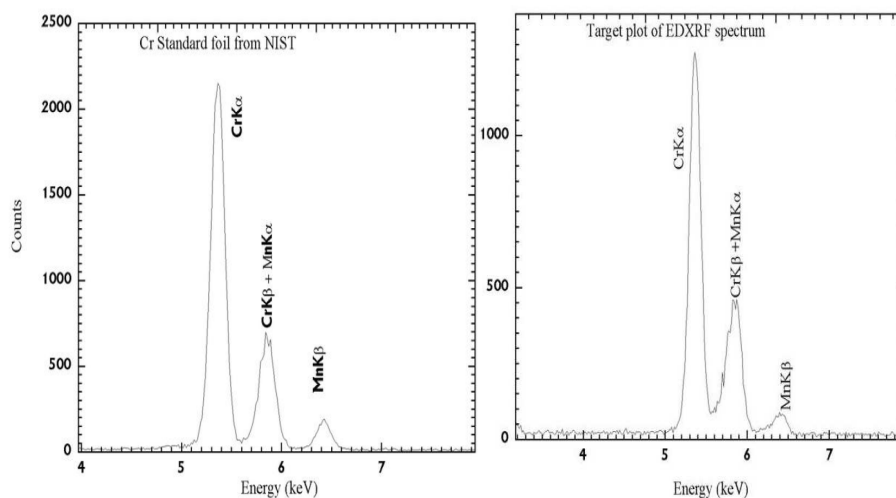


Figure 4.4: Typical spectra of the L x-rays of standard Cr target obtained from NIST and deposited Cr target

undergoes electron capture decay with  $T_{1/2}=2.73$  years and results in emission of the Mn  $K\alpha_2$ ,  $K\alpha_1$ , and  $K\beta_1$  x rays with probabilities of 8.2, 16.2, and 2.86 per 100 decays, respectively. In order to measure the thickness of chromium target first we put the standard foil of known thickness provided by Nuclear Institute of Standards Technology (NIST), and measure the intensity of  $CrK\alpha$  line as shown in the left frame of Fig. 4.4 and then put the actual target at the same position and find out the intensity of same X ray line (shown in right frame of Fig. 4.4). By comparing the two we can get the desired thickness which is  $550 \mu\text{g}/\text{cm}^2$  used in the present experiment.

## 4.4 Data analysis for $\gamma$ -ray spectroscopy

Main objective of data analysis in  $\gamma$ -spectroscopy are:

- To look for  $\gamma$ -transition following the nuclear reaction
- To look for correlations  $\gamma$ - $\gamma$ ,  $\gamma$ - $\gamma$ - $\gamma$  etc. to search for sequence of transition
- To measure the intensity of each transition to estimate the population of each level
- To establish the level scheme

- To extract the additional information like lifetimes of the states which gives valuable information about nuclear matrix element

Since the nuclear de-excitation process is statistical in nature, there is no time correlation between successive events. Only the probability of pulse height distribution for individual events is of statistical importance. As a result, the single parameter data are generally recorded as multi-channel histograms where the channel number is proportional to the energy or pulse height of the incident radiation and the counts/channel refers to the number of times a pulse height within a given range of values is observed within a fixed counting time interval. Data from multi detector arrays are generally stored in list mode format where all the parameters associated with an event (i.e. energy and timing from each detector) along with some identification tags are recorded 'event' by 'event'.

During off-line analysis, the data records are read back and unpacked to retrieve the original ADC values associated with each event. Prior to the detailed analysis, the data is pre-processed using suitable data analysis software packages: (a) to correct for any off-line drift (b) to perform energy calibration (c) gain matching (to make the data detector independent). The details of these procedures are given in Refs. [58, 59].

In the present work, data were collected in double coincidence (i.e. when two or more clover detectors fire) and in LIST mode. These data were analyzed to measure the lifetime of high spin states in  $^{75}\text{Kr}$  and  $^{75}\text{Br}$  nuclei. The analysis procedures are being described in detail in this section. The program INGASORT [60], RADWARE [61] and DAMM [62] have been used for the data analysis through out the present work.

#### 4.4.1 Correction for gain drift

Generally, in-beam  $\gamma$ - ray spectroscopy experiments are carried out for a period of 3 - 4 days. During this span of time, possibilities of any gradual drifts in amplifier gain (or electronic instabilities) can not be avoided. Therefore, first of all this drifts have to be corrected before any further processing of the data. This is done during the pre-processing stage. An automatic correction for instrumental (electronic) drifts have

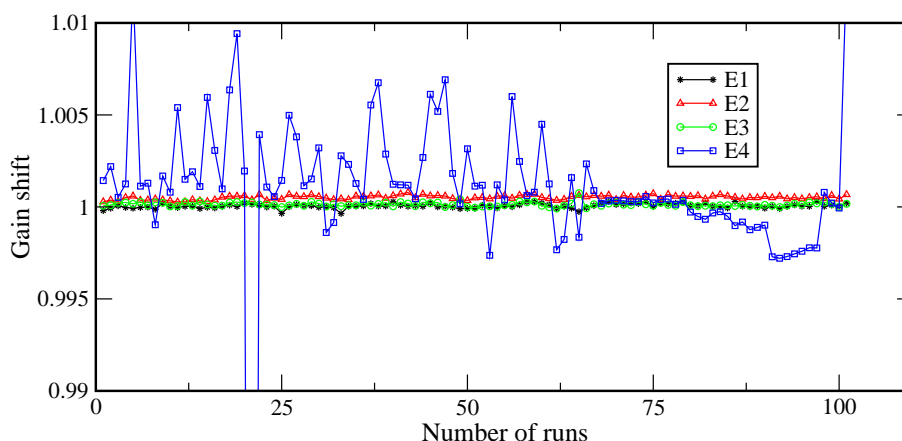


Figure 4.5: Variation of gain shift for all 4 crystal of clover 16 during experiment

been done by subroutine (GAINMATCH) of the INGASORT program.

The variation of gain shift during the entire experiment for all four crystal of clover number 16 as representative is shown in Fig. 4.5. From the plot it is clear that out of four crystals of clover, three have very slight shift as compared to the 4th crystal which has a very large gain shift. However, in some crystals after the few runs there is large shift. These crystals are excluded from the further sorting either fully or partially, from where they are showing shift. This gain shift mostly arises due to the non-linear behavior of the amplifier gain. If the gain shift is  $\leq 0.01$  (in absolute unit) then no correction is required, whereas correction for the gain drift is required if observed shift exceeds 0.01 (in absolute unit). The drift correction is achieved in the following steps : (i) generation of 1D (one-dimensional) spectrum from the list-mode data ; (ii) one of the spectrum is selected as the reference spectrum. Two well separated distinct peaks, one at low-energy region ( $\sim 100$  keV) and the other at high-energy region ( $\sim 1500$  keV), are identified; (iii) The aim of the procedure is to align these peaks in the subsequent data sets to the same position as that in the reference spectrum.

#### 4.4.2 Energy calibration and gain matching

The energy calibration and subsequent gain-matching of the clover detector was achieved with the use of standard radioactive source having a number of strong  $\gamma$ -transitions of known energy e.g.  $^{152}\text{Eu}$ . This was chosen because of the wide energy range from 121.78

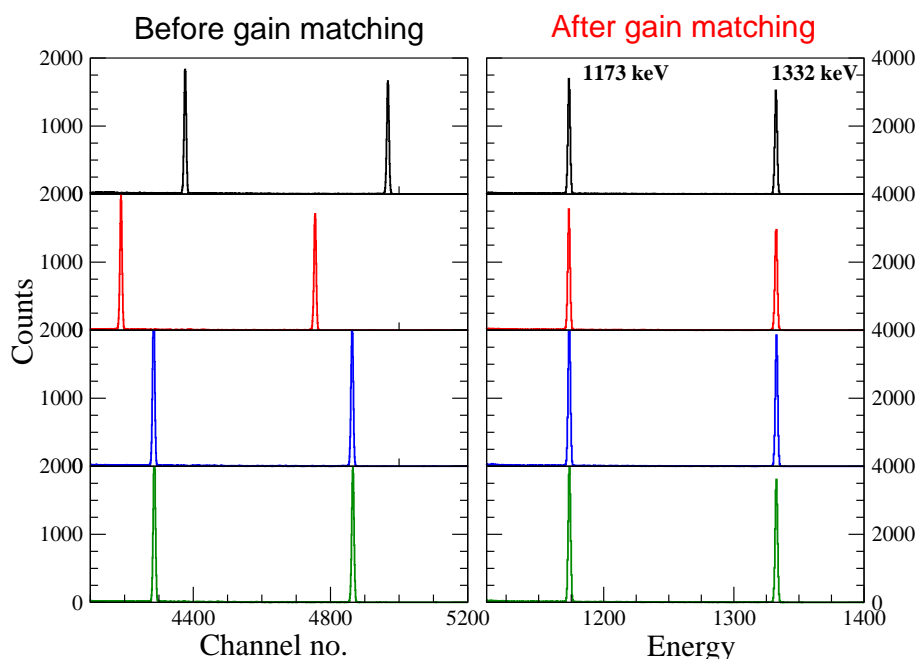


Figure 4.6: The gain matching process

keV to 1408.01 keV. Analysis packages like CANDLE [55] is used for the calibration during online data collection while INGASORT [60] is used for off-line analysis. An approximate two point linear calibration using the transitions at 121.78 and 1408.01 keV peaks is first performed by visually identifying two prominent lines in the spectrum. A slight nonlinearity for large pulse height can be corrected by using an automatic peak search program of INGASORT for the second order polynomial fit ( $E\gamma = a + bX + cX^2$ , where  $X$  is the channel number). The observed channel centroid would provide an energy calibration with an accuracy of  $\sim 0.1$  keV within the energy range 0 - 2 MeV. For analyzing data from single detector, it is easy to collect data with any appropriate gain and then convert channel number to energy during analysis. However data from multi detectors requires the storage of histogram with fixed keV/channel (typically 0.5 or 1.0 keV/channel). Software gain matching of different detectors is possible by converting each channel event into corresponding energy. An illustration of the gain matching process is depicted in Fig. 4.6. The left panel of the figure shows the data before the gain matching while the right panel shows the same data set after the gain matching. Since the individual crystal signals are processed by independent front end electronics, it necessarily does not results in the energy peak being digitized to the

same ADC channel for all the detectors. As seen from the left panel, the 121 keV peak occurs at different channels for the four crystals belonging to the same clover. After the gain matching is done, this gamma peak from the four crystals is matched to the one common channel. Fig. 4.6 shows the gain matching process, with the help of radioactive source ( $^{60}\text{Co}$ ) data. Since clover detector are used in addback mode it is very important to do proper gain matching before going to actual analysis.

### 4.4.3 Efficiency calibration

Since detection efficiency for  $\gamma$ -ray changes as a function of  $\gamma$ -ray energy, the next step is to do efficiency correction. The efficiency determination is achieved using a source emitting several transitions whose relative intensities are accurately known. From a measurement of the corresponding photo-peak area, the energy dependence of the photo-peak efficiency can be directly determined. Useful sources for energy calibration for different energy range are  $^{152}\text{Eu}$  and  $^{133}\text{Ba}$ . For the accurate determination of efficiencies, it is essential to keep the source exactly at the target position, so as to obtain appropriate photo peak efficiency for the actual in-beam data. A detailed description of above procedure can be found in Refs [58, 60]

## 4.5 Analysis of $\gamma$ - $\gamma$ coincidence data

After the proper gain-matching and raw sorting, different  $E_\gamma$ - $E_\gamma$  matrices are generated using list mode data by using the CANDLE [55] and INGASORT [60] program. These matrix were analyzed using the software INGASORT and RADWARE for getting the coincidence relations. From these coincidence relations the levels were placed in the decay scheme. Finally, for the application of Doppler-shift attenuation method (DSAM), line shapes were obtained from the background-subtracted spectra by using DAMM program.

### 4.5.1 $\gamma - \gamma$ Matrices

The normal approach to the analysis of  $\gamma - \gamma$  coincidences is for each event to store the energies of the two detected  $\gamma$ -rays in a two dimensional histogram, usually referred to as the matrix. The importance of storing the two dimensional histograms is the ease with which the energy correlation information may be extracted through a one-dimensional (1-D) projection from the two-dimensional (2-D) array. An example of 2d  $\gamma - \gamma$  coincidence matrix is shown in Fig. 4.7. Each axis of the matrix corresponds to the energy of the detected  $\gamma$ - rays. In the present work, the matrix has a dimension of  $4096 \times 4096$  channels, with the energy calibration 0.5 keV/channel. The number of counts in each (x, y) channel of the matrix tells how many pairs of  $\gamma$ -rays, with energies ( $E_{\gamma x}$ ,  $E_{\gamma y}$ ), have been detected.

For the application of present work following  $4k \times 4k$  matrices were constructed.

1.  $E_{\gamma}$ - $E_{\gamma}$  was sorted from all the detector without keeping the detector identification. With the large number of  $\gamma$  detectors in  $4\pi$  geometry, the isotropic direction of  $\gamma$  ray is assumed. Further the matrix was symmetrized to make the two axes equivalent. This type of matrix was utilized for constructing the level scheme.

2. As expected, the line shapes at the extreme forward and backward angles ( $32^\circ$ ,  $148^\circ$ ) are most sensitive to the fitting parameters, because the energy spread of the line shapes is larger as compared to angles of observation closer to  $90^\circ$ . Therefore for the measurement of lifetime by DSAM technique (described in later section) various asymmetric matrices were constructed by keeping above mentioned point in mind, namely the events in the  $148^\circ$  or  $32^\circ$  detectors along one axis and all other detectors along the second axis. While in case where gating above the transition is used, events at  $90^\circ$  are put along the second axis.

### 4.5.2 Background subtraction

The sorted  $\gamma$ - $\gamma$  coincidence data set contains the following possible combinations :

$$P = P_i P_j ; P_i B_j ; B_i P_j ; B_i B_j$$

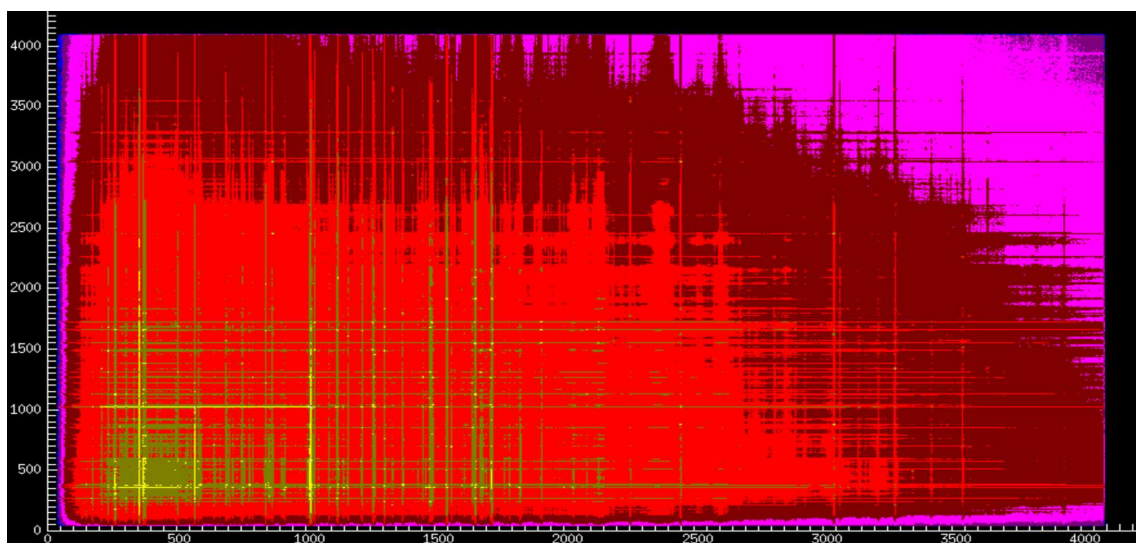


Figure 4.7: Pictorial view of two-dimensional matrix

where,  $P$  corresponds to the photo-peak information and  $B$  corresponds to the background. Of these pairs only the  $(P_i, P_j)$  combination contains genuine information. The process of eliminating or subtracting the other 3 combinations is known as background subtraction. The background in the matrix consists of Compton scattered events. Such events occur when one or both of the  $\gamma$ -rays deposited less than their total energy in the detectors. This background has to be correctly subtracted from each gated  $\gamma$ -ray spectrum. For the present line shape analysis background subtracted matrix were used, which is done by programme written by Palit [63], with RADWARE packages.

### 4.5.3 Total projections and gates

The total projection on the x axis of the matrix is a one dimensional  $\gamma$ -ray spectrum, obtained by summing the counts in all y channels for each x channel, and vice versa for the total projection on the y axis. For a symmetric matrix, the x and y total projection spectra are identical. A typical projection spectra along the x-direction (Fig. 4.8) shows the number of strong transitions of energies 131, 179, 191, 293, 689, 775 and 830 keV corresponding to different evaporation channels. By selecting a narrow window, often called a gate, e.g. on the y axis, and projecting out (sometimes called slicing) the one dimensional  $\gamma$ -ray spectrum in the x direction, a coincidence  $\gamma$ -ray

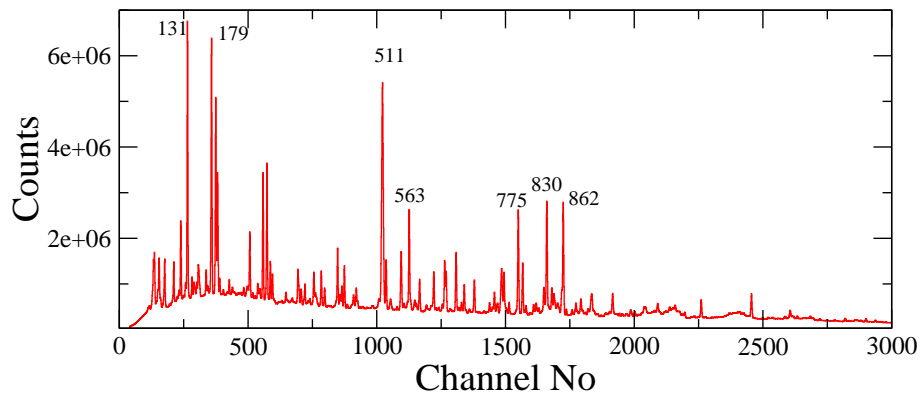


Figure 4.8: Total 1-D projection spectrum

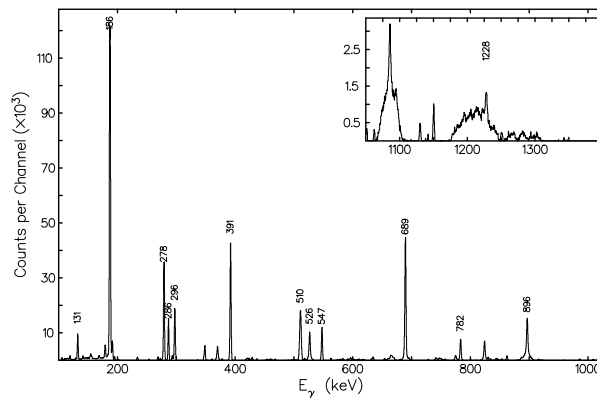


Figure 4.9: Spectrum showing the gate on 191 keV transition of  $^{75}\text{Kr}$

spectrum is obtained. If a gate is set within a range of  $y$  channels, that correspond to a peak in the total projection spectrum, the obtained spectrum, contains information about which other  $\gamma$ -rays the peak is in coincidence with. By setting gates on different peaks and examining the peaks in the gated spectra, it is possible to determine the different de-excitation paths of the excited nucleus. The coincidence spectra, however do not contain explicit information about the order of the  $\gamma$ -rays in each cascade. To determine the level scheme, the transitions and the levels must be ordered. This can be done by examining multiple gates, which can be done in a convenient way using the program `escl8r` of RADWARE. An example of gated spectra with gate on 191 keV transition (which is one of the lower transition of  $^{75}\text{Kr}$ ) is shown in Fig. 4.9.

## 4.6 Measurement of electromagnetic transition probabilities

Study of electromagnetic properties of nuclei give detailed information about the nuclear levels. These involve the measurements of multipolarities of the  $\gamma$ -rays, measurement of electromagnetic transition strengths and moments. The angular distribution and angular correlation measurements give information about the order of the multipole, while polarization measurements and conversion coefficients determine the electric and magnetic nature of the transition. The electromagnetic transition strengths are directly related to the wave functions of the levels involved. This gives crucial information about the structure of the nuclei and provide stringent test of nuclear models. Thus, in order to understand the shape and structure of the nucleus at high spins it is very important to measure the transition probabilities of these  $\gamma$  transitions. For measuring transition strengths we need to measure the lifetimes of the nuclear levels. The lifetimes of nuclear levels are related to transition strengths as discussed below. The transition probability of a  $\gamma$ -ray of multipolarity  $L$  from an excited state to a final state is given by,

$$\lambda_L = \frac{8\pi(L+1)}{\hbar[(2L+1)!!]^2} \left(\frac{E_\gamma}{\hbar c}\right)^{2L+1} B(L) \quad (4.1)$$

where  $B(L)$  is the reduced transition probability and is given by,

$$B(L) = (2J_a + 1)^{-1} | \langle \psi_b || M(L) || \psi_a \rangle |^2 \quad (4.2)$$

where,  $M(L, \mu)$  is the electromagnetic multipole operator. This reduced probabilities represents the sum of squared  $M(L, \mu)$  electromagnetic multipole operator over the  $\mu$  substates averaged over the  $(2J_a + 1)$  initial magnetic substates.

The reduced transition probabilities for different multipole orders are given by,

$$B(E1) = 6.29 \times 10^{-6} E_\gamma^{-3} \lambda(E1) e^2 fm^2 \quad (4.3)$$

$$B(E2) = 8.20 \times 10^{-10} E_\gamma^{-5} \lambda(E2) e^2 f m^4 \quad (4.4)$$

$$B(M1) = 5.68 \times 10^{-14} E_\gamma^{-3} \lambda(M1) \mu_N^2 \quad (4.5)$$

$$B(M2) = 7.41 \times 10^{-8} E_\gamma^{-5} \lambda(M2) \mu_N^2 f m^2 \quad (4.6)$$

where,  $E_\gamma$  in  $MeV$  and  $\lambda(L)$  in  $sec^{-1}$ .

To obtain the reduced transition probabilities, we need to measure experimentally the decay constant,  $\lambda(L)$ . The decay constant is defined in the radioactive decay law by the following relation,

$$I(t) = I_0 \exp(-\lambda t) \quad (4.7)$$

This gives the mean lifetime of the state. If the state decays to more than one final state, the branching ratios  $\frac{\lambda_i}{\sum \lambda_i}$  must be measured. In the present experiment conversion coefficients are small.

The transition rates, under the assumption that the transition is due to a single proton moving from one shell model state to another, can be estimated from

$$B(EL)_W = \frac{1}{4\pi} \left( \frac{3}{3+L} \right)^2 (1.2A^{1/3})^{2L} e^2 f m^{2L} \quad (4.8)$$

$$B(ML)_W = \frac{10}{4\pi} \left( \frac{3}{3+L} \right)^2 (1.2A^{1/3})^{2L-2} \mu_N^2 f m^{2L-2} \quad (4.9)$$

Clearly, these Weisskopf estimates are not realistic calculations of the transition rates, but provide values to classify measured  $B(E2)$  to be collective ( $\sim 100$  W.u.) or single particle ( $\sim 10$  W.u.) excitation.

Once the transition rates are measured, the shape of the nucleus can be obtained from it in the following way. In case of a deformed nucleus with axial symmetry, we

can calculate the transition quadrupole moment  $Q_t$  from the  $B(E2)$  values using the following relation,

$$B(E2; I \rightarrow I - 2) = \frac{5}{16\pi} Q_t^2 \langle I2K0 | (I - 2)K \rangle^2 \quad (4.10)$$

Here  $B(E2)$  is in unit of  $(e\text{ b})^2$ ,  $Q_t$  in  $e\text{ b}$  and  $K$  is the projection of total angular momentum on the symmetry axis and the term in brackets is a Clebsch-Gordon coefficient. It should be mentioned that the above equation is almost independent on the  $\gamma$  degree of freedom.

From the above discussion it is clear that the measurement of lifetime of a nuclear state is crucial and the different methods of measurement of lifetimes of nuclear states will be described in detail in the following section.

## 4.7 Methods of lifetime measurements

Depending on the time range, following methods are used to measure lifetimes of nuclear levels.

- Irradiation and counting ( $>$  min)
- Pulsed beam method for lifetimes  $\sim 10^{-7}$  to  $10^{-9}$  seconds
- Recoil distance method for lifetimes  $\sim 10^{-9}$  to  $10^{-12}$  seconds
- Doppler-shift attenuation method for lifetimes  $\sim 10^{-12}$  to  $10^{-14}$  seconds

for *irradiation and counting*, the isomer is produced by irradiation, taken to a low-background area and counted for a few half-lives. If the life time is sort ( $<$ ) it would be necessary to collect the data over many counting cycles to improve the statistics.

In the *pulsed beam method*, the nuclear state is populated with a pulsed beam with a period greater than the lifetime of the nuclear state. Then this level will decay through  $\gamma$  emission before the next pulse arrives. The variation of the intensity of the

$\gamma$  ray over the time period between the two beam pulses with show an exponential decay curve given by

$$N(t) = N_0 \exp(-t/\tau) \quad (4.11)$$

where,  $N_0$  is the total number of nuclei populated. and  $\tau$  is the mean lifetime of the level.

In the *recoil distance method*, the excited nuclear states are produced by bombarding a thin uniform foil with a heavy ion beam. The highly excited reaction product recoil out of the target into vacuum and the  $\gamma$ -rays emitted during this time are Doppler shifted depending on where we are seeing from. They are blue shifted in the forward angles and red shifted in backward angle. These recoils are stopped in a thick stopper foil. Once the recoil come to rest in the stopper the  $\gamma$  rays are not shifted and we get a stopped (unshifted) peak. The ratio of shifted to unshifted peak intensities at different stopper to target distance will give the lifetime of the nuclear state.

In the *Doppler-shift attenuation method* [64], the target is evaporated or rolled onto a thick stopper. Hence, the recoiling nucleus first moves in the target material and then in the stopper. The velocity of the recoiling nucleus is continuously decreasing and one gets a broad shifted peak along with the stopped peak giving rise to a shoe like structure. This method is shown in Fig. 4.10. Most of the nuclear lifetimes of the new structures found in the present work are in the range of  $10^{-12}$  to  $10^{-14}$  seconds and hence, this method has been extensively used. This method will be described in detail in the following section.

## 4.8 Doppler-shift attenuation method

In this method, the recoiling nucleus slows down in the target and backing, the  $\gamma$  rays de-exciting the short lived levels having a lifetime of the order of  $10^{-14}$  to  $10^{-12}$ s will be Doppler shifted. The continuous distribution in energy of the recoiling ions shows up as a line shape in the  $\gamma$  spectrum. This distribution in energy is on the higher side

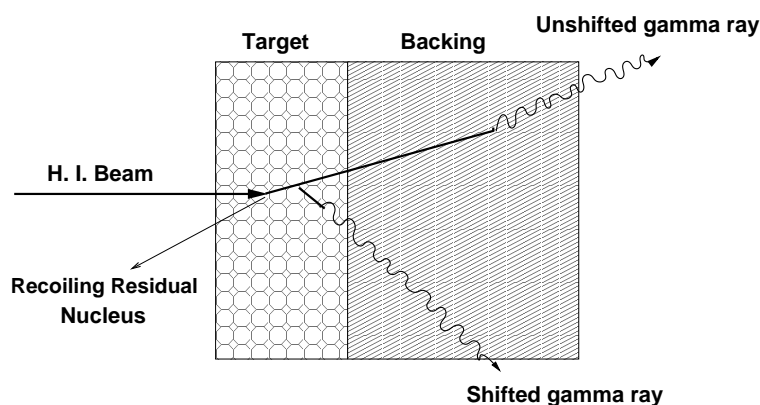


Figure 4.10: Figure shows the Doppler-shift-attenuation method

or lower side of the unshifted peak depending on the position  $\theta$  of the  $\gamma$  detector. The maximum shift in the observed spectrum is given by,

$$\Delta E = E_0 \frac{v}{c} \cos \theta \quad (4.12)$$

where  $E_0$  is the unshifted  $\gamma$  energy,  $v$  is the velocity of the recoiling nucleus and  $\theta$  the angle of the detector with respect to the beam direction. If the transit time is small compared to the lifetime of the level, most of the counts in the  $\gamma$ -spectrum will be in the unshifted peak. On the other hand, if the level lifetime is shorter than the travel time, most of the counts will be in the shifted part which is explained by Fig 4.11. Thus, the shape of the  $\gamma$ -spectrum depends mainly on the lifetime of the level, velocity of the recoiling nucleus and the time the recoil takes to be stopped completely in the stopper material. The shape of the spectrum is quantitatively, defined by,  $\frac{dN(E)}{dE}$ . If we know the velocity of the recoil and the energy loss of the recoil in the medium, then we can obtain the lifetime of the level from the observed line shape of the de-exciting  $\gamma$ -ray. It is crucial to know the energy loss of the recoil in the target and stopper and it is being discussed below.

### 4.8.1 Energy loss of heavy ions in materials

In line shape analysis, time dependence of the velocity of the recoil ions as it moves through the stopping medium is the main ingredient. This is given by equation,

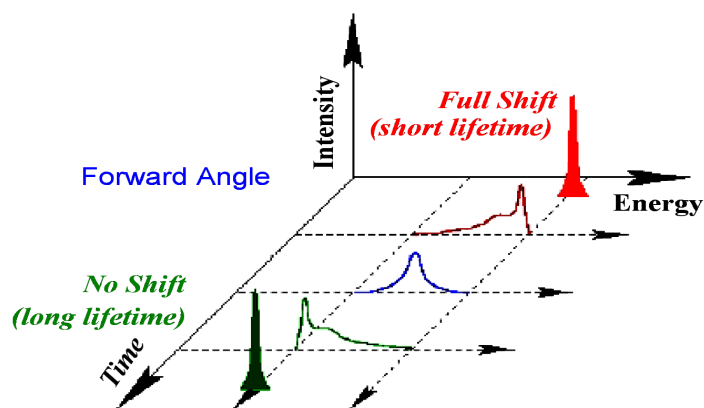


Figure 4.11: Basic principle for DSAM technique

$$\frac{dE}{dx} = -M_1 \frac{dv}{dt} \quad (4.13)$$

where,  $M_1$  is the mass of the recoiling nucleus. Thus the knowledge of stopping power  $dE/dx$  of heavy ion in stopping material is essential for DSAM line shape analysis.

The total stopping power of the ions in the stopping material has mainly two components. The first component arises due to the interaction of the moving ion with the electronic structure of the stopping material. The second component is due to the nuclear interaction. This part is important only for low velocity ions. The main contribution comes from the electronic component. The total stopping power can be written in terms of the reduced, dimensionless variable  $\rho$  and  $\epsilon$ ,

$$\frac{d\epsilon}{d\rho}|_{total} = \frac{d\epsilon}{d\rho}|_{elec} + \frac{d\epsilon}{d\rho}|_{nucl} \quad (4.14)$$

where,

$$\epsilon = 3.255 \times 10^4 \frac{A_2/(A_1 + A_2)}{Z_1 Z_2 (Z_1^{2/3} + Z_2^{2/3})} E(\text{MeV})$$

$$\rho = 1.659 \times 10^5 \frac{A_1}{(A_1 + A_2)^2 (Z_1^{2/3} + Z_2^{2/3})} x(\text{mg/cm}^2)$$

Here,  $A$  and  $Z$  represent the mass and atomic numbers, respectively, while the subscripts 1 and 2 refer to moving ion and stopping material, respectively.

### 4.8.2 Calculation of line shape

The contributions of the electronic and nuclear stopping as a function of the initial direction of motion of the recoil ( $z$ -direction) are given by,

$$-M_1 \frac{dv_z}{dt} = K_e \frac{v_z}{V_0} + K_n \left(\frac{v_z}{v_0}\right)^{-1} - K_3 \left(\frac{v_z}{v_0}\right)^3 \quad (4.15)$$

where,  $M_1$  is the mass of the recoil and  $v_0 = c/137$ .

Using equation 4.13 we can write,

$$M_1 \frac{dv_z}{dt} = \left(\frac{dv_z}{dV}\right) \left(\frac{dE}{dx}\right) \quad (4.16)$$

The probability that a  $\gamma$ -ray being emitted per unit velocity along the  $z$ -axis can be obtained by integrating the expression for  $M_1(dV_z/dt)$ . Neglecting the cubic term, Skokstad *et al.* [65] found the probability to be,

$$\frac{dN(V)}{dV} = c_1 ([V(\alpha/\tau)(\gamma^{-2} + V^2)]^{\alpha/2\tau-1} + \gamma^{-\alpha/\tau} \delta(V)) \quad (4.17)$$

where,

$V = v_z(t)/v(0)$ ;  $v(0) = v_z(0)$  is the initial velocity

$$c_1 = (\gamma^{-2} + 1)^{-\frac{1}{2}\alpha/T}$$

$$\alpha = M_1 v_0 / \rho K_e$$

$$\gamma^2 = (K_e/K_n)(v(0)/v_0)^2$$

$\alpha$  is the electronic stopping time characteristic of the medium and the recoil ion.  $\tau$  is the mean lifetime of the decaying level,  $\rho$  is the density of the stopping medium and  $\delta$  is the delta function. The probability distribution depends on two independent parameter  $\alpha\tau$  and  $\gamma$

The equation 4.17 represents the line shape of the  $\gamma$ -radiation. The term  $\gamma^{-\alpha/\tau}\delta(V)$  gives the unshifted component from the nuclei that have been completely stopped in the target. The first term corresponds to the shifted component from the moving nuclei.

### 4.8.3 Line shape analysis

The analysis of DSAM data in the present work were done with the “LINESHAPE” analysis code of J. C. Wells and N. R. Johnson [66, 67](and references therein). The Monte Carlo simulation technique was used in this program, as initially applied by Bacelar *et al.* [68, 69], for the velocity and directional history of series of recoiling nuclei. With this Monte Carlo routine, it is possible to trace both the scattering directions and the velocities of the recoiling ions to account primarily for the nuclear stopping power. The electronic stopping powers of Northcliffe and Schilling [70] corrected for shell effects were used for calculating the energy loss due to electronic scattering.

To calculate the line shape, the following effects have been taken into account,

- The energy loss of the projectile in the Cr target and the thick Au backing.
- The kinematics of the reaction which determines the recoil velocity distribution.
- The scattering of the slowing down ions.
- The cascade feeding from higher lying states.
- The effect of side feeding to the state of interest
- The resolution and efficiency of the clover detectors.
- The solid angle of each detector.

The LINESHAPE program involves minimization of  $\chi^2$  with variation of several parameters e.g. the transition quadrupole moments ( $Q_t$ ) for the transition of interest, transition quadrupole moments  $Q_t(\text{SF})$  of the modeled side feeding cascade, the intensity of contaminant peaks in the region of interest and the normalizing factor to normalize the intensity of fitted transition. The best fit was obtained through the least square minimization procedures SEEK, SIMPLEX, and MIGRAD referred in [66].

In the present work, the excited states in  $^{75}\text{Kr}$  and  $^{75}\text{Br}$  were populated by bombarding  $^{28}\text{Si}$  beam on  $^{50}\text{Cr}$  target. The target consisted of  $\sim 550 \mu\text{g}/\text{cm}^2$  isotopically enriched 96%  $^{50}\text{Cr}$  target with backing of  $\sim 12 \text{ mg}/\text{cm}^2$  gold to stop the recoiling ions produced in the reaction. Lifetimes of nuclear states obtained by comparing these experimental line shapes with the theoretically generated line shapes. The slowing down history of the recoiling nuclei was generated by using the Monte-Carlo technique with 10,000 histories and a time step of 0.01 ps. The side-feeding was modeled to be a rotational cascade of five transitions with a fixed moment of inertia of  $20\hbar^2 \text{ MeV}^{-1}$  through out the analysis. One always start the analysis from the top most transition, followed by the next transition within the cascade. Finally a global fit was performed for the whole cascade allowing all lifetimes and side feeding to be varied independently. This process of fitting was done for two extreme forward and backward angles i.e.  $148^\circ$  and  $32^\circ$ . The uncertainties in the  $Q_t$ 's and consequently in the lifetimes ( $\tau$ ) were determined by statistical method using the MINOS routine [67]. Examples of line shapes along with the best fits for a number of transitions in different bands of  $^{75}\text{Kr}$  and  $^{75}\text{Br}$  nuclei are shown in the subsequent chapters.

## 4.9 Conclusion

In the present chapter, preparation of enriched chromium target on gold backing is discussed. Details of the pre-processing of data taken and the analysis procedures are given. The later part of this chapter was devoted to describing the technique for measuring the lifetimes of nuclear states. The Doppler-shift attenuation method (DSAM) has been described elaborately, which is used in the present work for measuring the

lifetimes of the high spin states of some nuclei in 70-80 mass region . The data analysis procedures for this method has also been discussed.

# Chapter 5

## Shape Evolution at High Spin in $^{75}\text{Kr}$

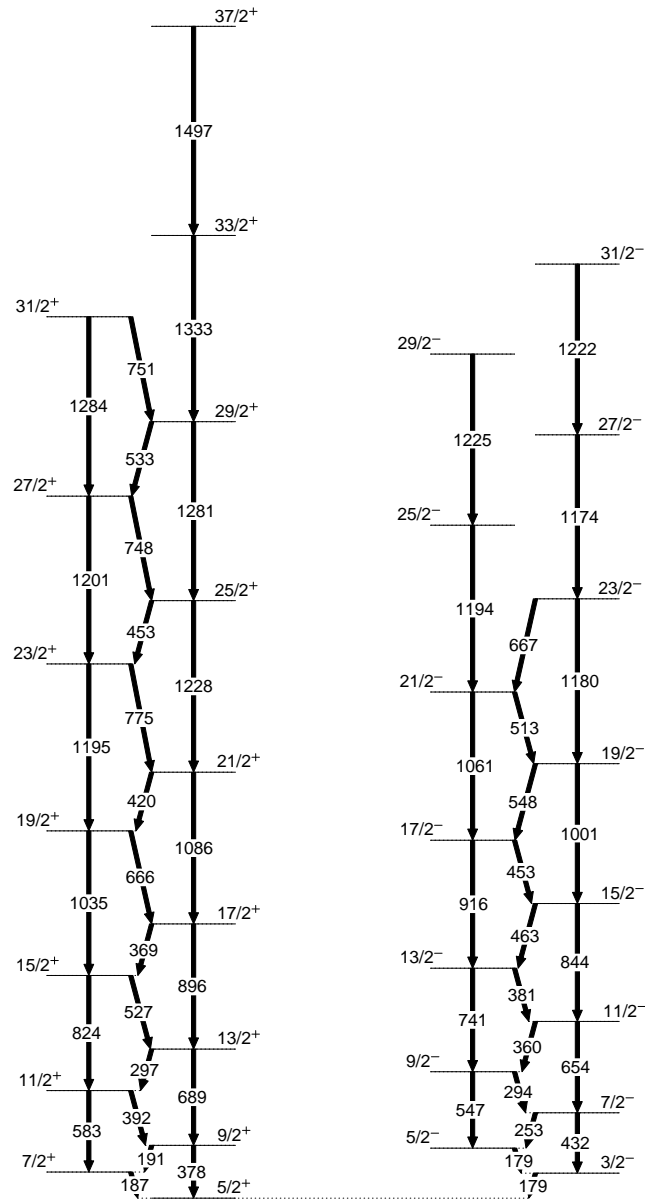
### 5.1 Introduction

As described in chapter 1, atomic nuclei exhibit a rich variety of phenomena primarily due to changes in the shell structure with particle number and excitation energy. The neutron-deficient isotopes with  $A \sim 70 - 80$  in particular have attracted considerable attention because of the observation of large deformation and shape coexistence at low excitation energies [4, 71, 72, 73, 74, 75]. In this mass region, dramatic competition among different shapes occurs because of the oblate deformed shell gaps at  $N$  or  $Z = 34$  and  $36$ , the prolate deformed shell gaps at  $N$  or  $Z = 34$  and  $38$ , and the spherical shell gap at  $N$  or  $Z = 40$  [11]. Several spectroscopic measurements have been carried out to investigate the deformation of these nuclei at various angular momenta. Lifetime measurement by recoil-distance Doppler shift method done by Ljungvall *et al.* [76] in  $^{70}\text{Se}$  and  $^{72}\text{Se}$  confirms the shape isomeric effect in these nuclei. More recently, the Coulomb excitation experiments with radioactive ion beams have been performed to look at the deformations of nuclei at low excitation energies [77]. Nearly symmetric fusion evaporation reactions have been used to study the shape evolution of these weakly populated neutron deficient isotopes up to very high spins [78].

Theoretical investigation of shape coexistence and shape evolution of these isotopes has been pursued quite vigorously using a number of microscopic models and it is

presently an active field of investigation [79, 80, 81, 82]. Previous studies of lifetimes in  $^{77,78}\text{Kr}$  [8, 83] and  $^{80,81}\text{Y}$  [84, 85] show loss of collectivity near the band-crossing region, indicating that the shape changes in each band from prolate at low spin to triaxial above the first rotational alignment. These results are in good agreement with theoretical predictions of models such as the Hartree-Fock-Bogoliubov cranking model and the projected shell model [84]. Another interesting feature of  $N \simeq Z$  nuclei with increasing angular momentum is the loss of collectivity which finally leads to the band termination and is seen, for instance, in  $^{73}\text{Br}$  [9].

In recent years, various structural similarities have also been observed in lighter neutron-deficient even  $Z$  and odd  $N$  nuclei, especially in  $^{73}\text{Se}$  [86],  $^{77}\text{Kr}$  [8], and  $^{77}\text{Sr}$  [87], because of the occupation of valance neutrons in the unique-parity  $g_{9/2}$  orbital. The yrast positive and negative parity bands of these nuclei are based on the  $[422]5/2^+$  and  $[301]3/2^-$  Nilsson orbitals, which is also verified by theoretical calculations. The neutron-deficient Kr isotopes in the vicinity of large shell gap exhibit many fascinating phenomena.  $^{75}\text{Kr}$  nucleus lies between the two well-studied  $^{76}\text{Kr}$  and  $^{74}\text{Kr}$  nuclei, with greatest deformation among all the krypton isotopes. Previous recoil distance lifetime measurements [88, 5] for the low-spin states of both positive and negative parity bands revealed that  $^{75}\text{Kr}$  has a large quadrupole deformation of  $\beta_2 \approx 0.40$ . The purpose of the present work is to understand the evolution nuclear shape with increasing angular momentum in  $^{75}\text{Kr}$  through the measurement of lifetimes of high-spin states. The present work reports the lifetime measurements of 16 states in both the positive and the negative parity bands using the Doppler shift attenuation method (DSAM). These bands exhibit a slight reduction in collectivity after the band crossing. The properties of these bands observed up to high-spins are compared with those obtained using projected shell-model (PSM) [48, 89] calculations. These calculations provide a microscopic understanding of the evolution of the collectivity of the two bands, which confirms the configuration assignments based on the  $g_{9/2}$  and  $f_{7/2}$  neutron orbitals for the observed positive and negative parity bands, respectively, and rotation-alignment effect triggered by the  $g_{9/2}$  protons. This chapter describes the lifetime measurement of high spin states of both positive and negative parity bands in  $^{75}\text{Kr}$ .

Figure 5.1: Partial level scheme of  $^{75}\text{Kr}$  relevant to the present work Ref. [5].

## 5.2 Experimental details

The excited states of the  $^{75}\text{Kr}$  nucleus have been populated via the  $^{50}\text{Cr}(^{28}\text{Si}, 2\text{pn})$  fusion evaporation reaction at an incident beam energy of 90 MeV. The  $^{28}\text{Si}$  beam was delivered by the 15-UD Pelletron accelerator [49] at the Inter University Accelerator Centre (IUAC), New Delhi, India. The target consisted of  $\sim 550 \mu\text{g}/\text{cm}^2$  isotopically enriched 96%  $^{50}\text{Cr}$  with backing of  $\sim 12 \text{mg}/\text{cm}^2$  gold to stop the recoiling ions produced in the reaction. The de-exciting  $\gamma$ -rays were detected with the Indian National Gamma Array (INGA) [22] consisting of 17 Compton-suppressed clover detectors at the time of the experiment. The clover detectors were arranged in five rings at different angle as discussed in Chapter 3. The front face of each detector was positioned  $\sim 24 \text{cm}$  away from the target. The energy and timing information from the clover detectors were processed using the indigenously developed Clover electronics modules [54]. The data were collected in the list mode when two or more detectors fired simultaneously using the CAMAC-based MULTI-CRATE synchronization mode coupled with PC-LINUX environment as described in section 3.5.

To further improve the quality of collected data analysis, we have carried out off-line gain matching of all the 17 clover detectors. The gain matched data were stored off-line into several 4kx4k square matrices with a dispersion of 0.5 keV/channel using the program using the program INGASORT [60]. For the application of Doppler-shift attenuation method (DSAM), line shapes were obtained from the background-subtracted spectra projected from matrices consisting of events in the  $148^\circ$  or  $32^\circ$  detectors along one axis and all other detectors along the second axis. These matrices contained approximately  $3 \times 10^8$  and  $1.5 \times 10^8$  coincidence events, respectively. The transitions reported in Ref. [5] were identified in our experiment also. Partial level scheme of  $^{75}\text{Kr}$  relevant to present work is given in Fig. 5.1 to facilitate the discussion of the line shape results of our measurements. Some representative gated spectra for positive and negative parity bands, indicating the transition observed in the present work are shown in Fig. 5.2 and Fig. 5.3.

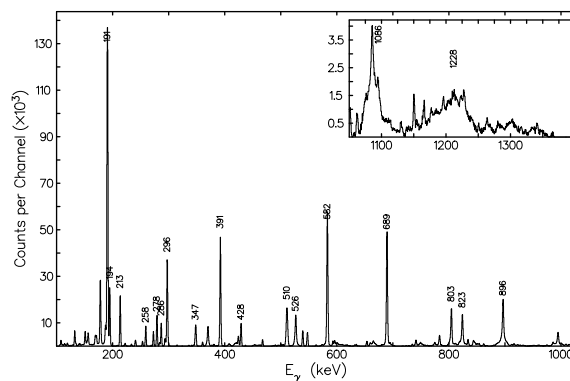


Figure 5.2: Gamma-ray spectrum created by gating on 187 keV transition of the yrast positive-parity band of  $^{75}\text{Kr}$ .

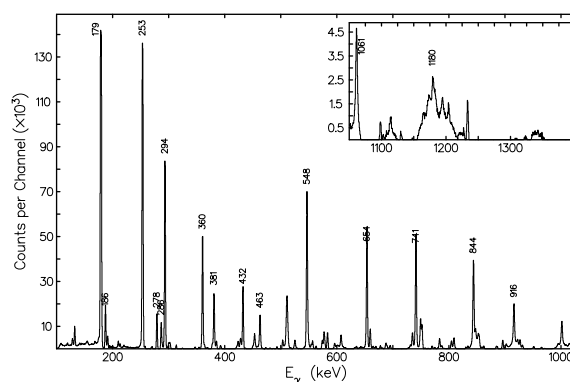


Figure 5.3: Gamma-ray spectrum created by gating on 178 keV transition of the negative-parity band of  $^{75}\text{Kr}$ .

### 5.3 Analysis method

The lifetimes of the states above  $15/2$  for positive-parity bands and  $13/2$  for negative-parity bands were measured for the first time using DSAM technique in the present work. In  $^{75}\text{Kr}$  both positive and negative-parity bands are strongly coupled, and show nearly degenerate signature partners with strong connecting dipole transitions. Therefore, they had to be analyzed as a pair. For analyzing the line shapes of such strongly-coupled bands we have used the program LINESHAPE developed by J. C. Wells [66]. The Monte Carlo simulation technique has been used in this program for the velocity and directional history of a series of recoiling nuclei in the target and in the backing

with a time step of 0.01 ps for 10,000 histories of energy losses at different depths. Shell-corrected Northcliffe and Schilling [70] electronic stopping powers have been used for calculating the energy loss. The detailed fitting procedure is described in section 4.8. The best fit was obtained through the least square minimization procedures SEEK, SIMPLEX, and MIGRAD referred in [66].

In the analysis of both of the bands, an effective lifetime was obtained for the topmost level by assuming a prompt feed to this level; for the rest of the transitions we have used a rotational cascade side-feeding model of five transitions with a fixed moment of inertia of  $20\hbar^2 \text{ MeV}^{-1}$  through out the analysis. The intensities of side-feeding transitions and branching ratio for the positive and negative-parity bands were obtained from experimentally determined relative intensities listed in Ref. [5]. The transition quadrupole moments for the side-feeding bands  $Q_t(\text{SF})$  were found to be  $\sim 2.4(6)$  e b for positive-parity bands and  $\sim 2.0(5)$  e b for the negative-parity bands from fits to the experimental line shapes. The uncertainty involved in the lifetimes and consequently in the transition quadrupole moments ( $Q_t$ ) were determined by the statistical method using subroutine MINOS [90]. The uncertainties of the measured lifetimes do not include those associated with the uncertainties of the stopping powers, which can contribute additional 10-15 % error in transition quadrupole moments.

Most of the line shapes were obtained from coincidence spectra of transition gated from below the transition of interest except for two transition in the negative-parity band where gate from above the transition of interest is used in order to reduce the contamination. Some low-lying transitions in  $^{75}\text{Kr}$  are close to those of other nuclei populated in the same reaction. This makes the selection of proper gate very crucial for the line shape analysis.

For the positive-parity bands, lifetimes were determined by analyzing the Doppler broadened line shapes in  $148^\circ$  and  $32^\circ$  coincidence spectra. The line shapes were obtained by putting the gates on the transition below. The line shapes of most of the transitions in the favored signature of the positive-parity band have been obtained with a gate on the 191- keV transition. However, for the 1228- and 1281-keV transitions the

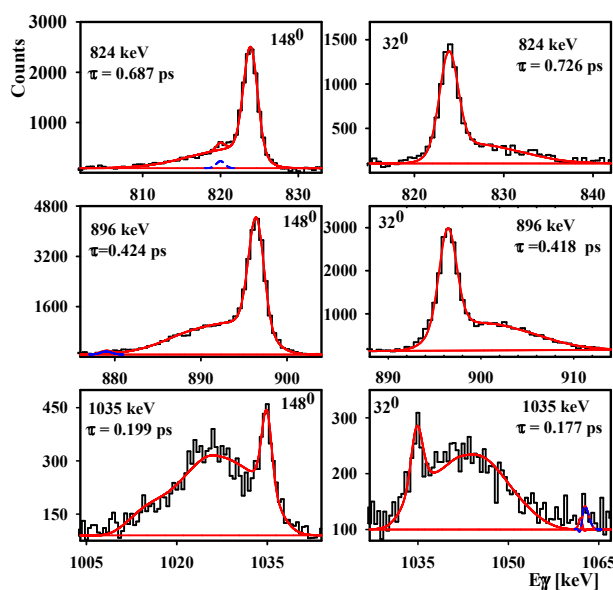


Figure 5.4: Least-squares fits of line shape of some representative transitions in the positive parity bands: 824 keV, 896 keV and 1035 keV transitions. The left-hand frames show the data for the  $148^\circ$  backward detectors and right-hand frames show the data for  $32^\circ$  forward detectors in  $^{75}\text{Kr}$ . The contaminant peaks are shown by dotted lines.

gate on the 896-keV transition has been used to minimize the interference of 1201-keV and 1284-keV transitions present in the unfavored signature band. The line shapes of lower transitions of the unfavored signature band were obtained with a gate on the 392-keV transition. The line shapes of the 1195- and 1201-keV transitions were obtained using a sum gate on 527- and 665-keV transitions and they were fitted together as shown in Fig. 5.5. In order to find the lifetime of levels in coupled band, the effective lifetimes of the state  $33/2^+$  and  $27/2^+$  were obtained through the analysis of the 1333- and 1201-keV transitions. The effective lifetimes were used to determine the lifetimes of the levels down to the  $15/2^+$  state. The experimental and fitted line shapes for some transitions at  $32^\circ$  and  $148^\circ$  are shown in Fig. 5.4.

In negative-parity bands, the lifetimes of  $13/2^-$  and  $15/2^-$  states have been obtained from coincidence spectra gated on transitions above the level of interest in the  $90^\circ$  detectors. This procedure is used to remove the effect of other interband transitions with energies of 741, 844 and 848 keV (as reported in the extensive level scheme of  $^{75}\text{Kr}$  [5]) on the line shapes of the 741 and 844 keV transitions which are emitted

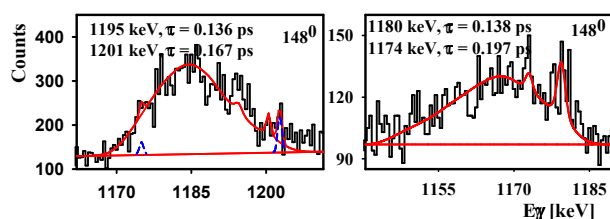


Figure 5.5: Simultaneous line shape fits of some transitions in  $^{75}\text{Kr}$ : The left-hand frame show the simultaneous least square fits of 1195 and 1201 keV transitions at  $148^\circ$  and right-hand frame show simultaneous least square fits of 1180 and 1174 keV transitions at  $148^\circ$ . The contaminant peaks are shown by dotted lines.

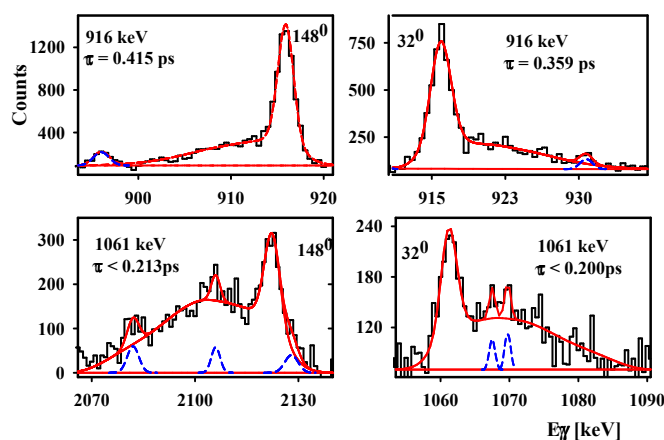


Figure 5.6: Least-squares fits for line shapes of 916 and 1061 keV transitions of the negative-parity band. The left-hand frames show the data for the  $148^\circ$  backward detectors and right-hand frames show the data for  $32^\circ$  forward detectors in  $^{75}\text{Kr}$ . The contaminant peaks are shown by dotted lines.

from  $13/2^-$  and  $15/2^-$  states, respectively. Lifetimes of other states above the  $15/2^-$  were determined by gating below the transition of interest. Effective lifetimes from 1061 keV and 1174 keV transitions have been obtained for the  $21/2^-$  and  $27/2^-$  states. The line shapes of the 1180 and 1174 keV transitions were obtained with gate on the 1001 keV transition. They were fitted together as shown in Fig. 5.5. The experimental and fitted line shapes at  $148^\circ$  and  $32^\circ$  for some transitions of negative-parity band are shown in Fig. 5.6.

The lifetimes of all levels with  $I^\pi=15/2^+$  to  $I^\pi=33/2^+$  in the positive-parity bands and from  $I^\pi=13/2^-$  to  $I^\pi=27/2^-$  levels in the negative-parity bands were obtained from fits to the line shapes at  $32^\circ$  and  $148^\circ$  are listed in Table 5.1 and 5.2, respectively. The

Table 5.1: Experimental lifetimes of excited states in  $^{75}\text{Kr}$  for positive-parity bands. Accepted lifetimes ( $\tau_{acc}$ ) represent the arithmetic average of the results measured at  $148^\circ$  and  $32^\circ$ . Excitation energies ( $E_x$ ),  $\gamma$ -ray energies ( $E_\gamma$ ), branching ratio (Rb) and spins were taken from Ref. [5].

$E_x$ (keV)	$I_f^\pi$ ( $\hbar$ )	$I_i^\pi$ ( $\hbar$ )	$E_\gamma$ (keV)	Rb	previous work (ps)	$\tau_{148}$ (ps)	$\tau_{32}$ (ps)	$\tau_{acc}$ (ps)
1594	15/2 <sup>+</sup>	11/2 <sup>+</sup>	824	62	<0.5	$0.426^{+0.022}_{-0.023}$	$0.450^{+0.022}_{-0.022}$	$0.438^{+0.022}_{-0.023}$
1963	17/2 <sup>+</sup>	13/2 <sup>+</sup>	896	86	<0.9	$0.366^{+0.010}_{-0.030}$	$0.361^{+0.015}_{-0.034}$	$0.364^{+0.015}_{-0.034}$
2629	19/2 <sup>+</sup>	15/2 <sup>+</sup>	1035	73		$0.145^{+0.011}_{-0.015}$	$0.129^{+0.017}_{-0.017}$	$0.137^{+0.017}_{-0.017}$
3049	21/2 <sup>+</sup>	17/2 <sup>+</sup>	1086	94		$0.174^{+0.004}_{-0.018}$	$0.143^{+0.006}_{-0.006}$	$0.159^{+0.006}_{-0.018}$
3824	23/2 <sup>+</sup>	19/2 <sup>+</sup>	1195	80		$0.109^{+0.011}_{-0.015}$	$0.153^{+0.024}_{-0.020}$	$0.131^{+0.024}_{-0.020}$
4277	25/2 <sup>+</sup>	21/2 <sup>+</sup>	1228	95		$0.130^{+0.005}_{-0.006}$	$0.088^{+0.010}_{-0.009}$	$0.109^{+0.010}_{-0.009}$
5025	27/2 <sup>+</sup>	23/2 <sup>+</sup>	1201	65		< 0.109	< 0.079	< 0.094
5558	29/2 <sup>+</sup>	25/2 <sup>+</sup>	1281	100		$0.129^{+0.009}_{-0.010}$	$0.062^{+0.013}_{-0.018}$	$0.096^{+0.013}_{-0.018}$
6891	33/2 <sup>+</sup>	29/2 <sup>+</sup>	1333	100		< 0.099	< 0.109	< 0.104

Table 5.2: Experimental lifetimes of excited states in  $^{75}\text{Kr}$  for the negative-parity bands. Accepted lifetimes ( $\tau_{acc}$ ) represent the arithmetic average of the results measured at  $148^\circ$  and  $32^\circ$ . Excitation energies ( $E_x$ ),  $\gamma$ -ray energies ( $E_\gamma$ ), branching ratio (Rb) and spins were taken from Ref. [5].

$E_x$ (keV)	$I_f^\pi$ ( $\hbar$ )	$I_i^\pi$ ( $\hbar$ )	$E_\gamma$ (keV)	Rb	previous work (ps)	$\tau_{148}$ (ps)	$\tau_{32}$ (ps)	$\tau_{acc}$ (ps)
1646	13/2 <sup>-</sup>	9/2 <sup>-</sup>	741	71	1.0(3)	$0.889^{+0.052}_{-0.049}$		$0.889^{+0.052}_{-0.049}$
2109	15/2 <sup>-</sup>	11/2 <sup>-</sup>	844	81	<0.6	$0.508^{+0.049}_{-0.040}$		$0.508^{+0.049}_{-0.040}$
2562	17/2 <sup>-</sup>	13/2 <sup>-</sup>	916	89		$0.369^{+0.038}_{-0.035}$	$0.320^{+0.033}_{-0.035}$	$0.345^{+0.038}_{-0.035}$
3110	19/2 <sup>-</sup>	15/2 <sup>-</sup>	1001	96		$0.227^{+0.024}_{-0.033}$	$0.243^{+0.019}_{-0.019}$	$0.235^{+0.024}_{-0.033}$
3623	21/2 <sup>-</sup>	17/2 <sup>-</sup>	1061	100		< 0.213	< 0.200	< 0.207
4290	23/2 <sup>-</sup>	19/2 <sup>-</sup>	1180	100		$0.138^{+0.012}_{-0.019}$	$0.178^{+0.038}_{-0.046}$	$0.158^{+0.038}_{-0.046}$
5464	27/2 <sup>-</sup>	23/2 <sup>-</sup>	1174	100		< 0.197	< 0.230	< 0.213

Table 5.3: Reduced transitional probability  $B(E2)$ , transitional quadrupole moments  $Q_t$  for the positive and negative-parity bands in  $^{75}\text{Kr}$  obtained in the present experiment.

$E_x$ (keV)	$I_i^\pi$ ( $\hbar$ )	$I_i^\pi$ ( $\hbar$ )	$E_\gamma$ (keV)	$B(E2)$ (W.u)	$Q_t(\text{Expt})$ (eb)
1594	15/2 <sup>+</sup>	11/2 <sup>+</sup>	824	163 <sup>+9</sup> <sub>-8</sub>	3.53 <sup>+0.10</sup> <sub>-0.08</sub>
1963	17/2 <sup>+</sup>	13/2 <sup>+</sup>	896	179 <sup>+18</sup> <sub>-7</sub>	3.54 <sup>+0.18</sup> <sub>-0.07</sub>
2629	19/2 <sup>+</sup>	15/2 <sup>+</sup>	1035	195 <sup>+27</sup> <sub>-21</sub>	3.59 <sup>+0.24</sup> <sub>-0.20</sub>
3049	21/2 <sup>+</sup>	17/2 <sup>+</sup>	1086	172 <sup>+22</sup> <sub>-5</sub>	3.30 <sup>+0.20</sup> <sub>-0.05</sub>
3824	23/2 <sup>+</sup>	19/2 <sup>+</sup>	1195	109 <sup>+19</sup> <sub>-18</sub>	2.59 <sup>+0.22</sup> <sub>-0.22</sub>
4277	25/2 <sup>+</sup>	21/2 <sup>+</sup>	1128	136 <sup>+13</sup> <sub>-11</sub>	2.85 <sup>+0.13</sup> <sub>-0.12</sub>
5025	27/2 <sup>+</sup>	23/2 <sup>+</sup>	1201	> 121	> 2.67
5558	29/2 <sup>+</sup>	25/2 <sup>+</sup>	1281	132 <sup>+30</sup> <sub>-16</sub>	2.76 <sup>+0.11</sup> <sub>-0.10</sub>
6891	33/2 <sup>+</sup>	29/2 <sup>+</sup>	1333	> 100	> 2.37
1646	13/2 <sup>-</sup>	9/2 <sup>-</sup>	741	156 <sup>+9</sup> <sub>-9</sub>	3.25 <sup>+0.09</sup> <sub>-0.09</sub>
2109	15/2 <sup>-</sup>	11/2 <sup>-</sup>	844	163 <sup>+14</sup> <sub>-15</sub>	3.22 <sup>+0.13</sup> <sub>-0.15</sub>
2562	17/2 <sup>-</sup>	13/2 <sup>-</sup>	916	175 <sup>+22</sup> <sub>-17</sub>	3.27 <sup>+0.20</sup> <sub>-0.17</sub>
3110	19/2 <sup>-</sup>	15/2 <sup>-</sup>	1001	177 <sup>+20</sup> <sub>-16</sub>	3.24 <sup>+0.18</sup> <sub>-0.15</sub>
3623	21/2 <sup>-</sup>	17/2 <sup>-</sup>	1061	> 157	> 3.02
4290	23/2 <sup>-</sup>	19/2 <sup>-</sup>	1180	120 <sup>+38</sup> <sub>-23</sub>	2.63 <sup>+0.39</sup> <sub>-0.27</sub>
5464	27/2 <sup>-</sup>	23/2 <sup>-</sup>	1174	> 92	> 2.26

accepted values obtained from above measurements are listed in the last column. Reduced electric quadrupole transition probability  $B(E2)$  (where, 1 W.u.=18.79 e<sup>2</sup>fm<sup>4</sup>) values obtained from the measured lifetimes are listed in Table 5.3. The transition quadrupole moments values  $Q_t$  were obtained from the  $B(E2)$  values using the rotational formula.

$$Q_t^2 = \frac{16\pi}{5} \langle IK20 | I - 2K \rangle^{-2} B(E2, I \rightarrow I - 2) \quad (5.1)$$

Here  $B(E2)$  is in units of (eb)<sup>2</sup>,  $Q_t$  in e b and the term in brackets is a Clebsch-Gordon coefficient. The value of spin projection quantum number  $K = 5/2$  was used for the positive-parity parity band and  $K = 3/2$  for the negative-parity band, respectively. These  $K$  values are consistent with previously reported Ref. [5], and are found to be the main components of the calculated PSM wave functions (see discussions below). The  $Q_t$  values for the positive and negative-parity bands are also listed in Table 5.3.

## 5.4 Results and Discussion

Energies of excited states,  $\gamma$ -ray transitions and the corresponding lifetimes are summarized in Table 5.1 and 5.2, respectively, for the positive-parity and negative-parity bands. The moment of inertia as a function of spin for both bands (relevant to the present work) are shown in Fig. 5.7 and 5.8. These plots indicates some irregularities around spin  $I = 25/2\hbar$ . The initial gain of  $5\hbar$  in the aligned angular momentum ( $i_x$ ) at  $\hbar\omega = 0.6$  MeV for the positive-parity yrast band which was noticed and interpreted by the cranking model as  $g_{9/2}$  proton alignment in the previous work [5], which gave rise to the irregularities to moment of inertia *vs.* spin plots at the above mentioned spin values. The TRS calculations indicated axially symmetric shapes with large deformation  $\beta_2 = 0.37$  for the positive-parity band and  $\beta_2 = 0.35$  for the negative-parity band [5]. These deformation values are about 10 – 12% lower compared to the experimental values  $\beta_2^{\rho,\text{diff}} = 0.41(2)$  for positive-parity and  $\beta_2^{\rho,\text{diff}} = 0.43(3)$  for negative-parity bands extracted from the measured  $B(E2)$  values for the low-lying states using Woods-

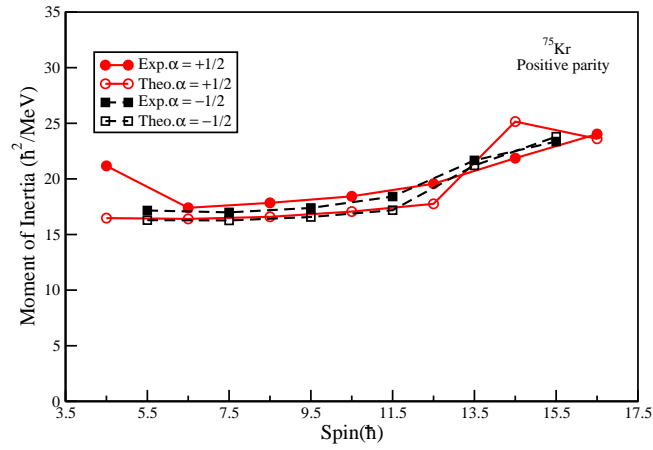


Figure 5.7: Moment of inertia as a function of spin for the positive-parity band in  $^{75}\text{Kr}$ .

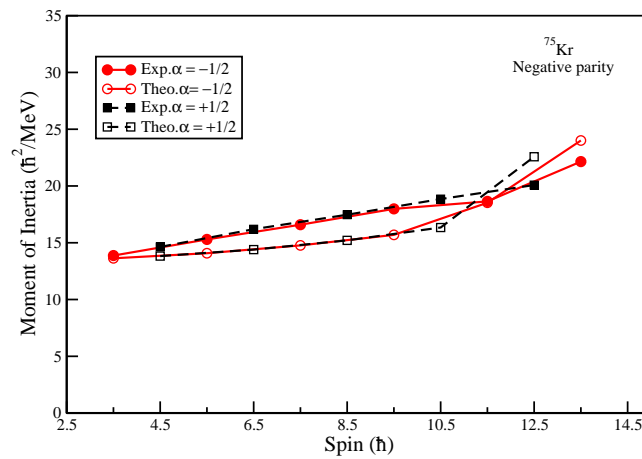


Figure 5.8: Moment of inertia as a function of spin for the negative parity band in  $^{75}\text{Kr}$ .

Saxon potentials [5]. The absolute value of  $\beta_2$  depends on models and the difference in  $\beta_2$  between the microscopic and macroscopic definitions was discussed in ref [91]. It will be interesting to investigate the evolution of deformations at higher spin for these bands. Figures 5.9 and 5.10 show the variation of transition quadrupole moments for positive and negative-parity bands as a function of spin. The behaviors of both the signature partners are almost same in both parity bands (see Ref [92]). It is seen that, the  $B(E2)$  values in both the bands are quite large and values are around 170 W.u. before the band crossing which falling down to around 130 W.u. near the crossing region. Consequently, the average values of transitional quadrupole moments are 3.5 e b and 3.2 e b for positive and negative-parity bands, respectively, before the band crossing. The present work reports the  $Q_t$  measurements beyond the band-crossing region. We observe that near the band crossing region and beyond, the average values of  $Q_t$  decrease for both the bands by around 10 - 20%.

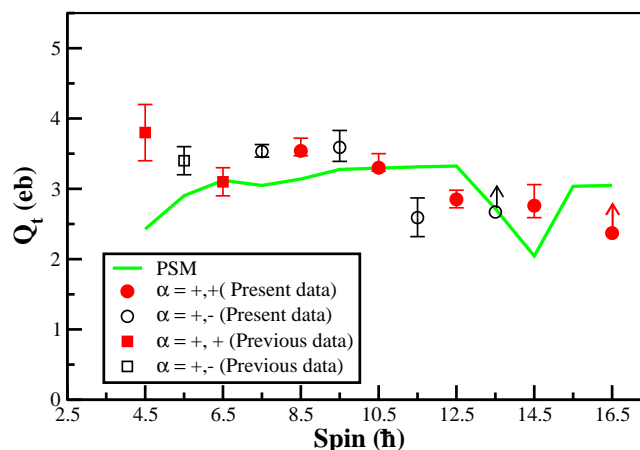


Figure 5.9: Comparison of the measured transitional quadrupole moments  $Q_t$  for excited states in the positive-parity bands in  $^{75}\text{Kr}$  with the prediction of the projected shell-model calculations. Circles represents the data from present measurements and the square for previous work reported in Ref. [5], respectively. Filled (open) symbols stand for positive (negative) signature band.

#### 5.4.1 Projected shell model calculations

The projected shell model (PSM) [48], which is a shell model based on the deformed basis, has been used to understand the evolution of collectivity for the positive and

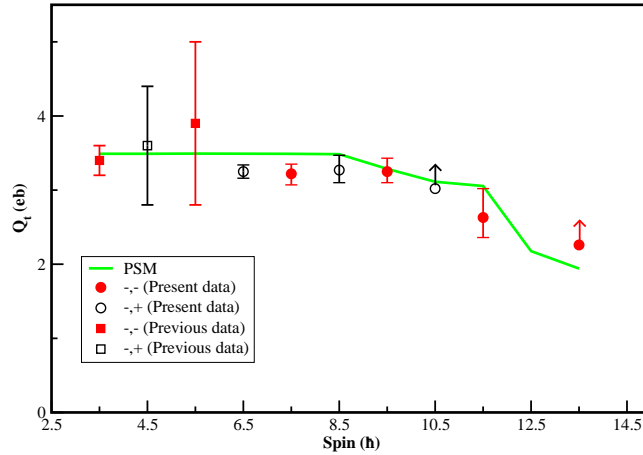


Figure 5.10: Comparison of the measured transitional quadrupole moments  $Q_t$  for excited states in the negative-parity bands in  $^{75}\text{Kr}$  with the prediction of the projected shell-model calculation. Circles represent the data from present measurements and the square for previous work reported in Ref. [5], respectively. Filled (open) symbols stand for positive (negative) signature band.

negative parity bands of  $^{75}\text{Kr}$  up to high spins. It is thus considered highly interesting to examine the behaviors of these  $Q_t$  values for pure oblate or prolate configurations through a model like the PSM. The PSM requires much less numerical effort. Therefore, the calculations are stable and interpretations for its results are easy. In the PSM calculations, we employ a quadrupole plus pairing Hamiltonian, with inclusion of quadrupole-pairing term [48]

$$\hat{H} = \hat{H}_0 - \frac{1}{2}\chi \sum_{\mu} \hat{Q}_{\mu}^{\dagger} \hat{Q}_{\mu} - G_M \hat{P}^{\dagger} \hat{P} - G_Q \sum_{\mu} \hat{P}_{\mu}^{\dagger} \hat{P}_{\mu}. \quad (5.2)$$

In the above equation,  $\hat{H}_0$  is the spherical single-particle Hamiltonian which contains a proper spin-orbit force. The monopole pairing strength  $G_M$  is taken to be  $G_M = [G_1 - G_2(N - Z)/A]/A$  for neutrons and  $G_M = G_1/A$  for protons with  $G_1 = 18.23$  and  $G_2 = 15.12$ . To compare these pairing strengths to those used in the previous PSM calculations for even-even nuclei in the same mass region (see, e.g., Refs. [80, 4]), the pairing strengths employed in this work are reduced by a factor of 0.90 for  $G_1$ , and 0.94 for  $G_2$ , to take into account the weakened pairing in odd-mass systems attributable to the blocking effect. The quadrupole pairing strength  $G_Q$  is assumed as usual to be proportional to  $G_M$ , the proportionality constant being fixed to 0.16 in the present

work. Finally, the quadrupole-quadrupole interaction strength  $\chi$  is determined by the self-consistent relation associated with deformation  $\varepsilon_2$  [48]. As we shall see below,  $\varepsilon_2 = 0.365$  gives the best description for all the experimentally determined states in  $^{75}\text{Kr}$ . This value of deformation is thus used to construct the deformed Nilsson basis, and is consistent with the overall trend of large deformation known for the mass region

## 5.4.2 Comparison with data

The experimental positive and negative parity bands in  $^{75}\text{Kr}$  both show a similar variation in moment of inertia (MI) as spin varies. As shown in Figs. 5.7 and 5.8, a behavior with a moderate increase in MI is seen till  $I \approx 25/2$ , which is followed by a more rapid rise for higher spin states. These experimental MI are compared with the results of the PSM calculations. In Figs. 5.7 and 5.8, MI is defined as  $\mathcal{J}(I) = (2I - 1)/[E(I) - E(I - 2)]$ . As one can see, the measured MI for both signature partners of the positive parity bands show an up bend starting from  $I^\pi = 25/2^+$ , which is well reproduced by the model calculations. The calculation also reasonably well reproduces the variation of moment of inertia with spin for the negative parity band. For the state  $I^\pi = 9/2^+$ , however, our calculations fails to describe the observed large MI value.

Now we turn our discussion to the evolution of transition quadrupole moments as a function of spin. Transition quadrupole moment  $Q_t$  is defined in Eqn. (5.1), in which the  $B(E2)$  values are calculated as

$$B(E2, I \rightarrow I - 2) = \frac{1}{2I + 1} |\langle \psi^{I-2} | \hat{Q}_2 | \psi^I \rangle|^2. \quad (5.3)$$

Constant effective charges are used ( $e_\pi = 1.7e$  for protons and  $e_\nu = 0.7e$  for neutrons); thus any variation in  $B(E2)$  or  $Q_t$  reflects changes of structure of the wave functions. The variation of transitional quadrupole moments with spin for the positive and negative-parity bands are compared with the calculations, in Figs. 5.9 and 5.10, respectively. For completeness, the present measurements of transitional quadrupole moments (see Table 5.3) for spin above  $I^\pi = 15/2^+$  for the positive-parity band and  $I^\pi = 13/2^-$  for the negative-parity band are plotted along with the previous

measurements from Ref. [5]. It is found that the transitional quadrupole moments  $Q_t$  for both positive and negative-parity bands have rather similar values at low spins. At high spins, in particular after the 1-qp and 3-qp band crossing,  $Q_t$  clearly decreases. The decrease in transition quadrupole moments corresponds to a quenching of system deformation. The drop in  $Q_t$  at spins  $I = 27/2$  and  $29/2$  for the positive-parity bands and at  $I = 25/2$  and  $27/2$  for the negative-parity bands is attributed to the changes in the structure (from 1-qp states as main component to 3-qp states). In a theoretical framework with no band mixing, the transitional quadrupole moment will be zero at the band crossing as the transition moment is calculated between two different states. However, due to the band mixing in the PSM, discussed later,  $Q_t$  has a finite values in the band crossing region.

For the lowest spin states of the positive parity the calculated values underpredict the previous measured  $Q_t$  values, as seen in Fig. 5.9. This discrepancy in  $Q_t$  and the failure to reproduce the measured MI at  $I = 9/2^+$  (as seen in Fig. 5.7) may have a common source that can be attributed to our simplified description of the deformed basis. A similar problem was found for the even-even nuclei of the same mass region [80]. In the present PSM calculation for  $^{75}\text{Kr}$ , a fixed prolate deformation is assumed. It is known that this nucleus is characterized by shape changes at low spins [5]. This means that, near the ground state, the potential energy surface has a soft character which cannot be ideally modeled by a single deformation. For the negative-parity band the transitional quadrupole moments ( $Q_t$ ) remain constant up to the band-crossing region, and then reduce slightly by  $\approx 13\%$ . This trend is quite nicely reproduced by the calculated ( $Q_t$ ) values of PSM, as shown in Fig. 5.10.

### 5.4.3 Explanation by configuration mixing

To understand what causes the variations in MI and  $Q_t$  as discussed above, and to further suggest the differences in structure for the rotational bands before and after band crossing, we study the band diagrams in Figs. 5.11 and 5.12, respectively for the positive parity band and negative parity bands. A band diagram in the PSM contains some selected rotational bands in their pure configuration [48]. In this way, it is easy

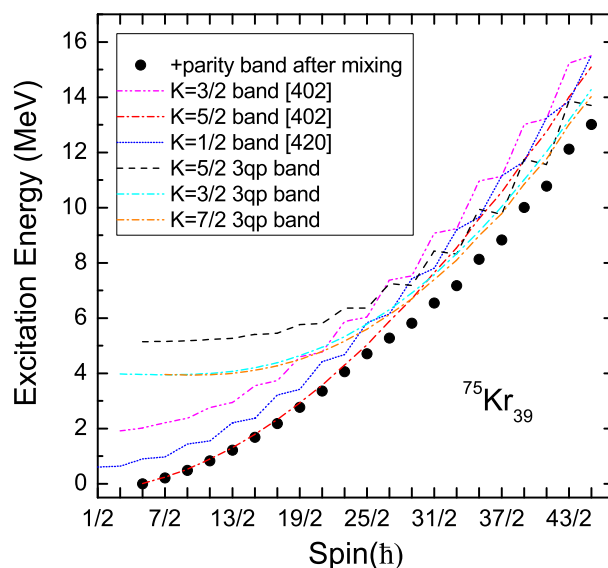
Figure 5.11: Band diagram for the positive parity band in  $^{75}\text{Kr}$ .

Table 5.4: Configurations of 1- and 3-qp states with positive-parity as shown in Fig. 5.11.

parity	qps	total $K$	configurations
+	1-qp	5/2	$\nu$ 5/2[402]
		1/2	$\nu$ 1/2[420]
		3/2	$\nu$ 3/2[402]
+	3-qp	3/2	$\nu$ 5/2[402] $\oplus$ $\pi$ 1/2[400] $\oplus$ $\pi$ 3/2[402]
		7/2	$\nu$ 5/2[402] $\oplus$ $\pi$ 1/2[400] $\oplus$ $\pi$ 3/2[402]
		5/2	$\nu$ 3/2[402] $\oplus$ $\pi$ 1/2[400] $\oplus$ $\pi$ 3/2[402]

to identify the important configurations of interest. The dots shown in Figs. 5.11 and 5.12 represent the lowest states at each spin obtained after band mixing, and these are the theoretical points compared with data (see Figs. 5.7 and 5.8).

For the positive-parity states in Fig. 5.11, we find that the neutron 1-qp band of  $\frac{5}{2}[402]$  lies lowest in energy in the low-spin region whereas the other two, the 1-qp  $\frac{1}{2}[420]$  and  $\frac{3}{2}[402]$  bands, lie respectively, about 0.7 and 1.9 MeV above. Thus the main component in the positive-parity band under discussion should be of  $K = \frac{5}{2}$ . However, the band cannot retain its pure configuration when the nucleus rotates faster because

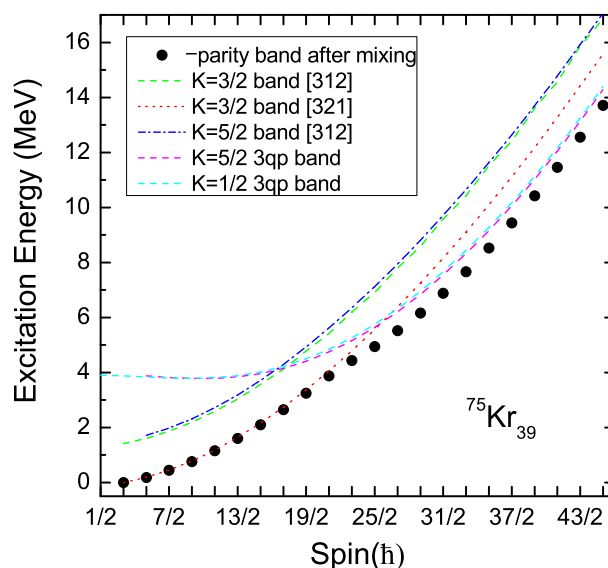
Figure 5.12: Band diagram for the negative parity band in  $^{75}\text{Kr}$ .

Table 5.5: Configurations of 1- and 3-qp states with negative-parity as shown in Fig. 5.12.

parity	qps	total $K$	configurations
-	1-qp	3/2	$\nu$ 3/2[321]
		5/2	$\nu$ 5/2[312]
		3/2	$\nu$ 3/2[312]
-	3-qp	1/2	$\nu$ 3/2[321] $\oplus$ $\pi$ 1/2[400] $\oplus$ $\pi$ 3/2[402]
		5/2	$\nu$ 3/2[321] $\oplus$ $\pi$ 1/2[400] $\oplus$ $\pi$ 3/2[402]

the 3-qp configurations are seen to come down approaching or even crossing the  $K = \frac{5}{2}$  band at higher spins. In Fig. 5.11, we show three most important 3-qp bands which are found the lowest among many other 3-qp bands. Their structures are listed in Table 5.4. Around the region of band-crossing, the corresponding wave functions must undergo a configuration change due to band mixing. The changes in configuration can lead to changes in the measured quantities. In fact, the data have shown a clear increase in MI starting from  $I = 25/2$  (as seen in Fig. 5.7), and reduced  $Q_t$  values near that spin (as seen in Fig. 5.9).

Similar variations discussed above happen also in the negative-parity band. In

the band diagram for the negative-parity states in Fig. 5.12, the lowest band is the neutron 1-qp  $\frac{3}{2}[321]$  band. The other two 1-qp bands, the  $\frac{3}{2}[312]$  and  $\frac{5}{2}[312]$  bands lie about 1.5 MeV above it. At  $I = 25/2$ , the calculation predicts a crossing of the  $\frac{3}{2}[321]$  band by two 3-qp bands (configurations listed in Table 5.5). Due to this crossing, a similar upbend in MI as well as a reduction in  $Q_t$  are expected, as in the positive parity case.

#### 5.4.4 Shape calculations

An other possible interpretation of the observed shape evolution comes from Hartree-Fock-Bogoliubov Cranking model with the Woods-Saxon potential and the monopole pairing force. The calculations generate a total Routhian surface (TRS) plot in the  $(\beta_2, \gamma)$  plane at discrete rotational frequencies, using a deformed Woods-Saxon potential and a short range monopole pairing force.

To investigate the shape of positive and negative parity bands in  $^{75}\text{Kr}$ , we have carried out the theoretical calculations of total Routhian surface (TRS). The evolution of shape and deformation with rotational frequency have been studied previously by Skoda *et al.*, [5] for  $[422]5/2^+$  and  $[301]3/2^-$  configuration of  $^{75}\text{Kr}$  using cranking calculations based on the deformed Woods Saxon potential. Similar calculations have been performed in this work in order to see the evolution of shape after the band crossing. We have performed the TRS calculations at various rotational frequencies for the positive and negative parity bands. In these calculations, the pairing term was calculated by solving the BCS gap equation at rotational frequency  $\omega = 0$  using the interaction strength  $G$  obtained from systematics. The pairing gap  $\Delta$  was allowed to vary smoothly as a linear function of  $\omega$  in such a way that it becomes  $\Delta_0/2$  at the critical frequency  $\omega_c$ , where  $\Delta_0$  is the pair gap at  $\omega = 0$ .  $\hbar\omega_c^\pi = 1.15$  MeV for proton and  $\hbar\omega_c^\nu = 0.95$  MeV for neutron are taken for nuclei in 80 mass region. The TRS were calculated for a range of shape parameters  $\beta_2$  and  $\gamma$  and minimized with respect to the hexadecapole deformation parameter  $\beta_4$ . Fig. 5.13 shows two representative TRS plots for favored signature of the positive-parity yrast band in  $^{75}\text{Kr}$  at two frequencies  $\hbar\omega = 0.30$  and  $0.65$  MeV. For a rotational frequency of  $\hbar\omega = 0.30$  MeV, which lies below

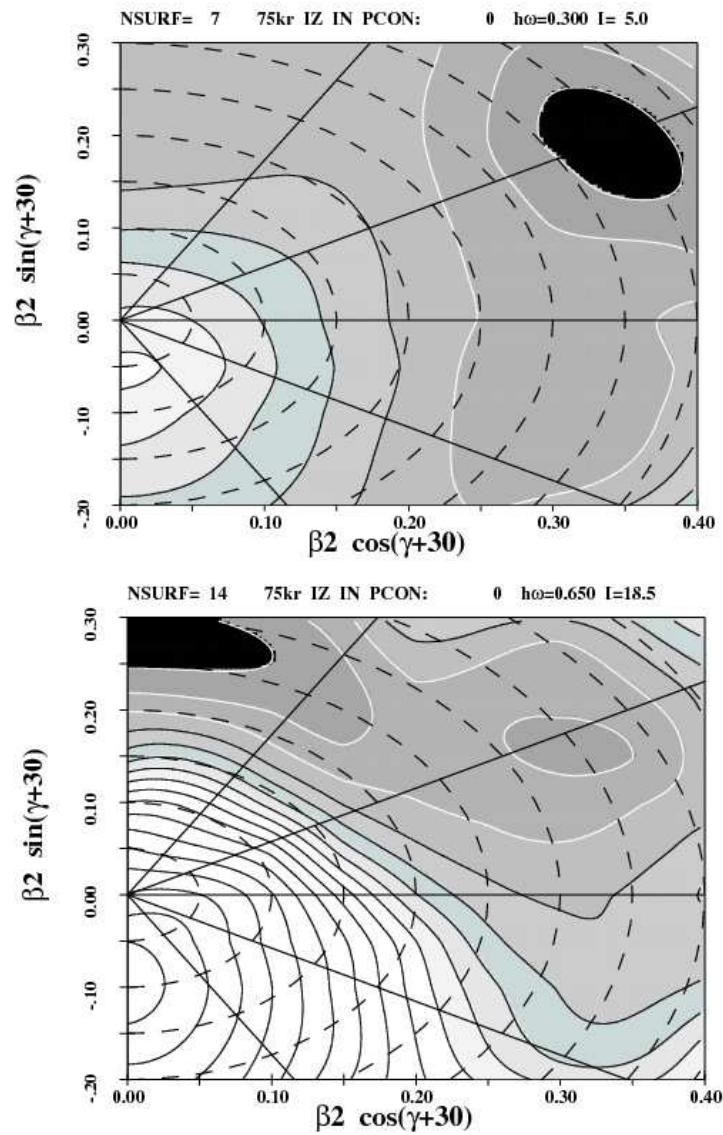


Figure 5.13: Total Routhian Surface (TRS) plots in the  $\beta_2 - \gamma$  plane for positive-parity band of  $^{75}\text{Kr}$ . Plots are for two rotational frequencies,  $\hbar\omega = 0.30$  MeV (top frame) and  $\hbar\omega = 0.65$  MeV (bottom frame) corresponding to before and after band crossing, respectively.

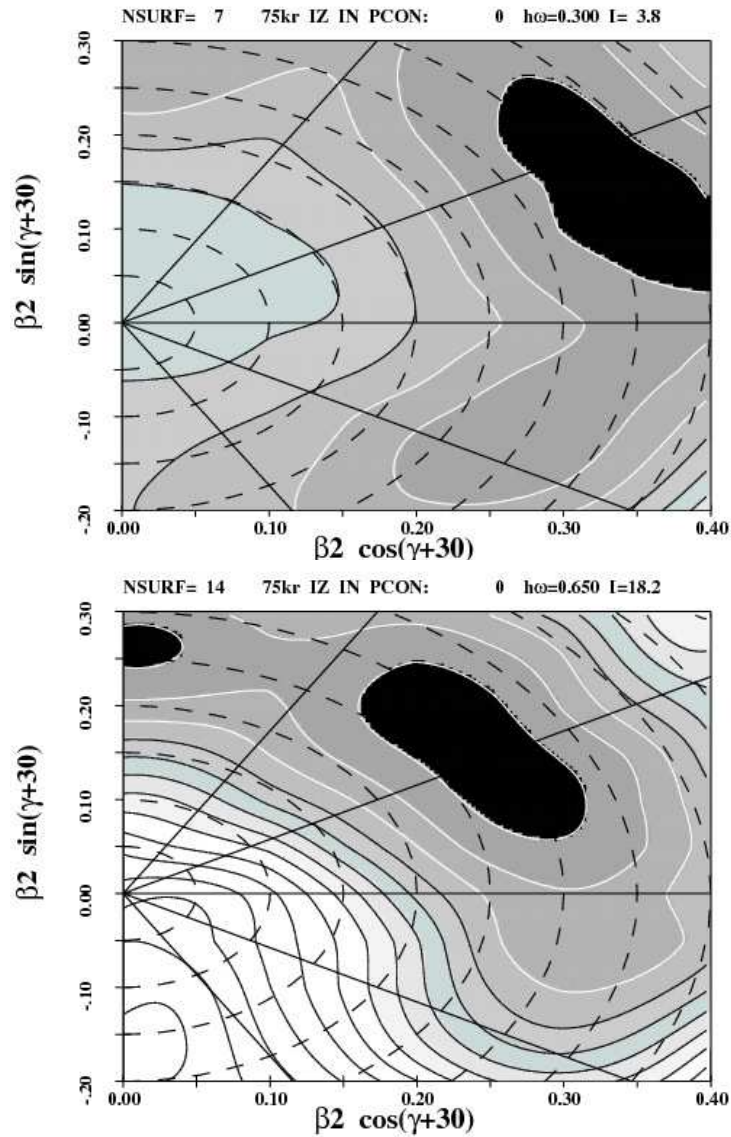


Figure 5.14: Total Routhian Surface (TRS) plots in the  $\beta_2 - \gamma$  plane for negative-parity band of  $^{75}\text{Kr}$ . Plots are for two rotational frequencies,  $\hbar\omega = 0.30$  MeV (top frame) and  $\hbar\omega = 0.65$  MeV (bottom frame) corresponding to before and after band crossing, respectively.

the first band crossing, a nearly prolate shape ( $\gamma \approx -2^\circ$ ) is predicted with deformation  $\beta_2 \approx 0.39$ , in good agreement with the deformation inferred from earlier recoil distance lifetime measurements (RDM). After the first band crossing (i.e after proton alignment) at rotational frequency  $\hbar\omega = 0.65$  MeV, a substantially less deformed prolate shape ( $\beta_2 \approx 0.29$ ) is predicted. At an even higher rotational frequency i.e at  $\hbar\omega = 0.70$  MeV, the shape is still remains nearly prolate with  $\beta_2 \approx 0.28$ . The behavior of TRS plots for unfavored signature partner band generally remain almost similar as observed for favored signature and are not shown.

The TRS calculated for negative-parity band at  $\hbar\omega = 0.30$  MeV and  $\hbar\omega = 0.65$  MeV are shown in Fig. 5.14 (range of spins in which lifetimes were measured in this work). Large deformations nearly  $\beta_2 \approx 0.38$  are indicated near the prolate-deformed axis ( $\gamma = -7^\circ$ ) at  $\hbar\omega = 0.30$  MeV indicating a near-prolate shape which becomes noticeably less deformed after the alignment i.e at  $\hbar\omega = 0.65$  MeV with  $\beta_2 \approx 0.29$  and  $\gamma = 12^\circ$ .

## 5.5 Conclusion

In this chapter, the experimental data of lifetime measurement of high spin states of the yrast positive and negative-parity bands in  $^{75}\text{Kr}$  are discussed and results were interpreted in the framework of projected shell-model and Woods-Saxon cranking calculations. Lifetimes of the high-spin states have been measured using Doppler-shift attenuation method, up to the highest possible spin via  $^{50}\text{Cr}(^{28}\text{Si}, 2\text{pn})^{75}\text{Kr}$  reaction, for the yrast positive-parity, as well as for the negative-parity bands of  $^{75}\text{Kr}$ . The extracted transitional quadrupole moments for both the bands remain constant before the band crossing and then decrease after band crossing. The experimentally observed energies and transition quadrupole moments have been compared with the predictions of projected shell-model and provide a good description of the measured data. The results obtained are also compared with TRS calculations and less deformed nearly prolate shape is predicted after the band crossing. Further measurements of the lifetime of excited states up to higher spins for this nucleus will be useful to probe the

nature of possible band termination.

# Chapter 6

## Shape Evolution at High Spins in $^{75}\text{Br}$

### 6.1 Introduction

The neutron-deficient isotopes with  $A \sim 70 - 80$ , in particular, have drawn considerable attention due to remarkable diversity of shapes and rapid changes in structure with particle number, angular momentum and excitation energies [4, 75, 71, 74, 93, 72]. The  $^{75}\text{Br}$  nucleus lies in the proximity of the  $N = 38$  prolate and the  $N = Z = 34, 36$  oblate shell gaps, implying that nuclei may exhibit different shapes at different excitation energies. The occupation of unique parity  $g_{9/2}$  orbital plays a dominating role for the shape competition and quasi particle alignment with small changes in nucleon number in this mass region. Due to competing collectivity of prolate oblate shapes, neutron-deficient Se [4], Br [94], Kr [5, 92] and with  $N \sim 40$  are well known to exhibit shape coexistence at low, excitation energy. The total Routhian surface (TRS) calculations for these lighter isotopes show more than one minima with small barrier between them. The theoretical investigation of the properties of these isotopes at low and intermediate spins is a challenge for microscopic models [79, 80, 81, 84]. Thus, the study of higher spin states and role of the deformed shall gaps are of vital interest for better understanding of nuclei in this mass region.

Previous experimental study on light odd  $A$  Bromine isotopes,  $^{75}\text{Br}$  and  $^{77}\text{Br}$  by Solomon *et al.* [94] and Sylvan *et al.* [95] have predicted two distinct rotational bands,

the ground state band having properties consistent with collective prolate rotational and excited band with high K oblate deformation. Previous recoil distance lifetime measurements [96] for the low-spin states of both positive as well as negative-parity bands revealed that  $^{75}\text{Br}$  has large quadrupole deformation  $\beta_2 \approx 0.3$ . So far yrast sequence of favored signature of positive and negative-parity band and few low lying states of unfavored states have been studied by Luhmann *et al.*, [96] and Mukherjee *et al.*, [97] by using thick 78 mg/cm<sup>2</sup> thick Vanadium target and fewer number of detectors. The present work reports the complementary measurement of lifetimes of 32 states with high efficiency detector array and with thin target above the band crossing, upto state  $37/2^+$  in the yrast positive-parity band,  $39/2^-$  in the negative-parity bands, and state upto  $25/2^+$  and  $31/2^-$  for high lying positive and negative-parity bands, respectively using Doppler shift attenuation method (DSAM). Lifetimes reported in this work, represents some recent measurements carried out with better accuracy which also include some previous measurements performed by Luhmann *et al.* [96] and Mukherjee *et al.* [97]. In addition, lifetime of states lying in high K bands are also reported for the first time in the present work. The motivation for the present work is to investigate the collectivity of different bands by measuring the lifetimes of high spin states of  $^{75}\text{Br}$  by DSAM technique. The properties of these bands observed up to high spins are compared with the projected shell model (PSM) [48, 89] calculations as well as cranked shell model.

## 6.2 Experimental details

High spin states of  $^{75}\text{Br}$  nucleus have been populated via the  $^{50}\text{Cr}(^{28}\text{Si}, 3p)$  fusion evaporation reaction at an incident beam energy of 90 MeV, this being another strongly populated channel in the same experiment discussed in Chapter 5. The details of target and detector system was already discussed in section 5.2 of previous chapter. The average initial recoil velocity of  $^{75}\text{Br}$  nuclei was  $\beta \approx 0.025$ .

For the application of Doppler-shift attenuation method (DSAM), various asymmetric matrices were constructed and line shapes were obtained from the background-

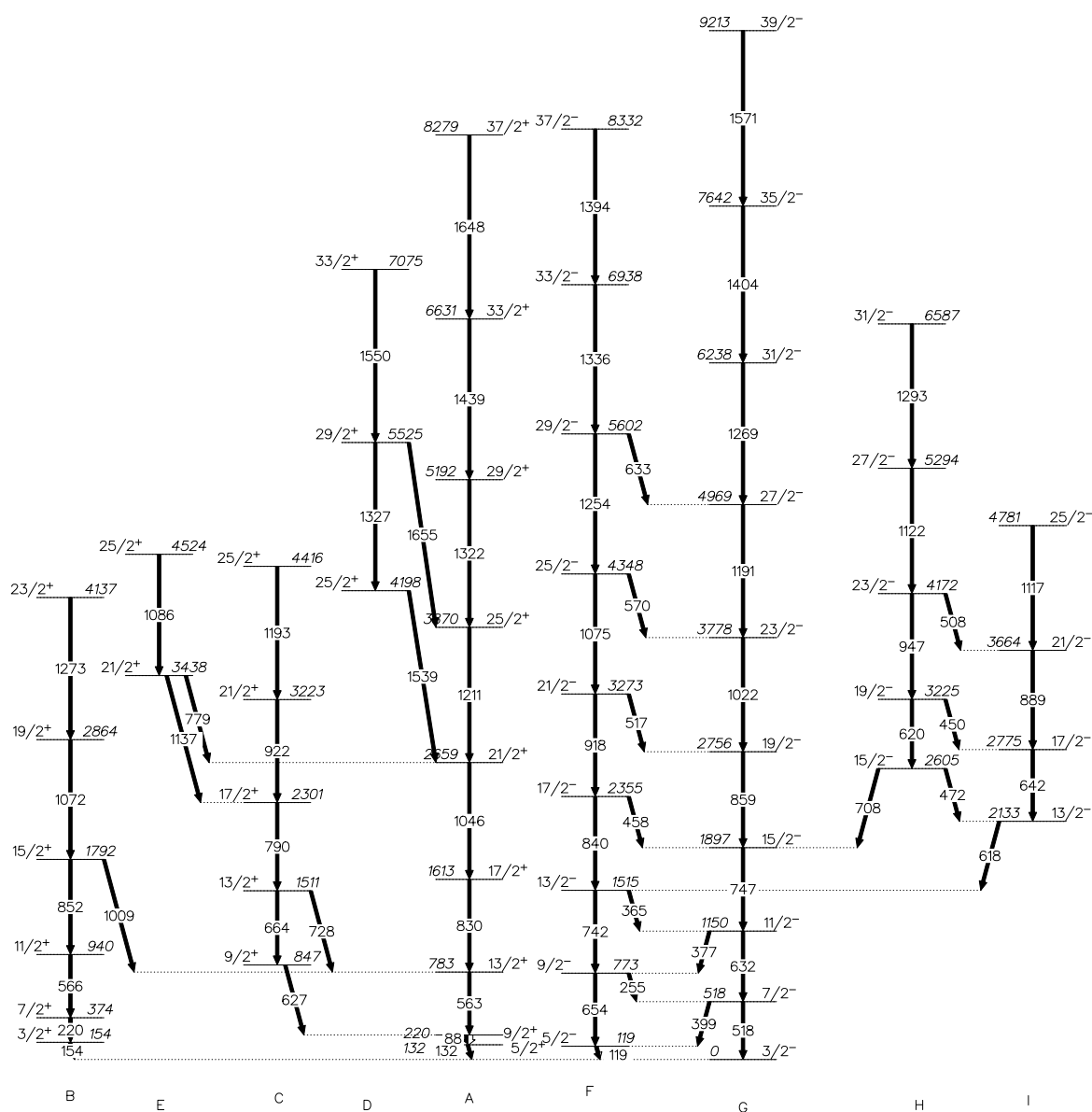


Figure 6.1: Partial level scheme of  $^{75}\text{Br}$  relevant to the present work Ref. [94].

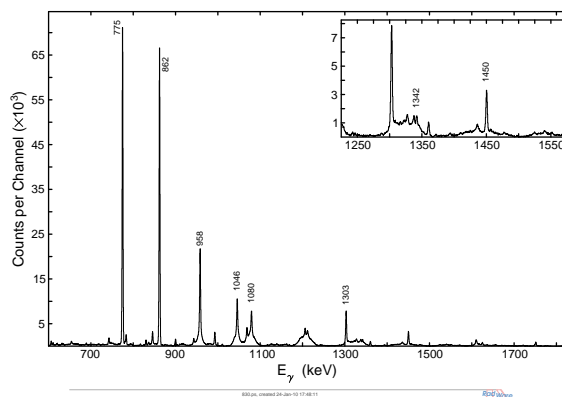


Figure 6.2: Gamma-ray spectrum created by gating on 830 keV transition of the yrast positive-parity band of  $^{75}\text{Br}$ .

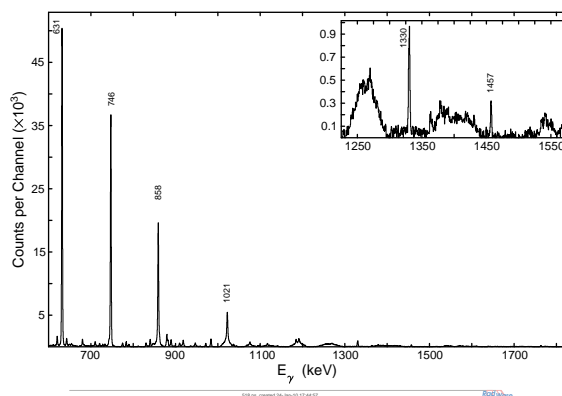


Figure 6.3: Gamma-ray spectrum created by gating on 518 keV transition of the favored signature partner of negative-parity band in  $^{75}\text{Br}$ .

subtracted spectra projected from matrices consisting of events at  $148^\circ$  ( $32^\circ$ ) detectors at one axis and all other detectors at second axis. Whereas, in case where lifetimes were obtained from gating above the transition asymmetric matrices consisting events at  $148^\circ$  ( $32^\circ$ ) detectors at one axis and all  $90^\circ$  detectors were put at second axis. Partial level scheme of  $^{75}\text{Br}$  relevant to present work is given in Fig. 6.1 to enable the discussion of the results of our measurement on line shapes. The transition reported in Ref. [94] were identified in our experiment, too. Some representative gated spectra for different bands indicating the transition observed in the present work are shown in Figs. 6.2, 6.3 and 6.4

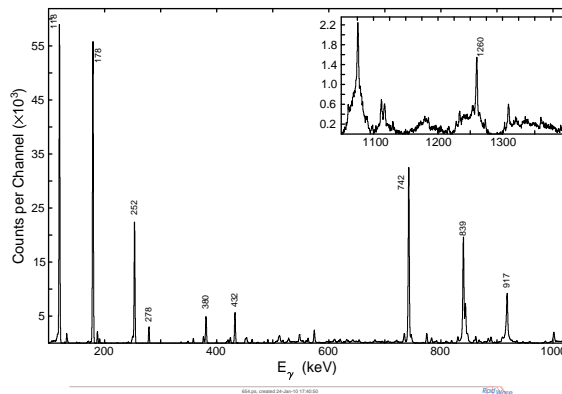


Figure 6.4: Gamma-ray spectrum created by gating on 654 keV transition of the unfavored signature partner of negative-parity band in  $^{75}\text{Br}$ .

### 6.3 Analysis method

The sub-picosecond lifetimes of the states above  $15/2$  were measured using DSAM technique in the present work. For analyzing the Doppler-broadened line shapes we have used the program LINESHAPE developed by J. C. Wells [66] already discussed in previous section 4.8. In the analysis of Doppler-broadened line shapes, an effective lifetime was obtained for the top most level by assuming a prompt feed to this level and for the rest of the transitions we have used a rotational cascade side-feeding model of five transitions. The intensities of side feeding transitions of the positive and negative-parity bands were obtained from experimentally determined relative intensities quoted in Ref. [94], from the intensity balance of each state. The uncertainty involved in the lifetimes and consequently in the transition quadrupole moments, ( $Q_t$ ) were determined by the statistical method using subroutine MINOS [90]. The uncertainties of the measured lifetimes have included 10% errors associated with the uncertainties of the stopping powers [70].

The line shapes were obtained from coincidence spectra of transition gated from below the transition of interest and lifetimes were obtained by analyzing the Doppler broadened line-shapes in  $32^\circ$  and  $148^\circ$  coincidence spectra, except in case of high K bands where only backward spectra were used. Lifetimes of some low lying states whenever possible, were determined from spectra gated from above the transition of

interest, to eliminate the effect of side feeding and it was found that lifetime values are almost consistent with this method of analysis of Doppler-broadened line shapes, too. As shown in decay scheme (see Fig. 6.1), for favored signature band A, 1322-keV transition is contaminated by 1327-keV transition of high lying band D. Thus line shape of 1322-keV transition is obtained by putting gate on 1211-keV transition to reduce the interference of this transition and hence we have obtained the Doppler-broadened line shapes by coincidence spectra gated on lines in  $90^\circ$  detectors and other detectors at  $148^\circ$  or ( $32^\circ$ ) and all other are fitted by 563 keV gate. The lifetimes of the states up to  $37/2^+$  were measured in the positive-parity band. However, in case of negative-parity band lifetimes up to  $39/2^-$  state have been measured. In addition, lifetimes of high K bands are also measured using gating below technique up to highest possible spin. In order to find the lifetimes of different bands, an effective lifetime has been determined for the top state and with this effective lifetime we have proceeded down to determine the lifetimes of lower states what so ever is possible by this technique. In some cases line-shape analysis became complicated due to the fact some low lying transitions in  $^{75}\text{Br}$  are very close to those of other nuclei populating in the same reaction as can be seen in Figs. 6.3. This makes the selection of proper gates more important to reduce the contamination in the line shapes of other transitions. The lifetime for the highest state in each cascade served as an upper bound value.

The experimental and fitted line-shapes for some representative transitions of different bands of  $^{75}\text{Br}$  at  $32^\circ$  and  $148^\circ$  are shown in Fig. 6.5, Fig. 6.6 and Fig. 6.7.

The lifetimes of all levels with  $I^\pi=15/2^+$  to  $I^\pi=37/2^+$  in the positive-parity bands and from  $15/2^-$  to  $39/2^-$  levels in the negative-parity bands obtained from fits to the line shapes at  $32^\circ$  and  $148^\circ$  are listed in Table 6.1 - 6.2, respectively. The accepted value of lifetimes have been obtained from weighted average and are listed in the last column of Table 6.1 - 6.2, respectively. Once lifetimes have been determined, reduced electric quadrupole transition probabilities  $B(E2)$  were obtained from the accepted values of lifetimes and hence the transition quadrupole moments  $Q_t$  were calculated using Eq. 5.1. The value of spin projection quantum number  $K = 1/2$  were used for the yrast positive parity band and  $K = 3/2$  for the yrast negative parity band, where as

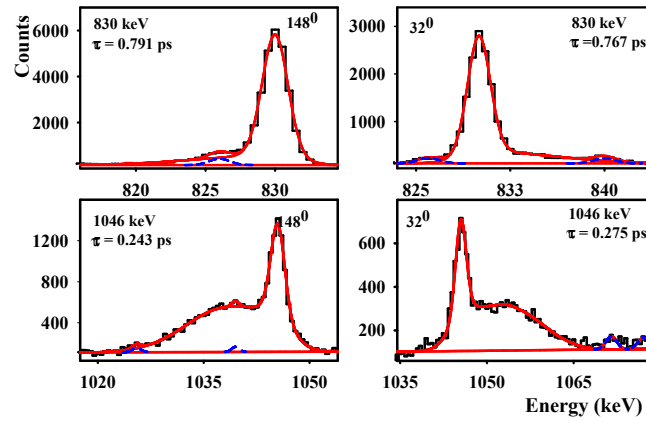


Figure 6.5: Least squares fits for line shape of 830 keV and 1046 keV transitions of the positive parity band. The left-hand frames show the data for the  $148^0$  backward detectors and right-hand frame show the data for  $32^0$  forward detectors in  $^{75}\text{Br}$ . The contaminant peaks are shown by dotted line.

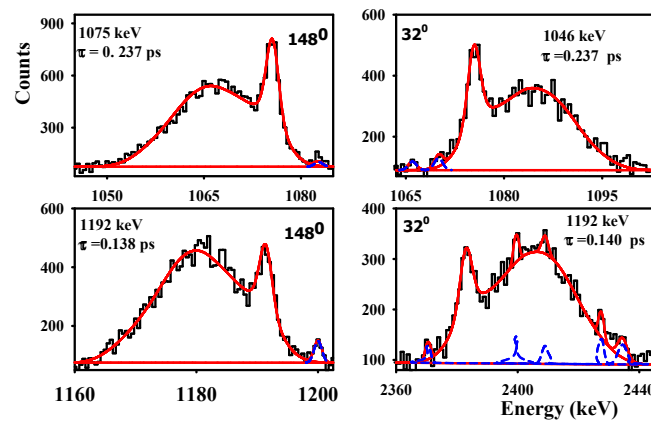


Figure 6.6: Least-squares fits for line shape of 1075 keV and 1192 keV transitions of negative parity band. The left-hand frames show the data for the  $148^0$  backward detectors and right-hand frames show the data for  $32^0$  forward detectors in  $^{75}\text{Br}$ . The contaminant peaks are shown by dotted line.

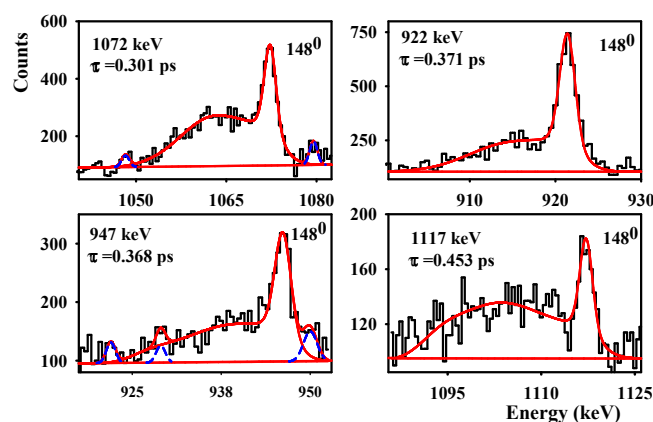


Figure 6.7: Least-squares fits for line shape of some representative transitions of different bands: 1072 keV, 922 keV, 947 keV and 1117 keV transitions for the  $148^0$  backward detectors in  $^{75}\text{Br}$ . The contaminant peaks are shown by dotted line.

Table 6.1: Experimental lifetimes of excited states in  $^{75}\text{Br}$  for positive-parity bands. Accepted lifetimes ( $\tau_{acc}$ ) represent the weighted average of the results measured at  $148^\circ$  and  $32^\circ$ . Excitation energies ( $E_x$ ),  $\gamma$ -ray energies ( $E_\gamma$ ), and spins were taken from Ref. [94].

$E_x$ (keV)	$I_i^\pi$ ( $\hbar$ )	$I_i^\pi$ ( $\hbar$ )	$E_\gamma$ (keV)	previous work (ps) <sup>b</sup>	$\tau_{148}$ (ps)	$\tau_{32}$ (ps)	$\tau_{acc}$ (ps)
1613	17/2 <sup>+</sup>	13/2 <sup>+</sup>	830	1.12 <sup>+0.16</sup> <sub>-0.22</sub>	0.791 <sup>+0.192</sup> <sub>-0.141</sub>	0.767 <sup>+0.195</sup> <sub>-0.144</sub>	0.780 <sup>+0.130</sup> <sub>-0.101</sub>
1791	15/2 <sup>+</sup>	11/2 <sup>+</sup>	852	1.08 <sup>+0.20</sup> <sub>-0.21</sub>	0.771 <sup>+0.221</sup> <sub>-0.166</sub>		0.771 <sup>+0.221</sup> <sub>-0.166</sub>
2658	21/2 <sup>+</sup>	17/2 <sup>+</sup>	1046	0.41 <sup>+0.09</sup> <sub>-0.08</sub>	0.243 <sup>+0.064</sup> <sub>-0.043</sub>	0.275 <sup>+0.066</sup> <sub>-0.048</sub>	0.260 <sup>+0.044</sup> <sub>-0.034</sub>
2863	19/2 <sup>+</sup>	15/2 <sup>+</sup>	1072	0.47 <sup>+0.05</sup> <sub>-0.05</sub>	0.301 <sup>+0.075</sup> <sub>-0.055</sub>		0.301 <sup>+0.075</sup> <sub>-0.055</sub>
3589	25/2 <sup>+</sup>	21/2 <sup>+</sup>	1211	0.14 <sup>+0.03</sup> <sub>-0.03</sub>	0.166 <sup>+0.040</sup> <sub>-0.030</sub>	0.162 <sup>+0.044</sup> <sub>-0.033</sub>	0.164 <sup>+0.028</sup> <sub>-0.023</sub>
4136	23/2 <sup>+</sup>	19/2 <sup>+</sup>	1273		< 0.187		< 0.187
5191	29/2 <sup>+</sup>	25/2 <sup>+</sup>	1322	0.17 <sup>+0.04</sup> <sub>-0.03</sub>	0.162 <sup>+0.040</sup> <sub>-0.030</sub>	0.128 <sup>+0.035</sup> <sub>-0.025</sub>	0.147 <sup>+0.026</sup> <sub>-0.021</sub>
6630	33/2 <sup>+</sup>	29/2 <sup>+</sup>	1439	0.08 <sup>+0.02</sup> <sub>-0.02</sub>	0.101 <sup>+0.028</sup> <sub>-0.022</sub>	< 0.12	0.101 <sup>+0.028</sup> <sub>-0.022</sub>
8277	37/2 <sup>+</sup>	33/2 <sup>+</sup>	1648	0.03 <sup>+0.01</sup> <sub>-0.008</sub>	< 0.048		< 0.048

Table 6.2: Experimental lifetimes of excited states in  $^{75}\text{Br}$  for the negative-parity bands. Accepted lifetimes ( $\tau_{acc}$ ) represent the weighted average of the results measured at  $148^\circ$  and  $32^\circ$ . Excitation energies ( $E_x$ ),  $\gamma$ -ray energies ( $E_\gamma$ ), and spins were taken from Ref. [94].  $a$  and  $b$  represents data from Ref. [96] and [97], respectively.

$E_x$ (keV)	$I_i^\pi$ ( $\hbar$ )	$I_i^\pi$ ( $\hbar$ )	$E_\gamma$ (keV)	previous work (ps)	$\tau_{148}$ (ps)	$\tau_{32}$ (ps)	$\tau_{acc}$ (ps)
1896	$15/2^-$	$11/2^-$	747	$1.8(9)^a$	$1.334^{+0.347}_{-0.268}$	$1.267^{+0.338}_{-0.253}$	$1.301^{+0.232}_{-0.191}$
2355	$17/2^-$	$13/2^-$	840	$1.16^{+0.26b}_{-0.22}$		$0.838^{+0.204}_{-0.157}$	$0.838^{+0.204}_{-0.157}$
2755	$19/2^-$	$15/2^-$	859	$1.2(3)^a$	$0.526^{+0.130}_{-0.101}$	$0.519^{+0.166}_{-0.121}$	$0.523^{+0.098}_{-0.080}$
3273	$21/2^-$	$17/2^-$	918	$0.70^{+0.16b}_{-0.14}$	$0.490^{+0.116}_{-0.088}$	$0.491^{+0.118}_{-0.088}$	$0.490^{+0.079}_{-0.065}$
3777	$23/2^-$	$19/2^-$	1022	$0.54(11)^a$	$0.312^{+0.073}_{-0.054}$	$0.260^{+0.062}_{-0.047}$	$0.287^{+0.045}_{-0.037}$
4348	$25/2^-$	$21/2^-$	1075	$0.30^{+0.07b}_{-0.06}$	$0.237^{+0.056}_{-0.041}$	$0.237^{+0.056}_{-0.042}$	$0.237^{+0.038}_{-0.030}$
4968	$27/2^-$	$23/2^-$	1191	$0.26(5)^a$	$0.138^{+0.037}_{-0.024}$	$0.140^{+0.034}_{-0.026}$	$0.139^{+0.024}_{-0.019}$
5603	$29/2^-$	$25/2^-$	1254	$0.18^{+0.05b}_{-0.04}$	$0.115^{+0.028}_{-0.021}$	$0.072^{+0.020}_{-0.014}$	$0.097^{+0.018}_{-0.014}$
6237	$31/2^-$	$27/2^-$	1269		$0.180^{+0.043}_{-0.032}$	$0.158^{+0.039}_{-0.029}$	$0.169^{+0.028}_{-0.022}$
6939	$33/2^-$	$29/2^-$	1336	$0.09^{+0.03b}_{-0.02}$	$0.108^{+0.029}_{-0.020}$	$0.118^{+0.030}_{-0.022}$	$0.113^{+0.02}_{-0.016}$
7641	$35/2^-$	$31/2^-$	1404		$< 0.107$	$0.135^{+0.033}_{-0.025}$	$0.135^{+0.033}_{-0.025}$
8333	$37/2^-$	$33/2^-$	1394	$0.03^{+0.01b}_{-0.01}$	$< 0.095$	$< 0.163$	$< 0.132$
9212	$39/2^-$	$35/2^-$	1571			$< 0.158$	$< 0.158$

Table 6.3: Experimental lifetimes of excited states in  $^{75}\text{Br}$  measured at  $148^\circ$  for the positive-parity high lying K bands. Excitation energies ( $E_x$ ),  $\gamma$ -ray energies ( $E_\gamma$ ), and spins were taken from Ref. [94].

$E_x$ (keV)	$I_i^\pi$ ( $\hbar$ )	$I_i^\pi$ ( $\hbar$ )	$E_\gamma$ (keV)	$\tau_{acc}$ (ps)
2310	$17/2^+$	$13/2^+$	790	$0.835^{+0.154}_{-0.125}$
3223	$21/2^+$	$17/2^+$	922	$0.373^{+0.050}_{-0.062}$
4416	$25/2^+$	$21/2^+$	1193	$< 0.308$
3438	$21/2^+$	$17/2^+$	1137	$0.389^{+0.102}_{-0.074}$
4525	$25/2^+$	$21/2^+$	1086	$< 0.200$

Table 6.4: Experimental lifetimes of excited states in  $^{75}\text{Br}$  measured at  $148^\circ$  for the negative-parity high lying K bands. Excitation energies ( $E_x$ ),  $\gamma$ -ray energies ( $E_\gamma$ ), and spins were taken from Ref. [94].

$E_x$ (keV)	$I_i^\pi$ ( $\hbar$ )	$I_i^\pi$ ( $\hbar$ )	$E_\gamma$ (keV)	$\tau_{acc}$ (ps)
4170	23/2 <sup>-</sup>	19/2 <sup>-</sup>	947	0.368 <sup>+0.094</sup> <sub>-0.069</sub>
5293	27/2 <sup>-</sup>	23/2 <sup>-</sup>	1122	0.154 <sup>+0.044</sup> <sub>-0.035</sub>
6586	31/2 <sup>-</sup>	27/2 <sup>-</sup>	1293	< 0.233
3664	21/2 <sup>-</sup>	17/2 <sup>-</sup>	889	0.505 <sup>+0.102</sup> <sub>-0.074</sub>
4781	25/2 <sup>-</sup>	21/2 <sup>-</sup>	1117	< 0.454

Table 6.5: Reduced transitional probability  $B(E2)$ , transitional quadrupole moments  $Q_t$  for the positive and negative-parity bands in  $^{75}\text{Br}$  obtained from present experiment.

$E_x$ (keV)	$I_i^\pi$ ( $\hbar$ )	$I_i^\pi$ ( $\hbar$ )	$E_\gamma$ (keV)	$B(E2)$ (W.u)	$Q_t(\text{Expt})$ (eb)
1613	17/2 <sup>+</sup>	13/2 <sup>+</sup>	830	142 <sup>+22</sup> <sub>-20</sub>	2.85 <sup>+0.21</sup> <sub>-0.21</sub>
1791	15/2 <sup>+</sup>	11/2 <sup>+</sup>	852	126 <sup>+35</sup> <sub>-27</sub>	2.72 <sup>+0.35</sup> <sub>-0.32</sub>
2658	21/2 <sup>+</sup>	17/2 <sup>+</sup>	1046	134 <sup>+20</sup> <sub>-19</sub>	2.74 <sup>+0.20</sup> <sub>-0.21</sub>
2863	19/2 <sup>+</sup>	15/2 <sup>+</sup>	1072	102 <sup>+23</sup> <sub>-20</sub>	2.41 <sup>+0.26</sup> <sub>-0.25</sub>
3589	25/2 <sup>+</sup>	21/2 <sup>+</sup>	1211	102 <sup>+16</sup> <sub>-15</sub>	2.37 <sup>+0.19</sup> <sub>-0.18</sub>
4136	23/2 <sup>+</sup>	19/2 <sup>+</sup>	1273	> 69	> 1.96
5191	29/2 <sup>+</sup>	25/2 <sup>+</sup>	1322	73 <sup>+13</sup> <sub>-11</sub>	2.00 <sup>+0.16</sup> <sub>-0.16</sub>
6630	33/2 <sup>+</sup>	29/2 <sup>+</sup>	1439	70 <sup>+19</sup> <sub>-15</sub>	1.94 <sup>+0.25</sup> <sub>-0.22</sub>
8277	37/2 <sup>+</sup>	33/2 <sup>+</sup>	1648	> 75	> 2.00
1896	15/2 <sup>-</sup>	11/2 <sup>-</sup>	747	144 <sup>+25</sup> <sub>-22</sub>	3.03 <sup>+0.25</sup> <sub>-0.24</sub>
2355	17/2 <sup>-</sup>	13/2 <sup>-</sup>	840	125 <sup>+27</sup> <sub>-24</sub>	2.76 <sup>+0.29</sup> <sub>-0.28</sub>
2755	19/2 <sup>-</sup>	15/2 <sup>-</sup>	859	178 <sup>+32</sup> <sub>-28</sub>	3.26 <sup>+0.28</sup> <sub>-0.27</sub>
3273	21/2 <sup>-</sup>	17/2 <sup>-</sup>	918	137 <sup>+21</sup> <sub>-19</sub>	2.82 <sup>+0.21</sup> <sub>-0.20</sub>
3777	23/2 <sup>+</sup>	19/2 <sup>+</sup>	1022	136 <sup>+20</sup> <sub>-18</sub>	2.80 <sup>+0.20</sup> <sub>-0.20</sub>
4348	25/2 <sup>-</sup>	21/2 <sup>-</sup>	1075	128 <sup>+19</sup> <sub>-18</sub>	2.69 <sup>+0.19</sup> <sub>-0.19</sub>
4968	27/2 <sup>-</sup>	23/2 <sup>-</sup>	1191	131 <sup>+21</sup> <sub>-19</sub>	2.70 <sup>+0.21</sup> <sub>-0.21</sub>
5603	29/2 <sup>-</sup>	25/2 <sup>-</sup>	1254	145 <sup>+24</sup> <sub>-23</sub>	2.83 <sup>+0.23</sup> <sub>-0.23</sub>
6237	31/2 <sup>-</sup>	27/2 <sup>-</sup>	1269	78 <sup>+12</sup> <sub>-11</sub>	2.08 <sup>+0.15</sup> <sub>-0.15</sub>
6939	33/2 <sup>-</sup>	29/2 <sup>-</sup>	1336	90 <sup>+15</sup> <sub>-14</sub>	2.22 <sup>+0.18</sup> <sub>-0.17</sub>
7641	35/2 <sup>-</sup>	31/2 <sup>-</sup>	1404	59 <sup>+13</sup> <sub>-12</sub>	1.79 <sup>+0.19</sup> <sub>-0.19</sub>
8333	37/2 <sup>-</sup>	33/2 <sup>-</sup>	1394	> 63	> 1.84
9212	39/2 <sup>-</sup>	35/2 <sup>-</sup>	1571	> 29	> 1.25

Table 6.6: Reduced transitional probability  $B(E2)$ , transitional quadrupole moments  $Q_t$  of high K positive and negative-parity bands in  $^{75}\text{Br}$  obtained from present experiment.

$E_x$ (keV)	$I_i^\pi$ ( $\hbar$ )	$I_f^\pi$ ( $\hbar$ )	$E_\gamma$ (keV)	$B(E2)$ (W.u)	$Q_t(\text{Expt})$ (eb)
2310	17/2 <sup>+</sup>	13/2 <sup>+</sup>	790	166 <sup>+28</sup> <sub>-25</sub>	4.53 <sup>+0.37</sup> <sub>-0.36</sub>
3223	21/2 <sup>+</sup>	17/2 <sup>+</sup>	922	176 <sup>+35</sup> <sub>-21</sub>	3.93 <sup>+0.37</sup> <sub>-0.24</sub>
4416	25/2 <sup>+</sup>	21/2 <sup>+</sup>	1193	> 59	> 2.09
3438	21/2 <sup>+</sup>	17/2 <sup>+</sup>	1137	59 <sup>+14</sup> <sub>-12</sub>	2.28 <sup>+0.25</sup> <sub>-0.25</sub>
4525	25/2 <sup>+</sup>	21/2 <sup>+</sup>	1086	> 144	> 3.27
4170	23/2 <sup>-</sup>	19/2 <sup>-</sup>	947	156 <sup>+36</sup> <sub>-32</sub>	3.26 <sup>+0.36</sup> <sub>-0.35</sub>
5293	27/2 <sup>-</sup>	23/2 <sup>-</sup>	1122	159 <sup>+47</sup> <sub>-35</sub>	3.17 <sup>+0.44</sup> <sub>-0.37</sub>
6586	31/2 <sup>-</sup>	27/2 <sup>-</sup>	1293	< 52	> 1.77
3664	21/2 <sup>-</sup>	17/2 <sup>-</sup>	889	156 <sup>+57</sup> <sub>-47</sub>	3.36 <sup>+0.56</sup> <sub>-0.56</sub>
4781	25/2 <sup>-</sup>	21/2 <sup>-</sup>	1117	< 55	> 1.9

K = 9/2 for band G, H and K = 7/2 for band H, I have been used, respectively. These K values are consistent with previously reported value of yrast positive and negative parity band in Ref. [96]. Both  $B(E2)$  and  $Q_t$  for the positive and negative-parity bands are given in Table 6.5 and 6.6.

## 6.4 Results and Discussion

Lifetime measurements are an important tool for the study of rich variety of phenomena observed in the  $A = 80$  mass region. For instance, measurements of transition strengths determine the degree of deformation along a rotational band. Results for the energies of excited states,  $\gamma$ -ray transitions from the initial to the final states, and the corresponding lifetimes are summarized in Table 6.1 - 6.4, respectively. In the present work, lifetimes of total 32 high spin states were measured using DSAM technique, which includes some previous measurements performed with lesser efficiency. In addition, lifetimes of the high spin states in band C, E, H and I were measured for the first time using DSAM technique in the present work and are listed in last column of Table 6.3 - 6.4, respectively. The experimental moment of inertia (MI) of positive and

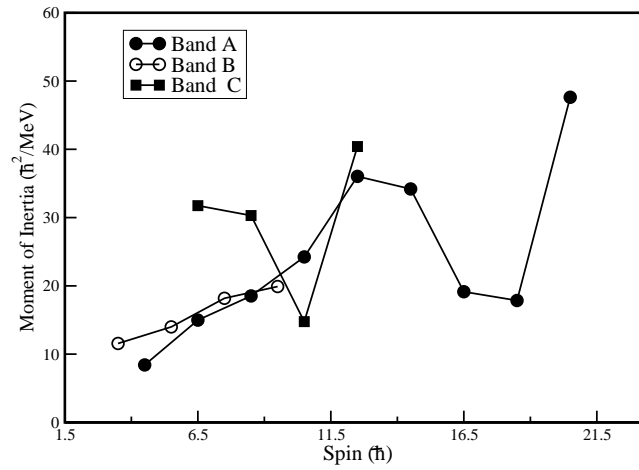


Figure 6.8: Moment of inertia as a function of spin for the positive parity bands in  $^{75}\text{Br}$ .

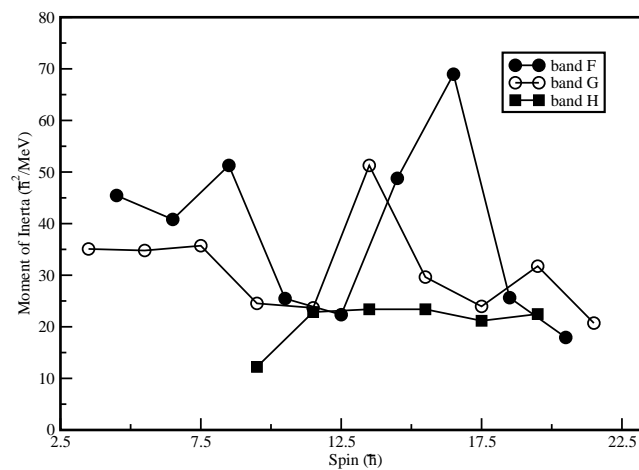


Figure 6.9: Moment of inertia as a function of spin for the negative parity bands in  $^{75}\text{Br}$ .

negative-parity bands (relevant to this work) as a function of spin are shown in Fig. 6.8 and Fig. 6.9. In the yrast positive-parity band (Band A) at  $I = (25/2)\hbar$  rise in MI has been interpreted as alignment of neutron  $g_{9/2}$  orbital on the basis of cranking model [96]. Whereas, in case of negative-parity bands (Band F and G) two irregularities are seen around the spin  $I = (17/2)\hbar$  and  $I = (27/2)\hbar$  due to the alignment of protons and neutrons, respectively. But the plot of MI of band B and C in positive-parity and band H of negative-parity are very regular and hardly show any alignment at higher spins. The total Routhian surface calculations for positive-parity band A indicate two minima in the ground state, one at prolate and the other at oblate deformation [97], showing shape coexistence, which is obvious for  $N = 38$  or  $40$  nuclei.

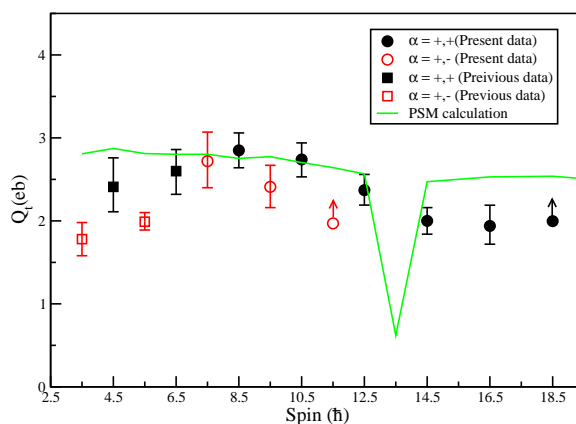


Figure 6.10: Comparison of the measured transitional quadrupole moments  $Q_t$  for excited states in the positive-parity bands in  $^{75}\text{Br}$  with the prediction of the projected shell-model calculation. Circles represent the data from present measurements and the square for previous work reported in Ref. [94], respectively. Filled (open) symbols stand for positive (negative) signature band.

The present work reports the transition quadrupole moments  $Q_t$  measurements beyond the band crossing region and also for high-lying K bands. Fig. 6.10 shows the variation of  $Q_t$  deduced from the measured lifetimes for the yrast positive-parity band A and its signature partner band B. The results show large collectivity below the spin  $(21/2)\hbar$  corresponding to nearly constant average value of transition quadrupole moments which is  $\sim 2.65$  eb. Above this state, the  $Q_t$  values decrease around 10%. The spin at which this reduction in collectivity (or rise in MI) takes place corresponds roughly to the crossing frequency at which a  $g_{9/2}$  neutron alignment occurs in favored

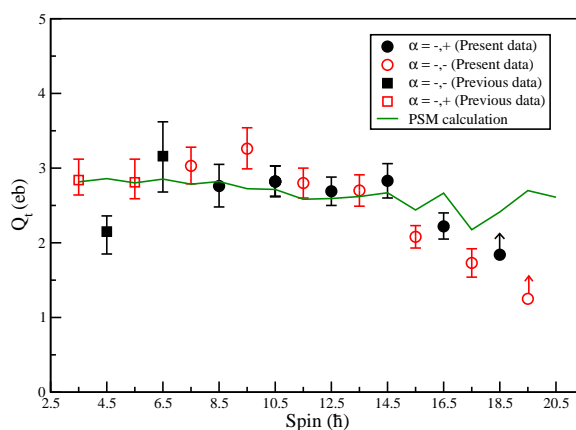


Figure 6.11: Comparison of the measured transitional quadrupole moments  $Q_t$  for excited states in the negative-parity bands in  $^{75}\text{Br}$  with the prediction of the projected shell-model calculation. Circles represents the data from present measurements and the square for previous work reported in Ref. [94], respectively. Filled (open) symbols stand for positive (negative) signature band.

signature, as unfavored signature is weakly populated and observed only upto  $(23/2)\hbar$  spin.

Fig. 6.11 show the variation of  $Q_t$  deduced from the measured lifetimes for the negative-parity bands (band F and G) as a function of spin. From graph it is clear that both the signature partners (band F and G) of negative-parity band have almost similar behavior and the average value of  $Q_t$  are around 2.8 e b before the band crossing and decreases sharply after the band crossing upto  $\sim 1.50$  e b. The spin at which the drop in  $Q_t$  takes place corresponds roughly to the crossing frequency associated with a  $g_{9/2}$  neutron alignment, as indicated by a sudden change in the MI at this point (see Fig. 6.9 )

Transitional quadrupole moments of two additional positive-parity bands with band head spins of  $9/2^+$  and  $11/2^+$  at 302 and 1129 keV, respectively are seen in Fig. 6.12. The  $Q_t$  value for oblate  $9/2^+$  (band C) are higher than all other bands but no alignment effect is seen. Similarly two additional high K bands are observed in negative-parity bands and variation of  $Q_t$  is shown in Fig. 6.13.

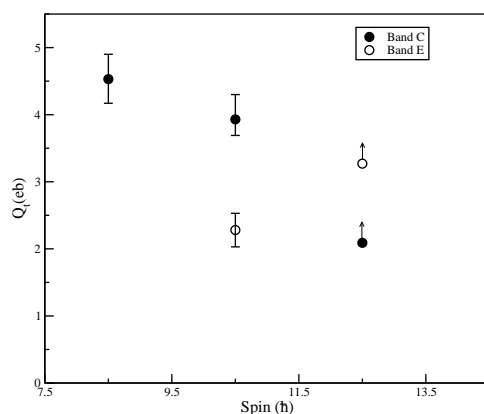


Figure 6.12: Experimental transitional quadrupole moments  $Q_t$  as a function of spin for positive parity high K bands in  $^{75}\text{Br}$ .

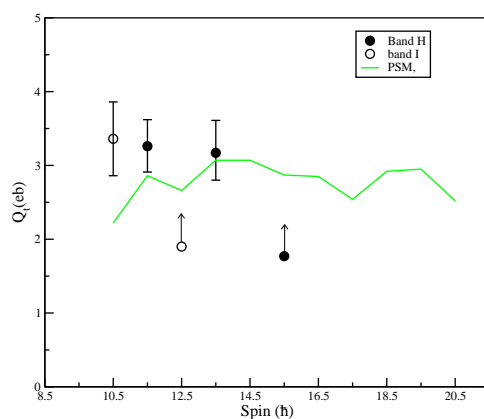


Figure 6.13: Comparison of the measured transitional quadrupole moments  $Q_t$  for excited states in the negative-parity high K bands in  $^{75}\text{Br}$  with the prediction of the projected shell-model calculation.

### 6.4.1 Projected shell-model calculations

In order to investigate the evolution of collectivity for the positive and negative parity bands of  $^{75}\text{Br}$  up to high spins state, projected shell model calculations have been performed. Details of PSM calculations have been already described in chapter 2. Previous calculations using the PSM applied to  $^{75}\text{Kr}$  (previous chapter) explains nicely the evolution of collectivity in both positive and negative-parity bands of  $^{75}\text{Kr}$ .

In the projected shell model approach the basis in which the shell model Hamiltonian is diagonalized, is chosen in the quasi-particle (qp) space. For even-odd nuclei,

the ground-band is a one quasi-particle configuration and in order to describe the high spin structure of a well-deformed even-odd nuclei, it is necessary to consider at least three qp configurations consisting of one proton and two neutrons in the basis. As a matter of fact, due to the Pauli blocking of levels, quite upto high-spins these three qp configurations are sufficient to describe the physics. Thus, for low-lying bands of odd-even nuclei, the quasi-particle configuration space consists of a set of 1-qp and 3-qp states. The PSM uses a rotational-invariant Hamiltonian, including quadrupole-quadrupole, monopole-pairing, and quadrupole-pairing interaction terms which is already discussed in previous chapter. The monopole pairing strength  $G_M$  is taken to be  $G_M = [G_1 - G_2(N - Z)/A] / A$  for neutrons and  $G_M = G_1/A$  for protons with  $G_1 = 18.23$  and  $G_2 = 15.12$ . To compare these pairing strengths to those used in the previous PSM calculations for even-even nuclei in the same mass region (see, e.g., Refs. [80, 4, 92]).

In the calculations, the deformed quasiparticle basis is constructed from the Nilsson single-particle states followed by a BCS calculations. The single-particle space includes all nucleons in the  $N = 2, 3, 4$  major shells. The projected basis is used to diagonalize the shell-model Hamiltonian. The resulting wave functions  $R$  are used to determine transition strengths, and the  $B(E2)$  strengths are used to calculate transition quadrupole moments according to Eq. 5.3. The shell-model basis were constructed using a deformation parameter of  $\epsilon_2 = 0.355$  to remain consistent with the previous PSM results for  $^{75}\text{Kr}$  [92].

The variation of  $Q_t$  with spin for the positive and negative-parity bands are compared with the calculations, in Figs. 6.10 and 6.11, respectively. PSM calculations are plotted by solid curve in the same figure. For completeness, the present measurements of transitional quadrupole moments (see Table 6.5) for spin above  $I = 15/2$  for the positive and negative-parity band are plotted along with the previous measurements from Ref. [96].

In case of positive parity band,  $Q_t$  values obtained from experimental data are in fair agreement with the prediction of PSM calculations within experimental uncertainty

before the band crossing. Whereas, for the lowest spin states of the positive parity the calculated values overestimates the previous measured  $Q_t$  values, as seen in Fig. 6.10. A similar problem was found in  $^{75}\text{Kr}$  [92] as well as for the even-even nuclei of the same mass region [80]. A sharp reduction in  $Q_t$  occurs at spin  $27/2^+$ , just after the  $g_{9/2}$  neutron alignment near the spin  $25/2^+$ . At spins above the band crossing ( $I > 29/2$ ), the average  $Q_t$  value (2.53 eb) is somewhat smaller than that below the crossing (2.8 eb), which overestimates the experimentally observed  $Q_t$  value. As mentioned in earlier chapter, this reduction in  $Q_t$  has been associated with a structure change that occurs as a result of mixing of the configurations with 1-qp and 3-qp state at this spin.

For the negative-parity band the transitional quadrupole moments ( $Q_t$ ) remain constant at low spin i.e up to the band-crossing region, and then reduce slightly. This trend is quite nicely reproduced by the calculated ( $Q_t$ ) values of PSM, as shown in Fig. 6.11. In general, the  $Q_t$  values are in good agreement with those predicted by PSM calculations before the observed drop occurs, but the agreement becomes significantly worse with increasing spin.

## 6.4.2 Shape calculations

Cranked shell model calculations with a deformed Woods-Saxon potential and monopole pairing force are also performed for studying the evolution of shapes in yrast positive and negative parity bands of  $^{75}\text{Br}$ , already discussed in chapters 2 and 5. The calculations generate a total Routhians surface (TRS) plots for a range of shape parameters  $\beta_2$  and  $\gamma$  and minimized with respect to the hexadecapole deformation  $\beta_4$ .

At low rotational frequency, a minimum at near prolate deformation ( $\gamma \approx 0^\circ$ ) and a second less-favorite minimum at oblate deformation ( $\gamma \approx -60^\circ$ ) is predicted in both  $^{75}\text{Kr}$  and  $^{75}\text{Br}$  nuclei, indicating the shape coexistence phenomena. Fig. 6.14 shows two TRS plots for the favored signature of the positive-parity yrast band in  $^{75}\text{Br}$  for two rotational frequencies 0.30 MeV and 0.70 MeV, as a representative, before and after the band crossing. At rotational frequency  $\hbar\omega = 0.30$  MeV, large deformation  $\beta_2 \approx 0.38$  is indicated near the prolate axis at  $\gamma \approx -4^\circ$ . After the first band crossing, at rotational frequency  $\hbar\omega \approx 0.70$  MeV, minimum is shifted towards the triaxial axis

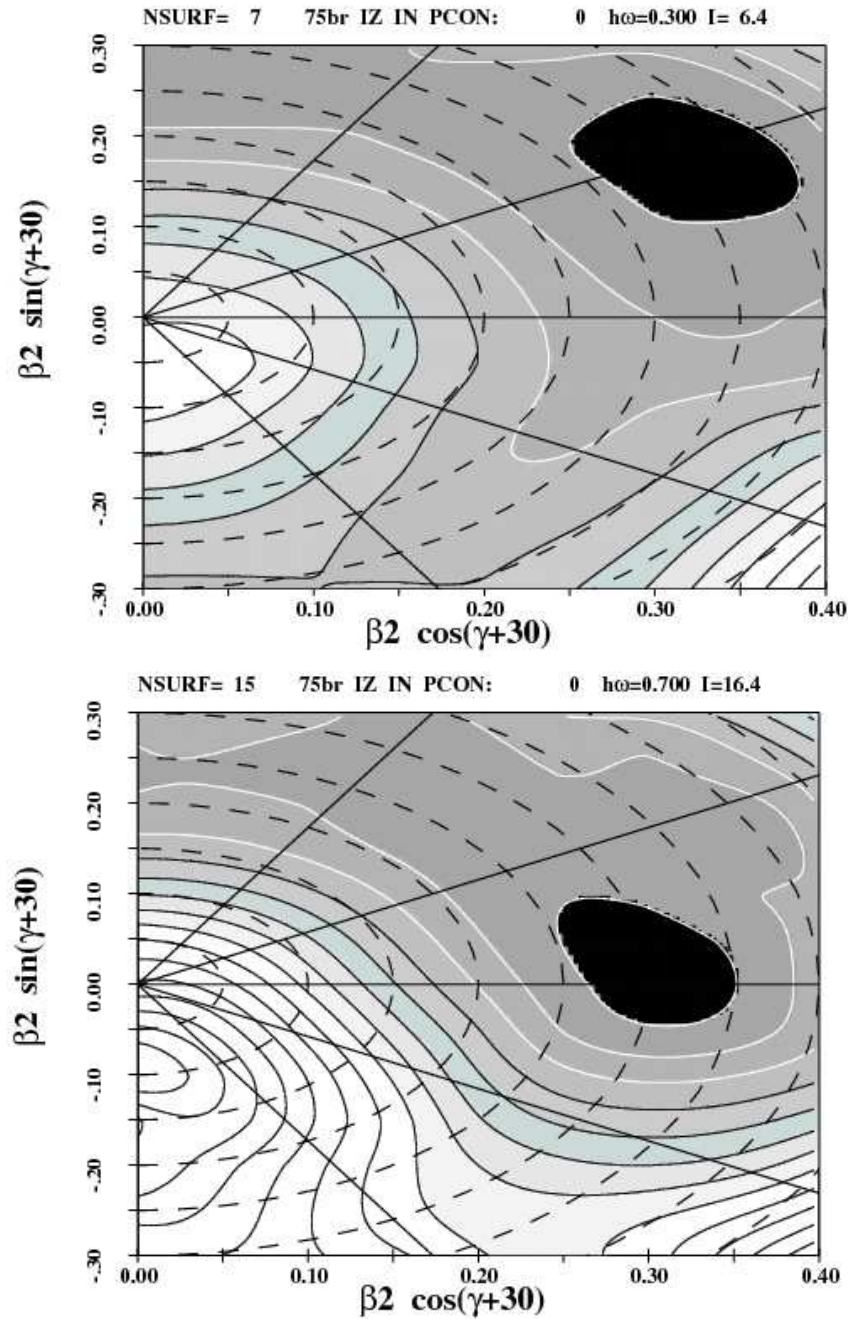


Figure 6.14: Total Routhian Surface (TRS) plots in the  $\beta_2 - \gamma$  plane for positive parity band of  $^{75}\text{Br}$ . Plots are for two rotational frequencies,  $\hbar\omega = 0.30$  MeV (top frame) and  $\hbar\omega = 0.70$  MeV (bottom frame) corresponding to before and after band crossing, respectively.

( $\gamma \approx -25^\circ$ ), indicating less deformed ( $\beta_2 \approx .30$ ) triaxial shape, which is expected from experimental  $Q_t$  plots with spin. The TRS plots for unfavored signature partner band remain almost similar as observed for favored signature and are not shown.

As mentioned above in negative parity band both proton and neutron alignment are possible which occurs at  $\hbar\omega \approx 0.38$  MeV and  $\hbar\omega \approx 0.65$  MeV, respectively (see Figs. 6.8 and 6.9). Accordingly sample of TRS plots for the favored signature ( $\alpha \approx +1/2$ ) of the negative-parity band in  $^{75}\text{Br}$  for three different rotational frequencies  $\hbar\omega = 0.30, 0.50$  MeV and at  $0.70$  MeV are shown in Figs. 6.15. At a frequency of  $0.30$  MeV below the proton alignment, the shape is predicted to be prolate with  $\beta_2 \approx 0.38$  and  $\gamma \approx -2^\circ$ . The minimum in the TRS shifts towards positive value of  $\gamma$  with minimum occurs at  $\beta_2 \approx 0.28$  and  $\gamma \approx 42^\circ$  at rotational frequency  $\hbar\omega \approx 0.5$  MeV (after the proton alignment). Where as, after the neutron alignment i.e. at  $\hbar\omega = 0.70$  MeV, the deformation again shifts towards  $\gamma \approx 40^\circ$  and  $\beta_2 \approx 0.276$  and the nucleus becomes  $\gamma$ -soft. This means that the proton and neutron pair alignments have opposite shape driving effects.

The other signature partner ( $\alpha = -1/2$ ) band have nearly similar features before and after the first band crossing as shown in Figs. 6.16 but difference come after the neutron alignment where the shape become more  $\gamma$ -soft and the minimum in the TRS shifts towards positive value of  $\gamma$  with minimum occurs at  $\beta_2 \approx 0.280$  and  $\gamma \approx 23^\circ$  at rotational frequency  $\hbar\omega \approx 0.70$  MeV Comparing this with the deformation of  $\alpha = +1/2$  band, it is observed that there is although very slight difference of deformation but observable difference in the value of triaxiality which is in fair agreement with the experimental data.

## 6.5 Conclusion

A  $\gamma - \gamma$  coincidence experiment with lifetime measurements was performed to study high-spin states of  $^{75}\text{Br}$  populated through the  $^{50}\text{Cr}(^{28}\text{Si}, 3\text{p})$  reaction at  $90$  MeV. Lifetimes of the 32 high spin states were measured up to highest possible spins along the yrast positive, negative parity, as well as the high K bands of  $^{75}\text{Br}$  using the

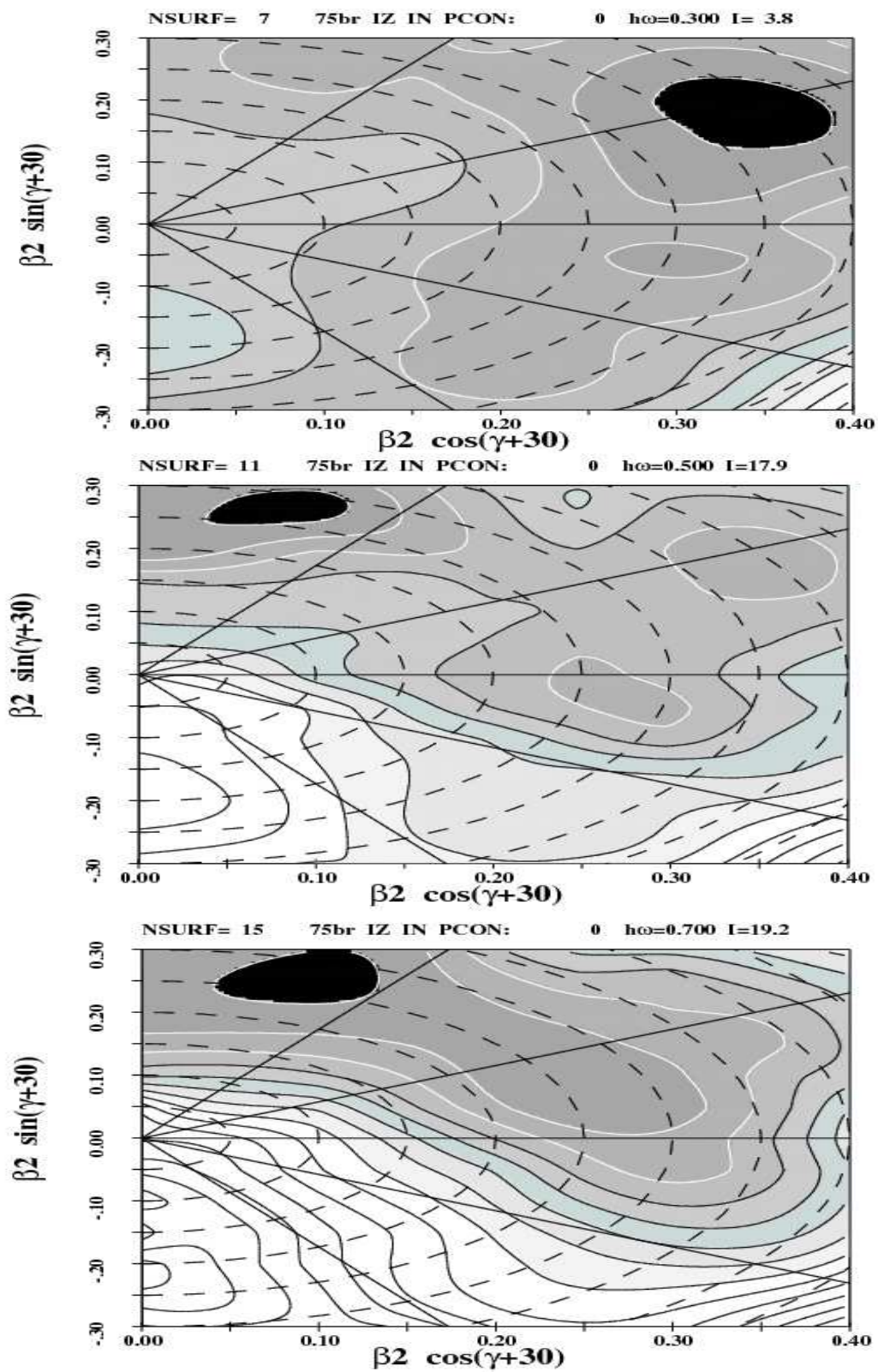


Figure 6.15: TRS plots in the  $\beta_2 - \gamma$  plane for negative-parity  $+1/2$  signature band of  $^{75}\text{Br}$ . Plots are for three rotational frequencies,  $\hbar\omega = 0.30$  MeV (top frame),  $\hbar\omega = 0.50$  MeV (middle frame) and  $\hbar\omega = 0.70$  MeV (bottom frame).

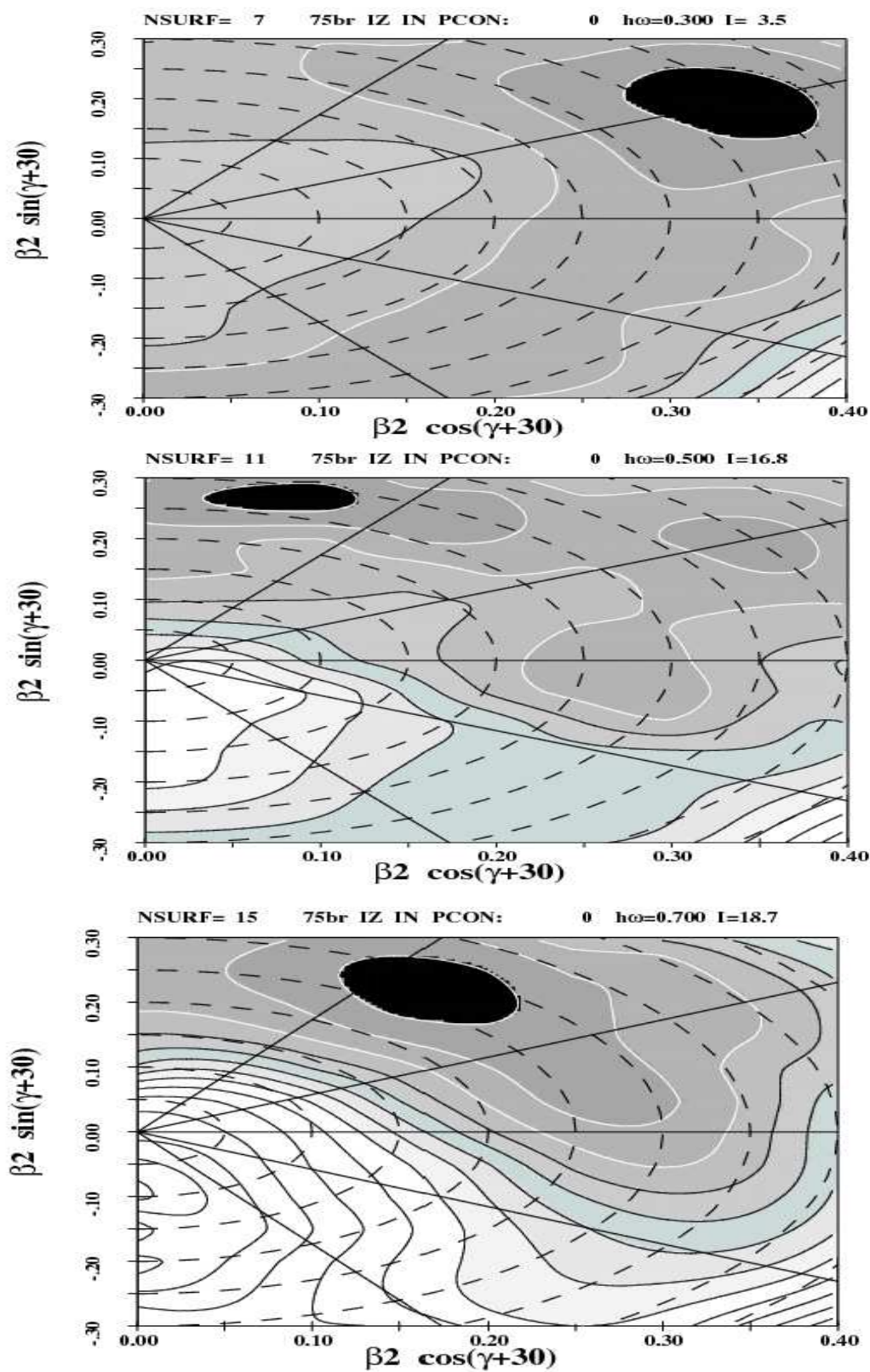


Figure 6.16: TRS plots in the  $\beta_2 - \gamma$  plane for negative-parity  $-1/2$  signature band of  $^{75}\text{Br}$ . Plots are for three rotational frequencies,  $\hbar\omega = 0.30$  MeV (top frame),  $\hbar\omega = 0.50$  MeV (middle frame) and  $\hbar\omega = 0.70$  MeV (bottom frame).

Doppler-shift attenuation method. The extracted transitional quadrupole moments of positive and negative-parity bands remain constant before the band crossing and then decrease after the band-crossing, decrease in negative-parity is more compare to positive-parity band. The experimentally observed transition quadrupole moments are compared with the projected shell-model calculations with reasonable good agreement and further analysis is in progress. The decrease in transition quadrupole moments  $Q_t$  is also predicted with TRS calculations, which shows good evidence for a reduction in deformation following the development of triaxiality near the spin  $25/2$ , due to alignment of quasi-particles.

# Chapter 7

## Shell Model Description of Proton Rich Sn Isotopes

The nuclear shell-model is among the most fundamental model for the microscopic study of the nuclear structure. The structure of neutron deficient nuclei far from  $\beta$  stability is currently key question for nuclear physics community, both experimentally due to development of the radioactive ion beam facilities and high efficiency gamma detector arrays and theoretically due to the development of new effective nucleon-nucleon interactions. Nuclei near the  $N \simeq Z$ , doubly magic core are known to exhibit many new structural phenomenon such as shell evolution, change of collective properties, band termination and magnetic rotation etc. In recent years rich variety of experimental spectroscopic data is now available for neutron deficient Sn isotopes by various experimental studies like intermediate energy Coulomb excitation experiments using RISING setup at GSI [28, 29] and at NSCL [30].  $\beta$  decay spectroscopy of lighter Sn [26, 27] also gives more valuable information for the low-lying levels. Meanwhile, substantial theoretical progress has been made in nuclear structure calculations in recent years. The existing radioactive ion beam facilities and forthcoming future cutting-edge research facilities, advance our understanding of nuclear structure and nuclear astrophysics. These facilities allow, from low to relativistic energies, for the study of reactions with exotic nuclei that have never been accessible before providing challenges for reaction theory as well as strong constraints on nuclear structure models.

From theoretical point of view the Sn isotopes are interesting to study, as they are

unique testing ground for nuclear structure calculations. Thus theoretical calculations for these nuclei are of great importance. Shell-model calculations for Sn isotopes have been performed by Engeland *et al.* [98], Covello *et al.* [99] and Schubart *et al.* [100] treating  $^{100}\text{Sn}$  as stable core, almost more than one decade back. The main deficiency of the work of Schubart is that the two body interaction in their calculations has to be scaled by a factor of 1.4 to give reasonable agreement with the experiments. Thus the spectrum is not very reliable. In the present work, large scale shell-model calculations have been performed for neutron deficient even  $^{102-108}\text{Sn}$  and odd  $^{103-107}\text{Sn}$  isotopes using more recent data of single particle spectrum and realistic interactions obtained by renormalization of Bonn and Paris potentials. The calculations have been performed using full sdgh model space consisting of  $1g_{7/2}$ ,  $2d_{5/2}$ ,  $2d_{3/2}$ ,  $3s_{1/2}$  and  $1h_{11/2}$  [101]. As nuclear shell-model is one of the most successful tool used for the interpretation of low lying states of nuclei near the proton or neutron shell closer, the aim of present work is to test both effective interactions for these lighter Sn isotopes near the  $N \simeq Z$  line where pairing correlation are more important. This chapter describes in brief a general introduction to the large scale shell-model calculations for proton rich Sn isotopes.

## 7.1 Techniques of calculations and Shell-Model code

The Shell-Model (SM) has always been considered as a fundamental tool for the study of the nuclear structure. Modern large-scale shell-model calculations give the most accurate and comprehensive description of nuclei far from  $\beta$ -stability. It can not only predict low-lying energy levels but also one of the most important theoretical predictions to compare with the experimental findings like g-factor, magnetic moments and quadrupole moments of very exotic nuclei. In the shell-model calculations one calculates the total energy relative to a closed core instead of calculating the total energy of the entire system of  $A$  valence nucleons.

The three pillars of the shell-model are namely, model space, effective interaction and shell-model code to diagonalize the matrices, which will be discussed in the following sections. Two main problems appear in a shell-model description of the nuclear

structure. The first one is related to its very foundations, i.e. to the possibility of obtaining a regularized effective interaction in a given valence space, from the bare nucleon-nucleon force. In its present state, effective interactions cannot be used in SM calculations without some phenomenological corrections.

The second problem is technical: with the increase of the size of the valence space or (and) the increase of the number of particles (holes) the dimension of matrices explodes. This explains why SM calculations have been only extensively done for

- light nuclei,  $p$  shell and  $s - d$  shell.
- heavy nuclei with only few particles (holes) outside an inert core or for semi-magic nuclei.

### 7.1.1 Model space

One assume that the valence nucleons occupy selected single particle levels (called the model space), outside an inert core. It is assumed that all the properties of the nucleus are governed by these nucleons. Generally, the best and most complete results are obtained when the model space is as large as possible. However, the computation time increases with the size of model space and empirical Hamiltonians are better determined in smaller model spaces. Thus the choice of model space is a compromise between what one would like to describe and what is computationally practical.

### 7.1.2 Effective interactions

The matrix elements of a given interaction between many-particle states can be expressed in terms of two-body matrix elements. The value of the matrix elements depends on the residual interaction, the single-particle wave functions and on the total

spin and isospin of the two-particle system.

### 7.1.2.1 Microscopic effective interactions

One of the most successful approaches for the effective nuclear interaction is based on Brueckner's G-matrix [102, 103]. It treats two nucleons in nuclear medium in a way analogous to the scattering of two nucleons in vacuum. The problem of the hard core that arises in the scattering of free nucleons is solved by performing an infinite summation of the scattering processes of two nucleons in the nuclear medium. The resulting effective interaction is well-behaved at short distances. At the same time many-body effects are consistently treated when just applying the bare force.

The G-matrix is obtained by solving the Bethe-Goldstone equation [104].

$$G(\omega) = V + V \frac{Q_2 P}{\omega - H_0} G(\omega) \quad (7.1)$$

Here,  $\omega$  is the 'starting energy' at which  $G$  is computed.  $H_0$  is the unperturbed Hamiltonian for the intermediate two-particle state.  $V$  is the bare interaction between two nucleons unmodified for the nuclear medium.  $Q_2 P$  is a two-particle projection operator that guarantees that the scattered particles obey the Pauli exclusion principle: the two nucleons can only be scattered to unoccupied states, hence to states that lie above the Fermi energy. The effective interaction derived from this G-matrix can be expressed as:

$$\nu_{eff} = G + G \frac{Q'}{E_{0v} - H_0^V} \nu_{eff} \quad (7.2)$$

where  $H_0^V$  is describing the single-particle Hamiltonian for the valence space, and  $E_{0v}$  is the corresponding single-particle energy. The prime on the projection operator  $Q'$  indicates that the expansion of  $\nu_{eff}$  does not sum over two-particle ladder diagrams already included in  $G$ , in order to avoid double-counting. The first such derived effective interaction is the one of Kuo and Brown in the sd-shell. Another example of an often used effective interaction based on the G-matrix by Hjorth-Jensen [105], developed for the  $1p_{3/2}$ ,  $0f_{5/2}$ ,  $1p_{1/2}$ ,  $0g_{9/2}$  space.

### 7.1.2.2 Phenomenological effective interactions

In this approach an effective interaction is developed by using the single-particle energies and two-body matrix elements as parameters in a fit for a particular mass region [106]. The single-particle energies are usually taken from the spectrum of the nucleus with the same core plus one nucleon. The energy levels calculated with these parameters are compared to the experimental energy levels and the parameter values are adjusted by means of a least-square fitting procedure. An advantage of the empirical approach is that it is not necessary to explicitly specify the interaction in order to correlate experimental energy spectra. The disadvantage of this method is that in many cases the number of parameters is very large and the selection of experimental states that are thought to be described will in the assumed model space may become rather arbitrary.

### 7.1.2.3 Schematic effective interactions

Departing from the basic properties of the nuclear force, we also use the properties of some of the simple forces such as multiple forces, zero-range or delta-forces and spin exchange component. The particular characteristic of these interactions provide insight in the description of nuclear structure properties. The delta interaction which is more popular in the sd-shell is SDM . There are systematic discrepancies with respect to the experimentally observed level energies in SDM interaction which is removed in the modified surface delta interaction (MSDI).

The delta-interaction is defined as:

$$V_{\delta}(1, 2) = -V(r)\delta(\vec{r}_1 - \vec{r}_2), \quad (7.3)$$

and as such, is a zero-range interaction, the simplest approximation for the short-range character of the nuclear force. Its attractive character is ensured by the minus sign. Moreover, the  $\delta$ -force can be extended by including a spin-exchange component:

$$V_{\delta}(1, 2) = -V_0(1 - \alpha + \alpha\vec{\sigma}_1 \cdot \vec{\sigma}_2)\delta(\vec{r}_1 - \vec{r}_2), \quad (7.4)$$

with  $\alpha$  the degree of spin-exchange, varying between 0 and 1, and  $V_0$  the strength of the interaction and given in units  $\text{MeV}\cdot\text{fm}^3$ .

### 7.1.3 Shell model code: Nushell

Nushell is a shell-model code developed by Alex Brown from MSU to tackle dimensions up to  $10^6$  in the J-T scheme and about  $2 \times 10^7$  in the M-scheme . NuShell generates the basis states in  $m$ -scheme and then computes the matrix in the j scheme. Therefore, it bypasses the complication of the angular momentum algebra in j-j coupled basis and also avoids the huge matrix dimension generated during  $m$ -scheme . NuShell code consists of seven main programs and some supporting codes, briefly mention here.

#### 7.1.3.1 Sequence of programs for energies

- **SHELL:** It creates batch file .bat that coordinates the program sequence and their inputs. Alternatively, the input is from a .ans file that has been made by a previous run of shell.
- **NUBASIS:** It makes a list of all possible M-scheme basis states for a given model space together with a given set of restrictions.
- **NUPROJ:** It makes linear combinations of the M-scheme basis states that have good J values in p/n formalism or good J and T in isospin formalism.
- **NUMATRIX:** It makes the matrix corresponding to the J (or JT) dimension of the problem. Only the non-zero matrix elements are stored.
- **NULANCZOS:** It find the lowest N eigenvalues for the matrix. The default value of N is 10.

### 7.1.3.2 Sequence of programs for overlaps and transitions

- **MVEC**: It reads the output of Proj and Lanczos to make the eigenvectors in the M-scheme basis and it is used as input to Tramp.
- **TRAMP**: It calculates overlaps between two wave functions. It can be used with the den option within shell to obtain: t - one-body transition density.
- **TBTDOP**: It makes an intermediate file needed for two-body transition densities.

### 7.1.3.3 Other programs

- **DENS**- calculates the radial wave functions for a given nucleus with oscillator, Woods-Saxon or Skyrme Hartree-Fock potentials and reads the \*.obd from nushell to calculate B(EL), B(ML) and B(GT) values.
- **LEVEL**-provides a level scheme for a given set of J values.
- **PN** converts a given set of \*.sp and \*.int files in isospin formalism into their equivalent in proton-neutron (pn) formalism.

## 7.2 Diagonalization via LANCZOS method

In the large-scale shell-model calculations, the standard diagonalization methods (Wilkinson 1965) where the CPU time increases as  $N^3$ ,  $N^3$  being the dimension of matrix. Therefore these methods cannot be used in large-scale shell-model calculations. The iterative methods are of general use, in particular the Lanczos method (Lanczos, 1950). The (real symmetric) matrix is diagonalized at each iteration, and the iterative process continues until all the required eigenvalue are converged according to some criterion. The number of iterations depends little on the dimension of the matrix. Besides, the computing time is directly proportional to the number of matrix elements and for this reason it is nearly linear (in the dimension of the matrix, instead of cubic as in the standard methods). It depends on the number of iterations, which in turn

depends on the number of converged states needed, as well as on the choice of starting vector (the pivot state).

We start with a normalized vector (pivot state)  $\phi_1$  and apply  $H$  operator on this vector. Then we get a parallel and an orthogonal components to the initial vector  $\phi_1$ :

$$H |\phi_1\rangle = E_{11} |\phi_1\rangle + E_{12} |\phi_2\rangle \quad (7.5)$$

with  $E_{11} = \langle \phi_1 | H | \phi_1 \rangle$  and  $E_{12} |\phi_2\rangle = H |\phi_1\rangle - E_{11} |\phi_1\rangle$ . Acting again with  $H$  on  $\phi_2$ , we generate a third vector  $\phi_3$  orthogonal to the first two.

$$H |\phi_2\rangle = E_{21} |\phi_1\rangle + E_{22} |\phi_2\rangle + E_{23} |\phi_3\rangle \quad (7.6)$$

$E_{21} = E_{12}$  since in our basis  $H$  matrix is real-symmetric.

Continuing this process, at iteration  $n$ , we obtain the diagonal energy of the vector  $|\phi_n\rangle$ , a new vector  $|\phi_{n+1}\rangle$  and the non diagonal energy  $E_{nn+1}$ .

$$H|\phi_n\rangle = E_{nn-1}|\phi_{n-1}\rangle + E_{nn}|\phi_n\rangle + E_{nn+1}|\phi_{n+1}\rangle,$$

$$E_{nn-1} = E_{n-1n}, E_{nn} = \langle \phi_n | H | \phi_n \rangle, \text{ and}$$

$$E_{nn+1}|\phi_{n+1}\rangle = H|\phi_n\rangle + E_{nn}|\phi_n\rangle - E_{nn-1}|\phi_{n-1}\rangle.$$

Due to the hermiticity of  $H$ , the construction of the Lanczos matrix ensures that all the elements  $E_{ij}$  with  $|i - j| > 1$  are zero.

The choice of the pivot state is crucial because iterative process will continue until all the eigenvalues that we need are converged. There are different ways to accelerate the convergence.

To restore the good quantum numbers in the pivot state. For example, in m-scheme, we project the pivot state on  $J^2$  and  $T^2$  ( this projection is achieved in doing a Lanczos calculations with the  $J^2$  and  $T^2$  operators). Especially when we need only one

converged state, it is interesting to use as pivot state the solution obtained in a truncated space. An important point to notice is that all the Lanczos vectors must be kept during the calculations. There are two reasons for this; firstly, we need them to calculate the eigenvectors and secondly because of numerical reasons. Mathematically the Lanczos vectors should be orthogonal, however numerically this is strictly so. Hence, small numerical precision errors can, after some iterations, produce catastrophes (e.g. the lowest states may reappear many times).

### 7.3 Details of calculations

Large scale shell-model calculations of the low-lying spectra for proton rich even ( $A = 102, 104, 106, 108$ ) and odd ( $A = 103, 105, 107$ ) Sn isotopes have been performed considering  $^{100}\text{Sn}$  as closed core. Valence neutrons are distributed over the single particle orbits  $1g_{1/2}$ ,  $2d_{5/2}$ ,  $2d_{3/2}$ ,  $3s_{1/2}$  ( $N=4$  oscillator shell) and the intruder orbit  $1h_{11/2}$  from  $N=5$  oscillator shell. The single particle energies and two body matrix element (TBME) are two most important ingredients in any shell-model calculations. Shell-model calculations were performed using the Nushell code [107] for two sets of nucleon-nucleon interactions. The first set of two body matrix elements named sn100pn was obtained from a realistic interaction calculated by Brown *et al* [108], starting with G matrix derived from CD Bonn nucleon nucleon interaction. The second set of TBME named snet was obtained from bare G matrix by Hoska [109] based on renormalized Paris potential for  $N=82$  nuclei [110]. The Coulomb interaction was added to the interaction between protons. Thus, there are three parts to the Hamiltonian, the proton-proton (pp), neutron-neutron (nn), and proton-neutron (pn) interactions. Since no experimental information is available for the single particle energies of  $^{101}\text{Sn}$ , calculated values of single particle energies shown in Table 7.1 for two different interactions have been used. The calculations have been performed without any truncation except in case of  $^{108}\text{Sn}$  where we have put maximum two particles in  $h_{11/2}$  orbital.

A harmonic oscillator basis was chosen for the single particle wave function, with an oscillator energy  $\hbar\omega$ . It is important for the present work to include all neutron

Table 7.1: Single particle energies used in two different shell-model approaches.

orbital nlj	sn100pn	snet Energy(MeV)
2d <sub>5/2</sub>	-10.6089	-10.15
1g <sub>7/2</sub>	-10.2893	-10.10
3s <sub>1/2</sub>	-8.7167	-8.40
2d <sub>3/2</sub>	-8.6944	-8.09
1h <sub>11/2</sub>	-8.8152	-7.85

configurations in the model space. This means diagonalization of large dimension matrices. In Nushell computer code a procedure based on the Lanczos algorithm where the states are given in the m-scheme Slater determinant basis is used. This technique is an iterative procedure where the lowest states are first calculated. More recent data of single particle energy has been used in this calculations.

## 7.4 Results and Discussion

### 7.4.1 Excitation energies of even Sn isotopes

The resulting energy spectra for even  $^{102-108}\text{Sn}$  isotopes are displayed in Figs.[7.1-7.4]. Only first excited states for each spectra are plotted up to 4.5 MeV excitation energy. Some characteristic properties are observed in the data.

In Table 7.1 we have listed experimental [111] and theoretical levels for  $^{102}\text{Sn}$  and plotted them in Fig. 7.1. Only three excited states with  $J^\pi = 2^+, 4^+$  and  $6^+$  have been observed experimentally. The ground state  $0^+$  and first excited  $2^+$  state are well predicted by both the interactions. The calculated  $2^+$  state lies  $\sim 230$  keV and 335 keV above the experimental level in sn100pn and snet interactions, respectively. In general the levels obtained with with snet lie slightly higher than those with sn100pn due to coulomb term. The main point of disagreement being the position of the  $4^+$  state which is reproduced very well by snet interaction but in case of sn100pn interaction it lies above the  $6^+$  state. Again  $6^+$  is in good agreement with both the interactions. Many states between 1.5 to 3 MeV excitation energy have been predicted whereas only two

Table 7.2: Experimental [111] and theoretical low-lying states of  $^{102}\text{Sn}$ . Energies are in MeV.

$J^\pi$	Exp.	$J^\pi$	sn100	$J^\pi$	snet
(0 <sup>+</sup> )	0.000	0 <sup>+</sup>	0.000	0 <sup>+</sup>	0.000
(2 <sup>+</sup> )	1.472	2 <sup>+</sup>	1.683	2 <sup>+</sup>	1.689
(4 <sup>+</sup> )	1.969	6 <sup>+</sup>	2.063	4 <sup>+</sup>	2.011
(6 <sup>+</sup> )	2.051	4 <sup>+</sup>	2.129	6 <sup>+</sup>	2.089
-	-	0 <sup>+</sup>	2.301	2 <sup>+</sup>	2.484
-	-	1 <sup>+</sup>	2.381	0 <sup>+</sup>	2.565
-	-	2 <sup>+</sup>	2.396	1 <sup>+</sup>	2.593
-	-	6 <sup>+</sup>	2.582	4 <sup>+</sup>	2.666
-	-	4 <sup>+</sup>	2.617	6 <sup>+</sup>	2.680
-	-	3 <sup>+</sup>	2.670	3 <sup>+</sup>	2.692
-	-	5 <sup>+</sup>	2.733	5 <sup>+</sup>	2.805

have been observed experimentally so far..

The energy levels calculated for  $^{104}\text{Sn}$  nuclei are tabulated in Table 7.2 and compared with experimental data [112]. Resulting experimental and calculated spectra are shown in Fig. 7.2. The ordering of levels is predicted very well from 0<sup>+</sup> ground state to 10<sup>+</sup> excited states by both the interactions. In order to interpret the experimental results of  $^{104}\text{Sn}$ , Gorska *et al.* [112] have done the shell-model calculations using snet interaction. Here we are also reporting these calculations along with sn100pn interaction for systematic study of these nuclei in this mass region. In both the calculations the first excited state 2<sup>+</sup> is slightly above the experimentally observed 2<sup>+</sup> state with a spacing of 1.26 MeV above the ground state. Energy gap of about 680 keV above the first excited 2<sup>+</sup> and 4<sup>+</sup> state is well reproduced by both the interactions. The higher states 8<sup>+</sup> and 10<sup>+</sup> are calculated at 3.623 and 3.995 MeV from sn100pn interaction whereas by snet interaction they lie at 3.505 MeV and 3.826 which are in good agreement with experimental values.

In Table 7.3 experimental [113] and shell-model low-lying levels are listed for  $^{106}\text{Sn}$  and energy spectra obtained are shown in Fig. 7.3. More recently shell-model calculations has been done by Dikmen [114] for  $^{106}\text{Sn}$  using CD Bonn potential. The calculated level reported in this paper are bit over estimated the experimentally ob-

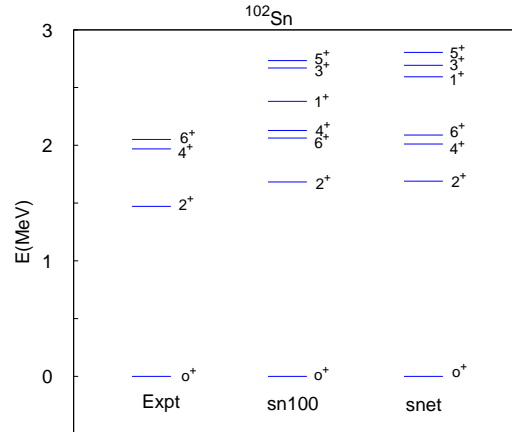
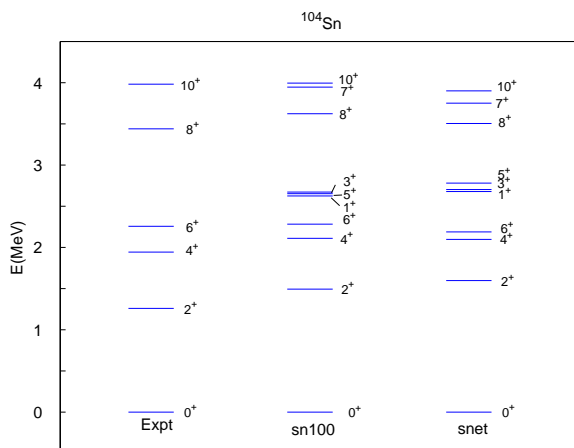


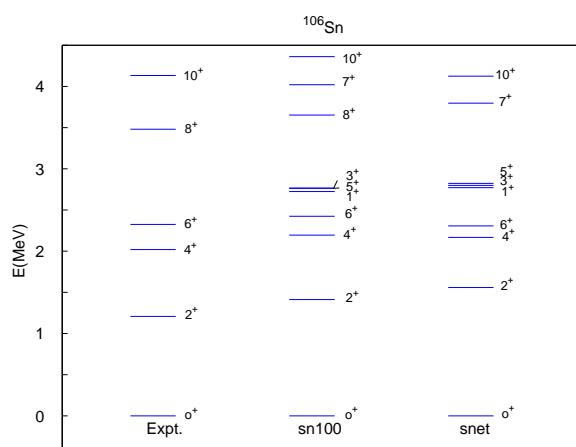
Figure 7.1: Experimental [111] and calculated energy levels of  $^{102}\text{Sn}$  with sn100 and snet interactions.

Table 7.3: Experimental [112] and theoretical low-lying states (up to 4.5 MeV) of  $^{104}\text{Sn}$ . Energies are in MeV.

$J^\pi$	Exp.	$J^\pi$	sn100	$J^\pi$	snet
$(0^+)$	0.000	$0^+$	0.000	$0^+$	0.000
$(2^+)$	1.260	$2^+$	1.494	$2^+$	1.597
$(4^+)$	1.943	$4^+$	2.111	$4^+$	2.098
$(6^+)$	2.257	$6^+$	2.282	$6^+$	2.188
$(8^+)$	3.440	$0^+$	2.358	$0^+$	2.337
$(10^+)$	3.981	$2^+$	2.537	$2^+$	2.534
-	-	$1^+$	2.624	$4^+$	2.609
-	-	$4^+$	2.633	$1^+$	2.679
-	-	$5^+$	2.652	$3^+$	2.702
-	-	$3^+$	2.672	$5^+$	2.780
-	-	$6^+$	2.797	$6^+$	2.861
-	-	$5^+$	3.038	$3^+$	3.074
-	-	$3^+$	3.061	$5^+$	3.083
-	-	$1^+$	3.345	$8^+$	3.505
-	-	$8^+$	3.623	$1^+$	3.543
-	-	$7^+$	3.946	$7^+$	3.751
-	-	$10^+$	3.995	$10^+$	3.826

Figure 7.2: Same as Fig. 7.1 for  $^{104}\text{Sn}$ .Table 7.4: Experimental [113] and theoretical low-lying states (up to 4.5 MeV) of  $^{106}\text{Sn}$ . Energies are in MeV.

$J^\pi$	Exp.	$J^\pi$	sn100	$J^\pi$	snet
$(0^+)$	0.000	$0^+$	0.000	$0^+$	0.000
$(2^+)$	1.208	$2^+$	1.413	$2^+$	1.558
$(4^+)$	2.202	$4^+$	2.194	$4^+$	2.167
$(6^+)$	2.324	$6^+$	2.424	$6^+$	2.306
$(8^+)$	3.480	$0^+$	2.430	$0^+$	2.361
$(10^+)$	4.133	$2^+$	2.592	$4^+$	2.615
-	-	$4^+$	2.676	$2^+$	2.625
-	-	$1^+$	2.723	$1^+$	2.771
-	-	$5^+$	2.762	$3^+$	2.799
-	-	$3^+$	2.766	$5^+$	2.822
-	-	$6^+$	2.985	$6^+$	2.932
-	-	$5^+$	3.080	$5^+$	3.169
-	-	$1^+$	3.481	$3^+$	3.293
-	-	$8^+$	3.652	$1^+$	3.692
-	-	$7^+$	4.020	$7^+$	3.797
-	-	$7^+$	4.119	$10^+$	4.125
-	-	$10^+$	4.362	-	-

Figure 7.3: Same as Fig. 7.1 for  $^{106}\text{Sn}$ .

served once while our calculations using snet interaction are even more closer to the experimentally observed values except the  $8^+$  level. The position of  $8^+$  level at 3.652 MeV from sn100pn interaction agrees with experimentally observed at 3.480 MeV but is much over estimated by snet interactions. Again the  $10^+$  state is in good agreement with experimental data from both the interaction.

Table 7.4 contains experimentally [115] observed states up to 4.5 MeV excitation energy and compared with shell-model calculations for  $^{108}\text{Sn}$ . In both set of shell-model calculations, performed for  $^{108}\text{Sn}$  a restriction of maximum two particles in  $h_{11/2}$  orbital has been put. The fit of experimental levels from theoretical calculations are shown in Fig. 7.4. It has been observed that experimental levels are in better agreement from sn100pn interactions compared to the previous work done by Dikmen [114] but significant discrepancy remains from snet interactions above  $4^+$  state, which may be due to the deficiency in the residual interaction. In fact with this interaction we are not able to reproduce the level above  $4^+$  state.

In Figs. 7.5 and 7.6, we have compared the calculated excitation energies of first excited  $2^+$  and  $4^+$  states for even A Sn isotopes (102 to 108), with the experimental data. We see that the behavior of energy as a function of A is remarkable well reproduced in all cases, the largest discrepancy is seen in the  $^{106}\text{Sn}$  nuclei which lie above in

Table 7.5: Experimental[115] and theoretical low-lying states (up to 4.5 MeV) of  $^{108}\text{Sn}$ . Energies are in MeV.

$J^\pi$	Exp.	$J^\pi$	sn100	$J^\pi$	snet
(0 <sup>+</sup> )	0.000	0 <sup>+</sup>	0.000	0 <sup>+</sup>	0.000
(2 <sup>+</sup> )	1.208	2 <sup>+</sup>	1.186	2 <sup>+</sup>	1.498
(4 <sup>+</sup> )	2.111	4 <sup>+</sup>	2.142	4 <sup>+</sup>	2.177
(6 <sup>+</sup> )	2.365	2 <sup>+</sup>	2.264	0 <sup>+</sup>	2.325
(8 <sup>+</sup> )	3.561	6 <sup>+</sup>	2.297	2 <sup>+</sup>	2.606
(10 <sup>+</sup> )	4.256	0 <sup>+</sup>	2.315	4 <sup>+</sup>	2.606
-	-	4 <sup>+</sup>	2.338	5 <sup>+</sup>	2.767
-	-	1 <sup>+</sup>	2.575	3 <sup>+</sup>	2.797
-	-	5 <sup>+</sup>	2.588	5 <sup>+</sup>	3.114
-	-	3 <sup>+</sup>	2.607	3 <sup>+</sup>	3.336
-	-	6 <sup>+</sup>	2.985	7 <sup>+</sup>	3.665
-	-	5 <sup>+</sup>	2.759	7 <sup>+</sup>	4.136
-	-	6 <sup>+</sup>	2.840	-	-
-	-	3 <sup>+</sup>	2.886	-	-
-	-	1 <sup>+</sup>	3.006	-	-
-	-	8 <sup>+</sup>	3.502	-	-
-	-	7 <sup>+</sup>	3.612	-	-
-	-	10 <sup>+</sup>	4.051	-	-

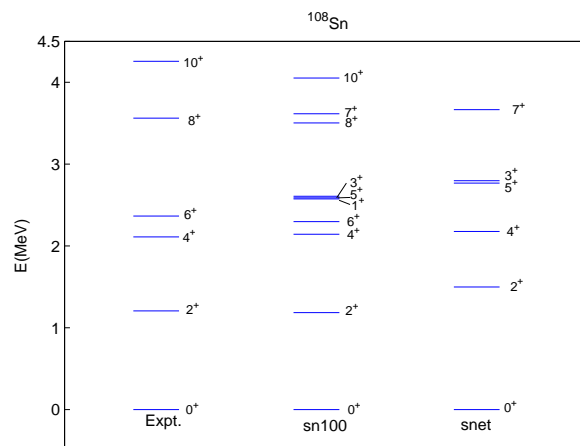


Figure 7.4: Same as Fig. 7.1 for  $^{108}\text{Sn}$ .

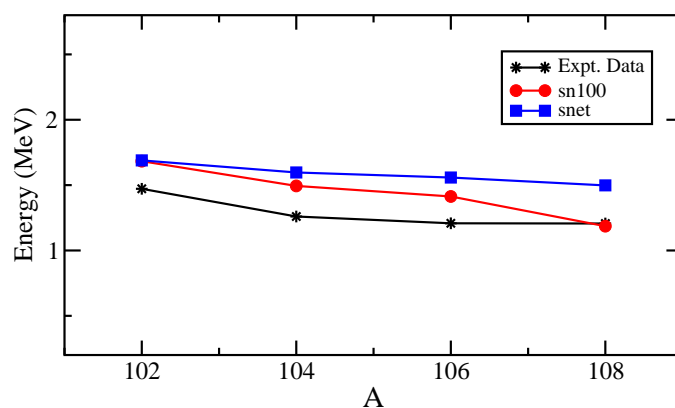


Figure 7.5: Comparison of energy of the first  $2^+$  excited state from shell model calculations with experimental data for even Sn isotopes with A ranging from 102 to 108.

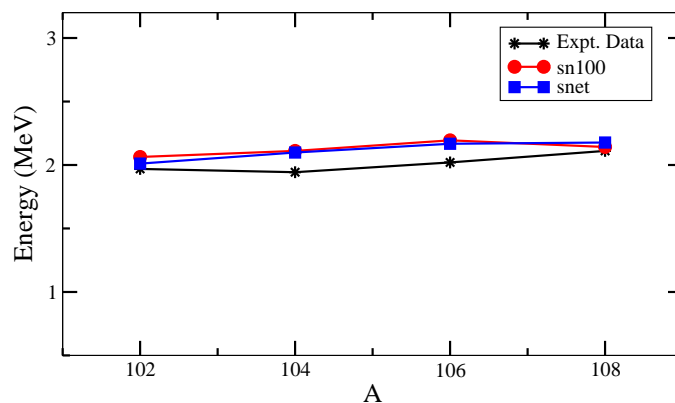


Figure 7.6: Comparison of energy of the first  $4^+$  excited state from shell model calculations with experimental data for even Sn isotopes with A ranging from 102 to 108.

both  $2^+$  and  $4^+$  excited state. It should be noted that the agreement with the experiment is satisfactory. Since it is very difficult to study these Sn isotopes experimentally far from stability, we are expecting more experimental data with the development of state of art facility. In our calculations we have many more levels as compared to the levels experimentally known which can be used as a guide line for future experiments.

#### 7.4.2 Excitation energies of odd Sn isotopes

The resulting energy spectra for odd  $^{103-107}\text{Sn}$  isotopes are shown in Figs.[7.7 -7.9]. Energy spectra are plotted up to 2.5 MeV excitation energy whereas previous calcu-

Table 7.6: Experimental [116] and theoretical low-lying states (up to 2.5 MeV) of  $^{103}\text{Sn}$ . Energies are in MeV.

$J^\pi$	Exp.	$J^\pi$	sn100	$J^\pi$	snet
(5/2 <sup>+</sup> )	0.000	5/2 <sup>+</sup>	0.000	5/2 <sup>+</sup>	0.000
(7/2 <sup>+</sup> )	0.168	7/2 <sup>+</sup>	0.026	7/2 <sup>+</sup>	0.077
(11/2 <sup>+</sup> )	1.486	5/2 <sup>+</sup>	1.124	3/2 <sup>+</sup>	1.008
(13/2 <sup>+</sup> )	1.785	1/2 <sup>+</sup>	1.186	5/2 <sup>+</sup>	1.241
-	-	7/2 <sup>+</sup>	1.282	3/2 <sup>+</sup>	1.284
-	-	3/2 <sup>+</sup>	1.307	9/2 <sup>+</sup>	1.399
-	-	3/2 <sup>+</sup>	1.355	1/2 <sup>+</sup>	1.512
-	-	9/2 <sup>+</sup>	1.395	7/2 <sup>+</sup>	1.521
-	-	11/2 <sup>+</sup>	1.635	11/2 <sup>+</sup>	1.601
-	-	9/2 <sup>+</sup>	1.717	9/2 <sup>+</sup>	1.612
-	-	1/2 <sup>+</sup>	1.749	1/2 <sup>+</sup>	1.660
-	-	11/2 <sup>+</sup>	1.763	11/2 <sup>+</sup>	1.751
-	-	13/2 <sup>+</sup>	1.798	17/2 <sup>+</sup>	1.925
-	-	17/2 <sup>+</sup>	1.876	13/2 <sup>+</sup>	1.931
-	-	15/2 <sup>+</sup>	1.924	15/2 <sup>+</sup>	1.938
-	-	15/2 <sup>+</sup>	2.066	15/2 <sup>+</sup>	2.010

lations were performed up to 1.5 or 2 MeV. Here we have extended the calculations and better agreement have been observed in this energy region. Some characteristic features have been reported in this section.

Table 7.7 shows the comparison between experimental[116] excitation energies and the results of the calculations for  $^{103}\text{Sn}$ . Only three excited states 7/2<sup>+</sup>, 11/2<sup>+</sup> and 13/2<sup>+</sup> are known experimentally till now. From Fig. 7.7 we can see that in both sets the splitting of two lowest-lying states 5/2<sup>+</sup> and 7/2<sup>+</sup>, which are essentially single particle in nature, is slightly under estimated by  $\sim 140$  and  $\sim 80$  keV from sn10pn and snet interactions, respectively. Above 7/2<sup>+</sup> we have large pronounced gap of about 1.3 MeV from the next 11/2<sup>+</sup> level. This is reproduced beautifully by both the interactions. However position and ordering of next two higher levels 11/2<sup>+</sup> and 13/2<sup>+</sup> are found with good agreement from calculations. We have many more levels as compared to the levels experimentally predicted in this energy domain.

Fig. 7.7 compares the experimental [117] and theoretical low lying states of  $^{105}\text{Sn}$  and corresponding excitation energies are tabulated in Table 7.7. As seen from the figure, we see that all the states up to 2.5 MeV are reproduced by the theory. Our calculations predicts 5/2<sup>+</sup> ground state and a close lying 7/2<sup>+</sup> state at 139 and 141 keV from both the calculations. In comparison to the previous work by Schubert *et*

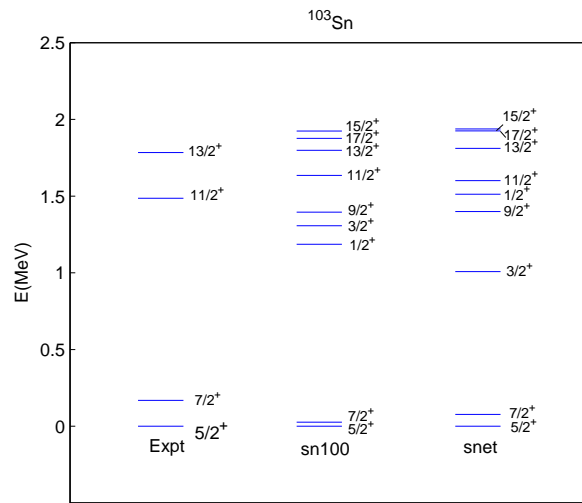


Figure 7.7: Experimental[116] and calculated energy levels of  $^{103}\text{Sn}$  with sn100pn and snet interactions.

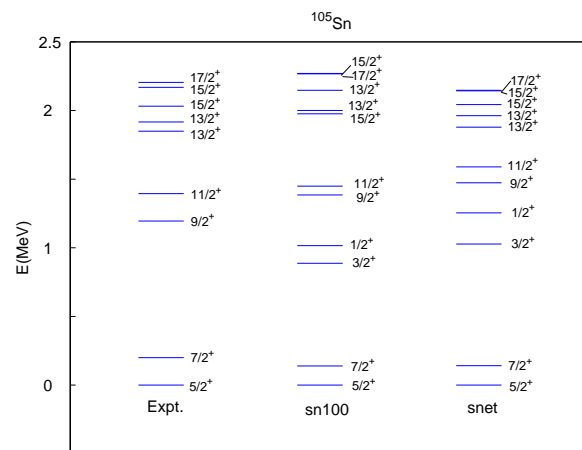


Figure 7.8: Same as Fig. 7.7 for  $^{105}\text{Sn}$ .

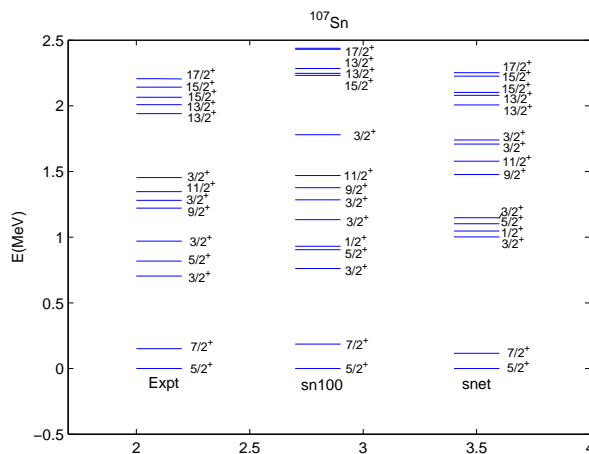
Table 7.7: Experimental [117] and theoretical low-lying states (up to 2.5 MeV) of  $^{105}\text{Sn}$ . Energies are in MeV.

$J^\pi$	Exp.	$J^\pi$	sn100	$J^\pi$	snet
(5/2 <sup>+</sup> )	0.000	5/2 <sup>+</sup>	0.000	5/2 <sup>+</sup>	0.000
(7/2 <sup>+</sup> )	0.200	7/2 <sup>+</sup>	0.139	7/2 <sup>+</sup>	0.141
(9/2 <sup>+</sup> )	1.195	3/2 <sup>+</sup>	0.887	3/2 <sup>+</sup>	1.027
(11/2 <sup>+</sup> )	1.394	5/2 <sup>+</sup>	0.942	3/2 <sup>+</sup>	1.144
(13/2 <sup>+</sup> )	1.849	1/2 <sup>+</sup>	1.016	5/2 <sup>+</sup>	1.199
(13/2 <sup>+</sup> )	1.916	3/2 <sup>+</sup>	1.177	1/2 <sup>+</sup>	1.254
(15/2 <sup>+</sup> )	2.031	9/2 <sup>+</sup>	1.385	1/2 <sup>+</sup>	1.450
(15/2 <sup>+</sup> )	2.168	11/2 <sup>+</sup>	1.449	9/2 <sup>+</sup>	1.473
(17/2 <sup>+</sup> )	2.204	1/2 <sup>+</sup>	1.501	7/2 <sup>+</sup>	1.500
-	-	7/2 <sup>+</sup>	1.553	9/2 <sup>+</sup>	1.579
-	-	9/2 <sup>+</sup>	1.692	11/2 <sup>+</sup>	1.589
-	-	15/2 <sup>+</sup>	1.976	13/2 <sup>+</sup>	1.878
-	-	13/2 <sup>+</sup>	2.000	13/2 <sup>+</sup>	1.962
-	-	11/2 <sup>+</sup>	2.066	11/2 <sup>+</sup>	2.017
-	-	13/2 <sup>+</sup>	2.147	15/2 <sup>+</sup>	2.043
-	-	17/2 <sup>+</sup>	2.267	15/2 <sup>+</sup>	2.143
-	-	-	-	17/2 <sup>+</sup>	2.147

al. [100], our calculations have clear one to one correspondence up to 15/2<sup>+</sup> from the experimental data.

In Table 7.8 we have listed experimental and theoretical low lying states of  $^{107}\text{Sn}$  and corresponding levels are drawn in Fig. 7.8. We have extended the calculations recently performed by Dikmen to higher spin states. Dikmen has performed the shell-model calculations for low lying levels using CD Bonn potential and Nijmegen interactions and it is observed that using sn100pn interaction we have much better agreement for low lying states, whereas for levels above 11/2<sup>+</sup>, ordering is well reproduced but values are slightly over predicted. However calculations performed by snet interaction are able to explain only low-lying states but for higher lying levels we have to retune the TBME or readjust the single particle energies.

Fig. 7.10 shows the calculated excitation energies of first excited 7/2<sup>+</sup> state for odd A Sn isotopes (103 to 107), with the experimental data. We see that the behavior of energy as a function of mass number (A) is quite satisfactory except for  $^{103}\text{Sn}$  where from calculations this level is under predicted. The overall agreement between theory and the experiment is satisfactory.

Figure 7.9: Same as Fig. 7.7 for  $^{107}\text{Sn}$ .Table 7.8: Experimental [118, 26] and theoretical low-lying states (up to 2.5 MeV) of  $^{107}\text{Sn}$ . Energies are in MeV.

$J^\pi$	Exp.	$J^\pi$	sn100	$J^\pi$	snet
(5/2 <sup>+</sup> )	0.000	5/2 <sup>+</sup>	0.000	5/2 <sup>+</sup>	0.000
(7/2 <sup>+</sup> )	0.151	7/2 <sup>+</sup>	0.186	7/2 <sup>+</sup>	0.116
(3/2 <sup>+</sup> )	0.704	3/2 <sup>+</sup>	0.761	3/2 <sup>+</sup>	1.002
(5/2 <sup>+</sup> )	0.818	5/2 <sup>+</sup>	0.905	1/2 <sup>+</sup>	1.047
(3/2 <sup>+</sup> )	0.970	1/2 <sup>+</sup>	0.931	5/2 <sup>+</sup>	1.102
(9/2 <sup>+</sup> )	1.221	3/2 <sup>+</sup>	1.133	3/2 <sup>+</sup>	1.148
(3/2 <sup>+</sup> )	1.280	3/2 <sup>+</sup>	1.284	7/2 <sup>+</sup>	1.453
(11/2 <sup>+</sup> )	1.347	9/2 <sup>+</sup>	1.377	9/2 <sup>+</sup>	1.477
(3/2 <sup>+</sup> )	1.454	7/2 <sup>+</sup>	1.445	11/2 <sup>+</sup>	1.578
(13/2 <sup>+</sup> )	1.941	11/2 <sup>+</sup>	1.469	9/2 <sup>+</sup>	1.579
(13/2 <sup>+</sup> )	2.009	9/2 <sup>+</sup>	1.638	3/2 <sup>+</sup>	1.709
(15/2 <sup>+</sup> )	2.065	3/2 <sup>+</sup>	1.780	3/2 <sup>+</sup>	1.740
(15/2 <sup>+</sup> )	2.142	11/2 <sup>+</sup>	2.189	13/2 <sup>+</sup>	2.007
(17/2 <sup>+</sup> )	2.206	15/2 <sup>+</sup>	2.232	13/2 <sup>+</sup>	2.080
-	-	13/2 <sup>+</sup>	2.247	15/2 <sup>+</sup>	2.102
-	-	13/2 <sup>+</sup>	2.284	15/2 <sup>+</sup>	2.226
-	-	17/2 <sup>+</sup>	2.430	17/2 <sup>+</sup>	2.252
-	-	15/2 <sup>+</sup>	2.438	-	-

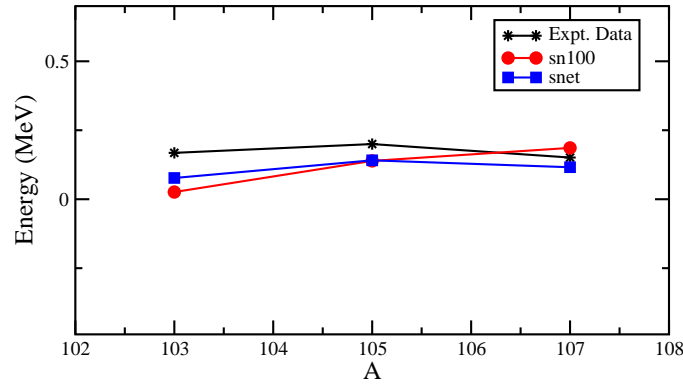


Figure 7.10: Comparison of energy of the first  $7/2^-$  excited state from shell model calculations with experimental data for odd Sn isotopes with A ranging from 103 to 107.

## 7.5 Electromagnetic transition strengths

In a quantum-mechanical treatment of a radiating system, the multipole moments of the charge, current and magnetization of the emitting system are replaced by matrix elements of corresponding operators between the initial and final states of the system.

The electric multipoles are defined as

$$B(el, L) = \frac{1}{2J_i + 1} \left| \langle J_f || \frac{1}{e} \sum_i e_i r_i^L Y_L(\theta_i \phi_i) || J_i \rangle \right|^2 \quad (7.7)$$

where L is the sum of orbital and intrinsic angular momenta,  $J_i$  and  $J_f$  are the initial and final state spins respectively. thus B(E2) in unit of  $e^2 \text{fm}^{2L}$  becomes

$$B(el, L) = \frac{1}{2J_i + 1} \left| \langle J_f || \frac{1}{e} \sum_i e_i r_i^2 Y_2(\theta_i \phi_i) || J_i \rangle \right|^2 \quad (7.8)$$

The reduced transition probabilities  $B(E2; 0_{g.s}^+ \rightarrow 2_1^+)$ , obtained from calculations are shown in column 3 and 4 of Table 7.9. and compared with recently observed experimental data [28, 30]. The neutron effective charge used in calculations is 1.0e, same as used in Refs. [28, 30]. Concept of effective charge is related to the degree of rigidity of the spherical equilibrium shape of the doubly-closed shell nucleus and thus, is especially sensitive to the excitation energy and decay rate of the lowest  $2^+$  state of the core nucleus. The results obtained from both the interactions have almost similar pattern and increase in  $B(E2)$  values have been observed with increasing the neutron number, which is signature for enhance in collectivity.

Table 7.9: Comparison of the yrast  $B(E2; 0_{g.s.}^+ \rightarrow 2_1^+)$  values, obtained from the shell-model calculations with the measured values in  $e^2b^2$  for even Sn isotopes. The experimental values have been taken from [30, 28]

Isotope	$B(E2, 0_{g.s.}^+ \rightarrow 2_1^+)[e^2b^2]$		
	Exp.	sn100pn	snet
$^{102}\text{Sn}$	-	0.039	0.041
$^{104}\text{Sn}$	-	0.090	0.083
$^{106}\text{Sn}$	0.240	0.138	0.116
$^{108}\text{Sn}$	0.230	0.176	0.170

## 7.6 Conclusion

We have presented here some results of large basis of shell-model calculations for the neutron deficient Sn isotopes. We have made use of effective interaction of Brown obtained by re normalization of Bonn and Paris nucleon nucleon interaction. It is observed that agreement with the experimental data is better for even Sn isotopes compared to that for odd one. More experimental data below 5 MeV is needed for better assessment of the calculations. Electromagnetic transition rates are also a sensitive tool for the test of nuclear wave functions. Together it would lead to better understanding of the role of modern realistic interactions in the shell-model approach to the nuclear many body problem.

# Chapter 8

## Summary and Future Perspective

### 8.1 Summary

In the present work, the aim was to understand the structural features that result from interplay between single particle and collective degrees of freedom. Such studies provide an opportunity to investigate a variety of phenomenon resulting from simultaneous excitation of nucleons across the shell closure. Keeping this in view, experimental studies have been carried out for  $^{75}\text{Kr}$  and  $^{75}\text{Br}$  and theoretical calculations in the the frame work of large scale shell model have been performed for  $^{102-108}\text{Sn}$  isotopes.

Excited state in  $^{75}\text{Kr}$  were investigated through in beam  $\gamma$ -ray spectroscopy techniques following its population in the  $^{50}\text{Cr}(^{28}\text{Si},2\text{pn})$  fusion-evaporation reaction at beam energy 90 MeV. The previously known level scheme have also been verified in the present work. In  $^{75}\text{Kr}$  both positive and negative parity bands are strongly connected with strong M1 transitions. Lifetimes of high-spin states of such coupled bands have been reported in the present work using the Doppler-shift attenuation method (DSAM). The lifetime measurements of the both positive and negative parity bands were extended after the band crossing. Transitional quadrupole moments  $Q_t$  determined from lifetimes of the yrast positive and negative parity bands show near constant behavior up to the band crossing followed by slight reduction in collectivity in the band crossing region which is an indication of the shape change. In particular, the yrast positive parity band of  $^{75}\text{Kr}$  was found to have large  $Q_t$  compared to the negative parity bands, showing the larger deformation. The properties of these bands observed

up to high-spins are compared with those obtained using projected shell-model (PSM). It is found that  $Q_t$  have rather similar values at low-spins. However at high spins particularly after the 1-qp and 3-qp band crossing,  $Q_t$  decreases. The drop in  $Q_t$  around spins  $I = 25/2$  for the positive parity band is interpreted as the effect of band crossing of 3 quasi-particle bands based on  $\nu 5/2[402] \oplus \pi 1/2[400] \oplus \pi 3/2[402]$  with the ground band based on  $\nu 5/2[402]$ . This behavior is supported by Total Routhian Surface (TRS) calculations. The TRS calculations for positive parity bands show a stable minima at prolate deformation ( $\gamma = 0^\circ$ ) which gets shifted towards less deformed nearly prolate shape after the band crossing at the same frequency where transition quadrupole moment decreases. Similar variations are exhibited in the negative-parity band.

High spin states in proton rich odd A,  $^{75}\text{Br}$  were investigated in the same experiment using  $^{50}\text{Cr}(^{28}\text{Si}, 3p)^{75}\text{Br}$  reaction at 90 MeV. The transitions reported in Ref. [94] were identified in our experiment, too. The lifetimes of high-spin states upto highest possible states, beyond the band crossing, in yrast positive and negative-parity bands as well as high K bands have been determined using DSAM technique. Instead, lifetime of some lower transitions were measured using gate above the transition of interest. It was observed that the  $Q_t$  of the yrast positive and negative-parity bands of  $^{75}\text{Br}$  determined from lifetime, remain almost constant before the proton or neutron alignment which decreases abruptly after the band crossing indicating the reduction in collectivity. Reduction in collectivity is more pronounced in case of negative parity bands as compared to the positive-parity band. This decrease was interpreted as change in deformation parameters  $\beta$  and  $\gamma$  due to alignments of proton / neutron obtained from TRS calculations. In case of positive-parity band, the  $g_{9/2}$  proton crossing is Pauli blocked and hence the effect of neutron crossing is an important factor to see the evolution of shapes in this band. Whereas, in case of the negative parity band both proton as well as neutron  $g_{9/2}$  alignment are possible. Decrease in the  $Q_t$  in both the bands are due to these alignments and can be seen consistently with the theoretically calculated TRS plots which show change in shape parameters  $\beta_2$  and  $\gamma$ . Experimentally observed  $Q_t$  is also compared with projected shell-model calculations and results are in good agreement. In case of positive parity band the  $Q_t$  values drop rather suddenly near the

region of neutron alignment, then rise again after the alignment to an average value somewhat smaller than below the alignment whereas in case of negative parity band general trend of decreasing  $Q_t$  with spin is supported by PSM calculations.

The lifetimes of additional high K bands in both positive and negative parity bands were also measured for the first time in this work for this particular nucleus. No significant signature of further alignment is seen in these bands.

The structure of positive parity band of  $A = 75$ , Krypton and Bromine nuclei are dominated by  $N = Z = 34, 36$  oblate shell gaps. For  $N = 39$  nuclei, alignment of  $g_{9/2}$  proton take place and for  $N = 40$ , neutron alignment has been seen. But in both cases  $Q_t$  remains constant before band crossing and then reduces slightly after the band crossing showing change in shape after the band crossing. It means that the effect of  $\pi g_{9/2}$  and  $\nu g_{9/2}$  alignments have similar effect on the shape transition of these nuclei. However, some more experimental data points are required after the band crossing in  ${}^{75}Kr$  to draw any conclusion for the effect of neutron or proton alignments in case of negative-parity bands of these nuclei.

Neutron deficient nuclei near the  $Z = 50$  shell closure exhibit many exciting features involving regular band structures arising from the occupancy of the valance protons and neutrons in  $g_{9/2}$  and  $h_{11/2}$  orbitals, respectively. In the present theoretical work, large scale shell model calculations have been performed on proton rich  ${}^{102-108}Sn$  isotopes. The modern large-scale shell-model calculations give at present the most accurate and comprehensive description of nuclei including those at very proton-rich or very neutron-rich edges. It can predict not only low-lying energy levels but can also successfully make most important theoretical predictions for comparison with the experimental findings. We have studied proton rich Sn isotopes in the framework of nuclear shell model for sdgh model space using two different types of effective interactions obtained from renormalized Bonn and Paris nucleon nucleon interaction. For diagonalization of matrices shell model code Nushell was used. The energy levels calculated for even and odd Sn isotopes are compared with experimentally observed levels and the ordering of the levels is correctly reproduced. The agreements with the experiential data is slightly

better for even Sn isotopes compared to the odd ones. The energies of first excited ( $2^+$ ) state are calculated and compared with the recent available data and almost constant spacing is found for both the interactions which agrees well with the experimentally obtained data. Transition probability  $B(E2)$  are also reported and compared with the experimental data wherever available. The agreement is very good for both the interactions.

## 8.2 Future Perspective

Atomic nucleus is a fundamental and unique laboratory of the nature for investigating the relationships among the fundamental forces as well as the symmetry principles of all physical phenomena. Today research on nuclear physics focuses on exploring nucleonic matter under extreme conditions of energy, temperature and that can be possible with the help of modern accelerator laboratories. In recent past, many exotic nuclear phenomena have been observed like shape co-existence, identical bands, band termination, chirality in nuclear rotation, magnetic rotation, super deformation and hyperdeformation through out the nuclear landscape. The discovery of these phenomena are closely related to technological development of detector and accelerator. The development of HPGE  $\gamma$  detectors brought renaissance in  $\gamma$ -ray spectroscopy because of the large improvement in energy resolution. Most of the present day  $\gamma$ -ray detection system like GAMMASPHERE [20], EUROGAM [21] and INGA [22] are made of these detectors as well as composite Ge detectors. Right now major effort has started around the world to make more sophisticated detector arrays in terms both efficiency and sensitivity. New proposed tracking arrays like AGATA and GRETA are supposed to have highly segmented Ge detectors covering close to the full  $4\pi$  solid angle.

Although this experimental work along with theoretical calculations has contributed to improve our knowledge of shape evolution at high spin states, more effort has to be put into the study of other proton or neutron-rich nuclei far from stability at higher spins in this mass region. Since nuclei in this mass region, show most of the above mentioned nuclear structure phenomena, more experimental as well as theoret-

ical studies are needed for better understanding of these exciting features in the light of future facilities.

Theoretical shell model calculations have been performed near the  $^{100}\text{Sn}$  region where the experimental data is scarce due to difficulty in populating these nuclei experimentally with present resources. The present work can be extended with the advent of these tracking arrays and radioactive ion beam facilities.

## List of Publications

### I] International Journals:

1. Shape evolution of the highly deformed  $^{75}\text{Kr}$  nucleus examined with the Doppler-shift attenuation method;  
**T. Trivedi**, R. Palit, D. Negi, Z. Naik, Y.-C. Yang, Y. Sun, J. A. Sheikh, A. Dhal, M. K. Raju, S. Appannababu, S. Kumar, D. Choudhury, K. Maurya, G. Mahanto, R. Kumar, R. P. Singh, S. Muralithar, A. K. Jain, H. C. Jain, S. C. Pancholi, R. K. Bhowmik, and I. Mehrotra,  
**Phys. Rev. C** **80**, 047302 (2009).
2. Lifetime measurement of high spin states in  $^{75}\text{Kr}$ ;  
**T. Trivedi**, D. Negi, R. Palit, Z. Naik, A. Dhal, M. K. Raja, A. Babu, S. Kumar, D. Choudhury, K. Maurya, G. Mahanto, R. Kumar, R. P. Singh, S. Muralithar, A. K. Jain, H. C. Jain, S. C. Pancholi, R. K. Bhowmik and I. Mehrotra,  
**Nucl. Phys. A** (to be published).
3. Shape evolution of highly deformed  $^{75}\text{Kr}$  and projected shell model description; Ying-Chun Yang, Yang Sun, **T. Trivedi**, R. Palit, J. A. Sheikh,  
**International Journal of Modern Physics E** (to be published).
4. The structure of  $^{136}\text{Ba}$  using HI reaction;  
 Suresh Kumar, A.K. Jain, Alpana Goel, S. S. Malik, R. Palit, H. C. Jain, I. Mazumdar, P. K Joshi, Z. Naik, A. Dhal, **T. Trivedi**, I. Mehrotra, A. Babu, L. Chaturvedi, V. Kumar, R. Kumar, D. Negi, R.P. Singh, S. Muralithar, R.K. Bhowmik, S.C. Pancholi,  
**Submitted to Phys. Rev. C**.
5. Indian National Gamma Array in Beam Hall II at IUAC;  
 S. Muralithar, Kusum Rani, Rakesh Kumar, R.P. Singh, J.J. Das, J. Gehlot, K.S. Golda, A. Jhingan, N. Madhavan, S. Nath, P.Sugathan, T. Varughese, M. M. Archunan, P. Barua, Arti Gupta, Mamta Jain, Ashok Kothari, B.P. Ajith Kumar,

A. J. Malyadri, U. G. Naik, Raj Kumar, Rajesh Kumar, S. Rao, S.K. Saini, S.K.Suman, E.T. Subramaniam, S. Venkataramanan, A. Dhal, G. Jnaneswari, D. Negi, K. Raja, **T. Trivedi**, and R. K. Bhowmik,

**Submitted to Nucl. Instru. Meth. (A).**

6. Multi-particle alignment in  $^{75}\text{Br}$  and emergence of triaxiality;

**T. Trivedi**, R. Palit, D. Negi, Z. Naik, Y.-C. Yang, Y. Sun, J. A. Sheikh, A. Dhal, M. K. Raju, S. Appannababu, S. Kumar, D. Choudhury, R. Kumar, R. P. Singh, S. Muralithar, A. K. Jain, H. C. Jain, S. C. Pancholi, R. K. Bhowmik, and I. Mehrotra,

**To be communicated.**

7. Shell model description of neutron deficient Sn isotopes;

**T. Trivedi** and I. Mehrotra,

**To be communicated.**

8. High spin structures in  $^{107}\text{In}$ ;

D. Negi, **T. Trivedi**, A. Dhal, S. Roy, V. Kumar, S. Kumar, M.K. Raju, S. Appanna Babu, G. Mohanto, J. Kaur, R.K. Sinha, R. Kumar, R.P. Singh, S. Muralithar, A.K. Bhati, S.C. Pancholi, R.K. Bhowmik,

**To be communicated.**

## II] International Conferences/Symposium:

1. Lifetime measurement of high spin states in  $^{75}\text{Kr}$ ;

**T. Trivedi**, D. Negi, R. Palit, Z. Naik, A. Dhal, M. K. Raja, A. Babu, S. Kumar, D. Choudhury, K. Maurya, G. Mahanto, R. Kumar, R. P. Singh, S. Muralithar, A. K. Jain, H. C. Jain, S. C. Pancholi, R. K. Bhowmik and I. Mehrotra, NN2009, Beijing, China, August 16-21, 2009.

2. Lifetime measurement of high spin states in  $^{75}\text{Br}$  through Doppler-shift attenuation method;

**T. Trivedi**, R. Palit, D. Negi, A. Dhal, M. K. Raja, S. Kumar, R. Kumar, R. P.

Singh, S. Muralithar, S. C. Pancholi, R. K. Bhowmik and I. Mehrotra,  
 APSORC'09, Nepa, USA, November 29 - December 4, 2009.

3. Complete and incomplete fusion in  ${}^9\text{Be}+{}^{124}\text{Sn}$  system;  
 V. V. Parkar, R. Palit, S. Sharma, B. S. Naidu, P. K. Joshi, S. Santra, P. K. Rath, K. Ramachandran, K. Mahata, **T. Trivedi**, A. Raghav  
 APSORC'09, Nepa, USA, November 29 - December 4, 2009.

### III] DAE Symposiums(International/National) :

1. Shape transition in  ${}^{75}\text{Kr}$  and  ${}^{75}\text{Br}$  nuclei;  
**T. Trivedi**, R. Palit, D. Negi, Z. Naik, Y. -C Yang, Y. Sun, J. A. Sheikh, A. Dhal, M. K. Raju, S. Appannababu, S. Kumar, D. Choudhury, K. Marya, G. Mahanto, R. Kumar, R. P. Singh, S. Muralithar, A. K. Jain, H. C. Jain, S. C. Pancholi, R. K. Bhowmik, I. Mehrotra,  
 Proc. DAE-BRNS Symp. on Nucl. Phys. **54**, 60 (2009).
2. High spin structures in  ${}^{107}\text{In}$ ;  
 D. Negi, **T. Trivedi**, A. Dhal, S. Roy, V. Kumar, S. Kumar, M.K. Raju, S. Appanna Babu, G. Mohanto, J. Kaur, R.K. Sinha, R. Kumar, R.P. Singh, S. Muralithar, A.K. Bhati, S.C. Pancholi, R.K. Bhowmik,  
 Proc. DAE-BRNS Symp. on Nucl. Phys. **54**, 68 (2009).
3. Shape behavior at high spin in  ${}^{137}_{61}\text{Pm}$ ; A. Dhal, R.K. Sinha, D. Negi, **T. Trivedi**, M.K. Raju, D. Choudhury, G. Mahanto, S. Kumar, J. Gehlot, R. Kumar, S. Nath, S.S. Ghugre, R.P. Singh, J.J. Das, S. Muralithar, N. Madhavan, J.B. Gupta, A.K. Sinha, A.K. Jain, I.M. Govil, R.K. Bhowmik, S.C. Pancholi, L. Chaturvedi,  
 Proc. DAE-BRNS Symp. on Nucl. Phys. **54**, 92 (2009).
4. Shape Co-existence in  ${}^{135}_{56}\text{Ba}_{79}$ ; Suresh Kumar, A.K. Jain, Alpana Goel, S. S. Malik, R. Palit, H. C. Jain, I. Mazumdar, P. K Joshi, Z. Naik, A. Dhal, **T. Trivedi**, I. Mehrotra, A. Babu, L. Chaturvedi, V. Kumar, R. Kumar, D. Negi, R.P. Singh, S. Muralithar, R.K. Bhowmik, S.C. Pancholi,  
 Proc. DAE-BRNS Symp. on Nucl. Phys. **54**, 90 (2009).

5. Search for anti-magnetic rotation in  $^{105}\text{Cd}$ ; Deepika Choudhury, Monika Patial, Neha Gupta, A.K. Jain, P. Arumugam, S.C. Pancholi, Anukul Dhal, R.K. Sinha, L. Chaturvedi, P.K. Joshi, R. Palit, Suresh Kumar, Ritika Garg, Samit Mandal, **T. Trivedi**, Indra Mehrotra, Alpana Goel, Dinesh Negi, Gayatri Mohanto, R.K. Bhowmik, S. Muralithar, R.P. Singh, N. Madhavan, Proc. DAE-BRNS Symp. on Nucl. Phys. **54**, 66 (2009).
6. Complete and incomplete fusion cross-sections in  $^9\text{Be}+^{124}\text{Sn}$  system and its implications in horizontal spectroscopy; V.V. Parkar, R. Palit, S. Sharma, B.S. Naidu, S. Santra, P.K. Joshi, P.K. Rath, K. Mahata, K. Ramachandran, **T. Trivedi**, A. Raghav, Proc. DAE-BRNS Symp. on Nucl. Phys. **54**, 320 (2009).
7. Fusion studies of weakly bound bound  $^6\text{Li}$  nucleus with  $^{90}\text{Zr}$  near Coulomb barrier; H. Kumawat, A. K. Mohanty, K. Mahata, A. Chatterji, R. K. Choudhury, S. Kailash, V. V. Parkar, R. Palit, **T. Trivedi**, Proc. DAE-BRNS Symp. on Nucl. Phys. **54**, 308 (2009).
8. Spectroscopy of neutron-rich tellurium nuclei; M.K. Raju, T.S. Reddy, B.S. Reddy, A. Dhal, D. Negi, **T. Trivedi**, G. Jnaneswari, A. Kumar, A.K. Sinha, S.S. Gughre, I. Mazumdar, S. Muralithar, S. Nath, P. Sugathan, J.J. Das, R.P. Singh, R. Kumar, N. Madhavan, R.K. Bhowmik, S. Kailas, U. Garg, P.V. Madhusudhana Rao, Proc. DAE-BRNS Symp. on Nucl. Phys. **54**, 80 (2009).
9. Preparation of Multilayer Calcium Target; Dinesh Negi, **T. Trivedi**, A. Babu, K. Raja, S. Kumar, A.K. Bhati, R.K. Bhowmik, J.J. Das, Abhilash, D. Kabiraj, S. Muralithar, R.P. Sigh, R. Kumar, S.C. Pancholi, Proc. DAE-BRNS Symp. on Nucl. Phys. **53**, 703 (2008).
10. High Spin States in  $^{137}\text{Pm}$ ; A. Dhal, R.K. Sinha, D. Negi, **T. Trivedi**, M. K. Raja, S. Kumar, G. Jnaneswari,

- D. Choudhury, G. Mahanto, J. Gehlot, R. Kumar, S. Nath, S. S. Ghugre, R. P. Singh, J.J.Das, S. Muralithar, N. Madhavan, J. B. Gupta, A. K. Sinha, A. K. Jain, I. M. Govil, R. K. Bhowmik, S. C. Pancholi, L. Chaturvedi,  
Proc. DAE-BRNS Symp. on Nucl. Phys. **53**, 221 (2008).
11. Investigation of Positive Parity Degenerate Dipole Bands in  $^{133}\text{Ce}$ ;  
R. Palit, V. V. Parkar, Z. Naik, H. C. Jain, P. K. Joshi, I. Mazumdar, A. Y. Deo, S. Sihotra, S. Kumar, S. Mandal, D. Mehta, D. Choudhury, A. K. Jain, D. Negi, **T. Trivedi**, S. Muralithar, R. P. Singh, Rakesh Kumar, N. Madhavan, R. K. Bhowmik,  
Proc. DAE-BRNS Symp. on Nucl. Phys. **53**, 323 (2008).
12. Indian National Gamma Array in Beam Hall II at IUAC;  
S. Muralithar, Kusum Rani, Rakesh Kumar, R.P. Singh, J.J. Das, J. Gehlot, K.S. Golda, A. Jhingan, N. Madhavan, S. Nath, P.Sugathan, T. Varughese, M. M. Archunan, P. Barua, Arti Gupta, Mamta Jain, Ashok Kothari, B.P. Ajith Kumar, A. J. Malyadri, U. G. Naik, Raj Kumar, Rajesh Kumar, S. Rao, S.K. Saini, S.K.Suman, E.T. Subramaniam, S. Venkataramanan, A. Dhal, G. Jnaneswari, D. Negi, K. Raja, **T. Trivedi**, and R. K. Bhowmik,  
Proc. DAE-BRNS Symp. on Nucl. Phys. **53**, 689 (2008).
13. High spin states in  $^{155}\text{Ho}$ ;  
G. Jnaneswari, S. Lakshminarayan, A.K. Jain, Deepika Choudhury, D. Rudolph , I.Ragnarsson, A .V. Ramayya, J.H. Hamilton, J.C. BatchelderAlpana Goel,L.Chaturvedi, Suresh Kumar, S.C. Pancholi, R.K.Bhowmik, S.Muralithar, N. Madhavan,R.P.Singh, R. Kumar, Dinesh Negi, Gayatri Mohanto, **Tarkeswar Trivedi**,  
Proc. DAE-BRNS Symp. on Nucl. Phys. **53**, 271 (2008).
14. The structure of  $^{136}\text{Ba}$  using HI reaction;  
Suresh Kumar, A.K.Jain, **T. Trivedi**, I. Mehrotra, et at.  
Proc. DAE-BRNS Symp. on Nucl. Phys. **52**, 292 (2007).
15. Lifetime measurement of  $^{75}\text{Br}$  with inverse kinematics ;

Dinesh Negi, V.kumar, **T. Trivedi** *et al.*

Proc. DAE-BRNS Symp. on Nucl. Phys. **52**, 191 (2007).

16. Structure of neutron deficient Sn isotopes;

**T. Trivedi**, I. Mehrotra,

Proc. DAE-BRNS Symp. on Nucl. Phys. **51**, 288 (2006).

# Bibliography

- [1] S. L. Tabor, P. D. Cottle, J. W. Holcomb, T. D. Johnson, P. C. Womble, S. G. Buccino, and F. E. Durham, *Phys. Rev.* **C41**, 2658 (1990).
- [2] J. Heese, D. J. Blumenthal, A. A. Chishti, P. Chowdhury, B. Crowell, P. J. Ennis, C. J. Lister, , and C. Winter, *Phys. Rev.* **C43**, R921 (1991).
- [3] G. D. Johns, J. Dring, J. W. Holcomb, T. D. Johnson, M. A. Riley, G. N. Sylvan, P. C. Womble, V. A. Wood, , and S. L. Tabor, *Phys. Rev.* **C50**, 2786 (1994).
- [4] R. Palit, H. C. Jain, P. K. Joshi, J. A. Sheikh, , and Y. Sun, *Phys. Rev.* **C63**, 024313 (2001).
- [5] S. Skoda, F. Becker, T. Burkardt, J. Eberth, S. Freund, U. Hermkens, T. Mylaeus, R. Sefzig, W. Teichert, A. von der Werth, et al., *Nucl. Phys.* **A633**, 565 (1998).
- [6] J. Dring, G. D. Johns, R. A. Kaye, M. A. Riley, S. L. Tabor, P. C. Womble, and J. X. Saladin, *Phys. Rev.* **C52**, R2284 (1995).
- [7] R. Schwengner, J. Dring, L. Funke, G. Winter, A. Johnson, and W. Nazarewicz, *Nucl. Phys.* **A509**, 550 (1991).
- [8] T. D. Johnson, J. W. Holcomb, P. C. Womble, P. D. Cottle, S. L. Tabor, F. E. Durham, S. G. Buccino, and M. Matsuzaki, *Phys. Rev.* **42**, 2418 (1990).
- [9] C. Plettner *et al.*, *Phys. Rev.* **C62**, 014313 (2000).
- [10] J. H. Hamilton, A. V. Ramayya, W. T. Pinkston, R. M. Ronningen, G. Garcia-Bermudez, H. K. Carter, R. L. Robinson, H. J. Kim, , and R. O. Sayer, *Phys. Rev. Lett.* **32**, 239 (1974).

- [11] W. Nazarewicz, J. Dudek, R. Bengtsson, T. Bengtsson, and I. Ragnarsson, Nucl. Phys. **A435**, 397 (1985).
- [12] J. Cederkall *et al.*, Eur. Phys. J. **A1**, 7 (1998).
- [13] D. Sohler *et al.*, Eur. Phys. J. **A 16**, 171 (2003).
- [14] M. Gierlik *et al.*, Nucl. Phys. **A724**, 313 (2003).
- [15] M. Lipoglavsek, C. Baktash, M. P. Carpenter, D. J. Dean, T. Engeland, C. Fahlander, M. Hjorth-Jensen, R. V. F. Janssens, A. Likar, J. Nyberg, et al., Phys. Rev. **C65**, 021302 (2002).
- [16] M. Lipoglavsek *et al.*, Phys. Rev. **C63**, 021307 (2001).
- [17] D. Negi, T. Trivedi, A. Dhal, S. Kumar, V. Kumar, S. Roy, M. Raju, S. A. Babu, G. Mohanto, J. Kaur, et al., Proc. DAE-BRNS Symp. on Nucl. Phys. **54** (2009).
- [18] S. Frauendorf, Rev. Mod. Phys. **73**, 463 (2001).
- [19] R. M. Clark and A. O. Macchiavelli, Annu. Rev. Nucl. Part. Sci. **50**, 1 (2000).
- [20] I. Y. Lee, Nucl. Phys. **A520**, 641c (1990).
- [21] J. Simpson, Z. Phys. **A358**, 139 (1997).
- [22] S. Muralithar, K. Rani, R. Kumar, R. P. Singh, J. J. Das, J. Gehlot, K. S. Golda, A. Jhingan, N. Madhavan, S. Nath, et al., Proc. DAE-BRNS Symp. on Nucl. Phys. **53**, 307 (2008).
- [23] D. R. LaFosse, C. J. Chiara, D. B. Fossan, G. J. Lane, J. M. Sears, J. F. Smith, K. Starosta, A. J. Boston, E.S.Paul, A. T. Semple, et al., Phys. Rev. **C62**, 014305 (2000).
- [24] A. V. Afanasjev and I. Ragnarsson, Nucl.Phys. **A628**, 580 (1998).
- [25] S. D. Robinson, S. J. Freeman, D. P. Balamuth, M. Carpenter, M. Devlin, B. G. Dong, J. L. Durell, P. Hausladen, D. R. LaFosse, T. Lauritsen, et al., J. Phys. **G28**, 1415 (2002).

- [26] J. J. Ressler, W. B. Walters, D. S. Brenner, C. N. Davids, A. Heinz, G.-L. Poli, J. Shergur, , and D. Seweryniak, Phys. Rev. **C65**, 044330 (2002).
- [27] M. Karny *et al.*, Eur. Phys. J. **A27**, 129 (2006).
- [28] A. Banu *et al.*, Phys. Rev. **C72**, 061305(R) (2005).
- [29] H.J. Wollersheim *et al.*, Nucl. Instr. Meth. **A537**, 637 ((2005).
- [30] C. Vaman *et al.*, Phys. Rev. Lett. **99**, 162501 (2007).
- [31] A. Ekstrom *et al.*, Phys. Rev. Lett. **101**, 012502 (2008).
- [32] M. G. Mayer, Phys. Rec. **75**, 1969 (1949).
- [33] M. G. Mayer and J. H. D. Jensen, *Elementary Theory of Nuclear Shell Structure* (John Wiley and Sons., New York, 1955).
- [34] M. K. Pal, *Theory of Nuclear Structure* (East - West press pvt. Ltd., New Delhi, 1982).
- [35] D. L. Hill and J. A. Wheeler, Phys. Rev. **89**, 1102 (1953).
- [36] S. G. Nilsson, Mat. Fys. Medd. Dan. Vid. Selsk. **29**, No.16 (1954).
- [37] S. G. Nilsson and Ragnarsson, *Shape and Shells in Nuclear Structure* (Combridge University Press, New York, 1995).
- [38] V. M. Strutinsky, Nucl. Phys. **A95**, 420 (1967).
- [39] V. M. Strutinsky, Nucl. Phys. **A112**, 1 (1968).
- [40] D. R. Inglis, Phys. Rev. **96**, 1059 (1954).
- [41] D. R. Inglis, Phys. Rev. **97**, 701 (1955).
- [42] R. Bengtsson and S. Frauendorf, Nucl. Phys. **A327**, 139 (1979).
- [43] R. Bengtsson and I. Ragnarsson, Nucl. Phys. **A436**, 14 (1985).
- [44] J. Elliott, Proc. Roy. Soc. **245**, 128 and 557 (1968).

- [45] A. Bohr and B. R. Mottelson, *Nuclear Structure Vol.I, Appendix 1A* (Benjamin, Inc., 1969).
- [46] Y. Sun and J. Egido, Nucl. Phys. **580**, 1, (1994).
- [47] Y. Sun, S. Wen, and D. Feng, Phys. Rev. Lett. **72**, 3483, (1994).
- [48] K. Hara and Y. Sun, Int. J. Mod.Phys. **E4**, 637 (1995).
- [49] G. K. Mehta and A. P. Patro, Nucl. Instru. Meth. **A 268**, 234 (1988).
- [50] P. K. Joshi, H. C. Jain, A. S. Medhi, S. Chattopadhyay, S. Bhattacharya, and A. Goswami, Nucl. Inst. Meth. **A399**, 51 (1997).
- [51] M. Saha Sarkar, P. Datta, I. Ray, C. Dey, S. Chattopadhyay, A. Goswami, P. Banerjee, R. P. Singh, P. K. Joshi, S. D. Paul, et al., Nucl. Instr. Meth. **A491**, 113 (2002).
- [52] P. Nolan, F. Beck, and D. Fossan, Ann. Rev. Nucl. Part. Sci. **45**, 561 (1994).
- [53] C. Beausang and J. Simpson, J. Phys. **G22**, 527 (1996).
- [54] S. Venkataramanan *et al.*, Proc. DAE-BRNS Symp. on Nucl. Phys. **45B**, 424 (2002).
- [55] CANDLE:, *A data acquisition and analysis software developed at inter university accelerator centre (iuac), new delhi, india*, (private communication).
- [56] Dinesh Negi, T. Trivedi, A. Babu, K. Raja, S. Kumar, A. K. Bhati, R. K. Bhowmik, J. J. Das, Abhilash, D. Kabiraj, et al., Proc. DAE-BRNS Symp. on Nucl. Phys. **53**, 307 (2008).
- [57] Veena Sharma, Sanjeev Kumar, D. Mehta, and Nirmal Singh, Phys. Rev. **A78**, 012507 (2008).
- [58] R. K. Bhowmik, *Lecture notes on Experimental Methods on Nuclear Spectroscopy* (SERC School, Kolkata, India, 2006).

- [59] R. K. Bhowmik, S. Muralithar, and R. P. Singh, Proc. DAE-BRNS Symp. on Nucl. Phys. **B44**, 422 (2001).
- [60] R. K. Bhowmik, *INGASORT Manual*, (*private communication*) (2001).
- [61] D. C. Radford *et al.*, Nucl. Instr. Meth. **A361**, 267 (1995).
- [62] DAMM:, *Milner package, the oak ridge analysis software*, (*private communication*).
- [63] R. Palit, TIFR, Mumbai, (*private communication*).
- [64] A. Z. Schwarzschild and E. K. Warburton, Annu. Rev. Nucl. Sci. **18**, 265 (1968).
- [65] R. G. Skokstad, I. A. Fraser, J. S. Greenberg, S. H. Sie, and D. A. Bromley, Nucl. Phys. **A156**, 145 (1970).
- [66] J. C. Wells, Tech. Rep., ORNL Physics Division Progress Reprt No. ORNL-6689, September **30** (1991).
- [67] N. R. Johnson, J. C. Wells, Y. Akovali, C. Baktash, R. Bengtsson, M. J. Brinkman, C. J. G. D. M. Cullen, H.-Q. Jin, I.-Y. Lee, A. O. Macchiavelli, *et al.*, Phys. Rev. **C55**, 652 (1997).
- [68] J. C. Bacelar, A. Holm, R. M. Diamond, E. M. Beck, M. A. Deleplanque, J. Draper, B. Herskind, and F. S. Stephens, Phys. Rev. Lett. **57**, 3019 (1986).
- [69] J. C. Bacelar, R. M. Diamond, E. M. Beck, M. A. Deleplanque, J. Draper, and F. S. Stephens, Phys. Rev. **C35**, 1170 (1987).
- [70] L. C. Northcliffe and R. F. Schilling, Nucl. Data, Sect **A7**, 233 (1970).
- [71] C. J. Lister, B. J. Varley, H. G. Price, and J. W. Olness, Phys. Rev. Lett. **49**, 308 (1982).
- [72] C. J. Lister, P. J. Ennis, A. A. Chishti, B. J. Varley, W. Gelletly, H. G. Price, and A. N. James, Phys. Rev. **C42**, R1191 (1990).

- [73] J. Heese, K. P. Lieb, S. Ulbig, B. Wormann, J. Billowes, A. A.Chishti, W. Gelletly, C. J. Lister, , and B. J. Varley, Phys.Rev. **41**, 603 (1990).
- [74] E. Nacher, A. Algora, B. Rubio, J. L. Tan, D. Cano-Ott, S. Courtin, P. Dessagne, F. Marchal, C. Mieh, E. Poirier, et al., Phys. Rev. Lett. **92**, 232501 (2004).
- [75] S. M. Fischer, D. P. Balamuth, P. A. Hausladen, C. J. L. M. P. Carpenter, D. Seweryniak, and J. Schwartz, Phys. Rev. Lett. **84**, 4046 ((2000).
- [76] J. Ljungvall, A. Gogen, M. Girod, J. P. Delaroche, A. Dewald, C. Dossat, E. Farnea, W. Korten, B. Melon, R. Menegazzo, et al., Phys. Rev. Lett. **100**, 102502 (2008).
- [77] A. M. Hurst *et al.*, Phys. Rev. Lett. **98**, 072501 (2007).
- [78] J. J. Valiente-Dobon *et al*, Phys. Rev. Lett. **95**, 232501 (2005).
- [79] M. Bender, P. Bonche, and P.-H. Heenen, Phys. Rev. **C74**, 024312 (2006).
- [80] Y. Sun, Eur. Phys. J. **A20**, 133 (2004).
- [81] A. Petrovici, K. W. Schmid, and A. Faessler, Nucl. Phys. **A728**, 396 (2003).
- [82] K. Kaneko, M. Hasegawa, and T. Mizusaki, Phys. Rev. **C70**, 051301(R) (2004).
- [83] A. Dhal *et al*, Eur. Phys. J. **A27**, 33 (2006).
- [84] R. A. Kaye *et al.*, Phys. Rev. **C69**, 064314 (2004).
- [85] R. A. Kaye *et al.*, Phys. Rev. **C66**, 054305 (2002).
- [86] G. Mukherjee, P. Joshi, S. N. Roy, S. Datta, R. P. Singh, S. Muralithar, and R. K. Bhowmik, Z. Phys. **A359**, 111 (1997).
- [87] C. J. Gross *et al.*, Phys. Rev. **C49**, R580 (1994).
- [88] M. A. Cardona, G. Garcia Bermudez, A. Filevich, and E. Achterberg, Phys. Rev. **C42**, 591 (1990).
- [89] Y. Sun and K. Hara, Comp.Phys. Commun. **104**, 245 (1997).

- [90] F. James and M. Roos, *Comput. Phys. Commun.* **10**, 343 (1975).
- [91] J. Dudek, W. Nazarewicz, and P. Olanders, *Nucl. Phys.* **A420**, 285 (1984).
- [92] T. Trivedi, R. Palit, D. Negi, Z. . Naik, Y.-C. Yang, Y. Sun, J. A. Sheikh, A. Dhal, M. K. Raju, S. Appannababu, et al., *Phys. Rev.* **C80**, 047302 (2009).
- [93] J. Heese, K. P. Lieb, S. Ulbig, B. Wormann, J. Billowes, A. A.Chishti, W. Gelletly, C. J. Lister, and B. J. Varley, *Phys. Rev.* **C41**, 603 (1990).
- [94] G. Z. Solomon, G. D. Johns, R. A. Kaye, and S. L. Tabor, *Phys. Rev.* **C59**, 1339 (1999).
- [95] G. N. Sylvan, J. E. Purcell, J. Doring, J. W. Holcomb, G. D.Johns, T. D.Johnson, M. A. Riley, P. C. Womble, V. A. Wood, and S.L.Tabor, *Phys. Rev.* **C48**, 2252 (1993).
- [96] L. Luhmann, M. Debray, K. P. Lieb, W. Nazarewicz, B. Wormann, J. Eberth, and T. Heck, *Phys. Rev.* **C31**, 828 (1985).
- [97] G. Mukherjee, P. Joshi, R. K. Bhowmik, S. N. R. S. Dutta, S. Muralithar, and R. P. Singh, *Nucl. Phys.* **A829**, 137 (2009).
- [98] T. Engeland, M. Hjorth-Jensen, A. Holt, and E. Osnes, *Phys. Scri.* **T56**, 58 (1995).
- [99] A. Covello, F. Andreozzi, L. Coraggio, A. Gargano, T. T. S. Kuo, and A. Porrino, *Prog. Part. Nucl. Phys.* **38**, 162 (1997).
- [100] R. Schubart, H. Grawe, J. Heese, H. Kluge, K. H. Maier, and M. Schramm, *Z. Phys.* **A352**, 373 (1995).
- [101] T. Trivedi and I. Mehrotra, *Proc. DAE-BRNS Symp. on Nucl. Phys.* **51**, 288 (2006).
- [102] K. Brueckner *et al.*, *Phys. Rev.* **97**, 1353 (1955).
- [103] B. Day *et al.*, *Rev. Mod. Phys.* **39**, 719 (1967).

- [104] H. Bethe *et al.*, Proc. Roy. Soc **A238**, 551 (1957).
- [105] M. H. Jensen *et al.*, Phys. Rep **261**, 125 (1995).
- [106] P. Brussaard, *Shell-Model Applications in Nuclear Spectroscopy* (North-Holland, Amsterdam, 1977).
- [107] B. A. Brown and W. D. M. Rae (2007), nushell@MSU, MSU-NSCL report.
- [108] B. A. Brown and K. Rykaczewski, Phys. Rev. **C71**, 044317 (2005).
- [109] A. Hosaka, K. -I. Kubo, and H. Toki, Nucl. Phys. **A444**, 76 (1985).
- [110] B. A. Brown *et al.*, Phys. Rev. **C50**, 2270(R) (1994).
- [111] M. Lipoglavsek *et al.*, Phys. Lett. **B440**, 246 (1998).
- [112] M. Gorska, H. Grawe, D. Kast, G. de Angelis, P. G. Bizzeti, B. A. Brown, A. Dewald, C. Fahlander, A. Gadea, A. Jungclauss, et al., Phys. Rev. **C58**, 108 (1998).
- [113] S. Juutinen *et al.*, Nucl. Phys. **A617**, 74 (1997).
- [114] Erdal Dikmen, Commun. theor. Phys. **51**, 899 (2009).
- [115] R. Wadsworth *et al.*, Phys. Rev. **C53**, 2763 (1996).
- [116] C. Fahlander *et al.*, Phys. Rev. **C63**, 021307(R) (1996).
- [117] A. Gadea *et al.*, Phys. Rev. **C55**, 1(R) (1997).
- [118] T. Ishii, A. Makishima, K. Koganemaru, Y. Saito, M. Ogawa, and M. Ishii, Z. Phys. **A347**, 41 (1993).